INFORMATION TO USERS

This manuscript has been reproduced from the microfilm master. UMI films the text directly from the original or copy submitted. Thus, some thesis and dissertation copies are in typewriter face, while others may be from any type of computer printer.

The quality of this reproduction is dependent upon the quality of the copy submitted. Broken or indistinct print, colored or poor quality illustrations and photographs, print bleedthrough, substandard margins, and improper alignment can adversely affect reproduction.

In the unlikely event that the author did not send UMI a complete manuscript and there are missing pages, these will be noted. Also, if unauthorized copyright material had to be removed, a note will indicate the deletion.

Oversize materials (e.g., maps, drawings, charts) are reproduced by sectioning the original, beginning at the upper left-hand corner and continuing from left to right in equal sections with small overlaps.

Photographs included in the original manuscript have been reproduced xerographically in this copy. Higher quality 6" x 9" black and white photographic prints are available for any photographs or illustrations appearing in this copy for an additional charge. Contact UMI directly to order.

Bell & Howell Information and Learning
300 North Zeeb Road, Ann Arbor, MI 48106-1346 USA

UMI®
800-521-0600

ULTRA-HIGH B DOPING DURING $Si_{1-x}Ge_x(001)$ GAS-SOURCE MOLECULAR-BEAM EPITAXY:A MECHANISTIC STUDY OF LAYER GROWTH KINETICS, DOPANT INCORPORATION, ELECTRICAL ACTIVATION, AND CARRIER TRANSPORT

BY

GLENN AARON GLASS

B.S., California Polytechnic State University at San Luis Obispo, 1994

THESIS

Submitted in partial fulfillment of the requirements
for the degree of Doctor of Philosophy in Materials Science and Engineering
in the Graduate College of the
University of Illinois at Urbana-Champaign, 1999

Urbana, Illinois

UNIVERSITY OF ILLINOIS AT URBANA-CHAMPAIGN

THE GRADUATE COLLEGE

August 1999

WE HEREBY RECOMMEND THAT THE THESIS BY

GLENN AARON GLASS

ENTITLED ULTRA-HIGH B DOPING DURING $Si_{1-x}Ge_x$ GAS-SOURCE MOLECULAR BEAM EPITAXY: A MECHANISTIC STUDY OF GROWTH KINETICS, DOPANT INCORPORATION, ELECTRICAL ACTIVATION AND CARRIER TRANSPORT

BE ACCEPTED IN PARTIAL FULFILLMENT OF THE REQUIREMENTS FOR

THE DEGREE OF DOCTOR OF PHILOSOPHY

J. Greene
Director of Thesis Research

J. E. Greene
Head of Department

Committee on Final Examination†

J. Greene
Chairperson

Ivan Petrov

J. R. Abelson

Tai C. Chiang

† Required for doctor's degree but not for master's.

O-517

ULTRA-HIGH B DOPING DURING $Si_{1-x}Ge_x(001)$ GAS-SOURCE MOLECULAR-BEAM EPITAXY:A MECHANISTIC STUDY OF LAYER GROWTH KINETICS, DOPANT INCORPORATION, ELECTRICAL ACTIVATION, AND CARRIER TRANSPORT

Glenn Aaron Glass, Ph.D.
Department of Materials Science and Engineering
University of Illinois at Urbana-Champaign, 1999
Dr. Joe Greene, Advisor

Abstract

B-doped $Si_{1-x}Ge_x(001)$ layers, with concentrations C_B up to $1.7x10^{22}$ cm^{-3}, were grown by gas-source molecular beam epitaxy (GS-MBE) from Si_2H_6, Ge_2H_6 and B_2H_6 at T_s = 500-800 °C. D_2 temperature-programmed desorption (TPD) spectra were then used to determine B coverages θ_B as a function of C_B and T_s. In these measurements, as-deposited films were immediately cooled, and hydrogen was site exchanged for deuterium to saturation coverage. Strong B surface segregation was observed with surface-to-bulk B concentration ratios ranging up to 1200.

TPD spectra of Si(001) layers exhibited β_2 and β_1 peaks associated with dideuteride and monodeuteride desorption as well as lower-temperature B-induced peaks β_2^* and β_1^*. Increasing θ_B increased the area under β_2^* and β_1^* at the expense of β_2 and β_1 and decreased the total D coverage θ_D. The TPD results were used to determine the B segregation enthalpy, -0.53 eV, and to explain the effects of high B coverages on Si(001) growth kinetics. Film deposition rates R increase by ≥ 50% with increasing $C_B \gtrsim 1x10^{19}$ cm^{-3} at $T_s \leq 550$ °C, due primarily to increased H desorption rates from B-backbonded Si adatoms, and decrease by corresponding amounts at $T_s \geq 600$ °C due to decreased adsorption site densities. The results were used to develop a robust model, with no fitting parameters, to predict the steady-state H

coverage θ_H, θ_B, and R as a function of impingement flux ratio and T_s. At $T_s \geq 700$ °C, high B coverages also induce {113} facetting.

C_B in Si(001) increases linearly with the incident precursor flux ratio and B is incorporated into substitutional electrically-active sites at concentrations up to $C_B^*(T_s)$ which, for T_s = 600 °C, is 2.5×10^{20} cm^{-3}. At higher B concentrations, C_B increases faster than $J_{B_2H_6}/J_{Si_2H_6}$ and there is a large and discontinuous decrease in the activated fraction of incorporated B. However, the total activated B concentration continues to increase and reaches a value of $N_B = 1.3 \times 10^{21}$ cm^{-3} with $C_B = 1.2 \times 10^{22}$ cm^{-3}. High-resolution x-ray diffraction (HR-XRD) and reciprocal space mapping measurements show that all films, irrespective of C_B and T_s, are fully strained. No B precipitates or misfit dislocations were detected by HR-XRD or transmission electron microscopy. The lattice constant in the film growth direction $a_\perp$ decreases linearly with increasing C_B up to the limit of full electrical activation and continues to decrease, but non-linearly, with $C_B > C_B^*$.

Room-temperature resistivity and conductivity mobility values are in good agreement with theoretical values for B concentrations up to $C_B = 2.5 \times 10^{20}$ and 2×10^{21} cm^{-3}, respectively. All results can be explained on the basis of a model which accounts for strong B surface segregation to the second-layer with a saturation coverage $\theta_{sat,B}$ of 0.5 ML (corresponding to $C_B = C_B^*$). At higher C_B (i.e., $\theta_B > \theta_{sat,B}$), B accumulates in the upper layer as shown by thermally programmed desorption measurements, and a parallel incorporation channel becomes available in which B is incorporated into substitutional sites as B-pairs which are electrically inactive but have a low charge scattering cross-section.

Isotopically-tagged temperature-programmed desorption was carried out *in-situ* on $Si_{0.82}Ge_{0.18}(001)$ layers to determine surface B and Ge coverages (θ_B and θ_{Ge}) as a function of C_B. Results show that the B segregation enthalpy decreases from -0.53 and -0.64 eV during GS-MBE Si(001) and Ge(001), respectively, to -0.42 eV during $Si_{0.82}Ge_{0.18}$ growth. C_B increases linearly with the incident precursor flux ratio $\xi = J_{B_2H_6}/(J_{Si_2H_6} + J_{Ge_2H_6})$ up to 5×10^{20} cm^{-3} corresponding to θ_B near saturation coverage (0.5 ML). The bulk Ge concentration x and θ_{Ge} are independent of ξ. Film deposition rates $R_{SiGe}(C_B)$, however, decrease by up to a factor of two with increasing $C_B \geq 5\times10^{19}$ cm^{-3} due primarily to a B-segregation-induced decrease in the adsorption site density. The above results were used to extend the capabilities of our model used above for Si(001) growth, to predict θ_H, θ_B, θ_{Ge}, and R_{SiGe} as a function of ξ and T_s.

Acknowledgments

This thesis is dedicated to my wife Cathy. Her constant support and inspiration are an integral part of the work herein.

Special thanks are extended to Dr. Greene for encouraging me to look for deeper answers to fundamental problems. Tirelessly, going through draft after draft, he never lost sight of the elusive goal. Thanks Joe, for having the patience and endurance to get us both through this!

Dr. H.-J. Kim is commended for his tireless work and cooperation. We have reaped great benefits by working on complementary projects in this area, and have significantly advanced the understanding of kinetic processes on surfaces during gas-source layer growth.

Dr. P. Desjardins was indispensable. At times when I thought that a solution was beyond reach, he was always there to supply the essential kernel of knowledge to get me back on track. His excellent editing skills advanced the state of this thesis greatly. Thanks also to Dr. M. -F. Pepin for her expert formatting assistance and advice.

Dr. M.R. Sardela Jr. provided much of the inspiration at the initial stages of the project, and taught me a great deal about x-ray diffraction.

Thanks to N. Taylor and T. Spila for keeping the lab running. Countless hours of maintenance and improvements were required, and they were always there to lend a hand. Thanks too to Y.-L. Foo and B. Cho for showing such enthusiasm, and revitalizing the lab anew. Good luck on your projects- I'm confident that you will make us all proud.

Dr. J.A.N.T. Soares assisted with electrical and optical measurements, Dr. A. Vailionis contributed with expertise on NEXAFS measurements, and J. Baker provided me with the knowledge to interpret, and access to perform, SIMS measurements critical to this work.

Drs. I. Robinson and D. Walko lent their time and resources for the *in-situ* annealing study. Thanks for the assistance and advice.

Thanks to B. Thrasher for all your help. You regularly performed miracles to keep the GS-MBE system operational. I honor you with the burn-box salute of gratitude!

Thanks again to everyone I've had the pleasure to interact with during my time here.

Glenn Glass, Urbana IL August 2 1999

Table of Contents

List of tables

List of figures

CHAPTER 1. Introduction

Ultra-high B doping (concentrations $C_B > 5\times10^{19}$ cm^{-3}) is currently of interest for use in Si and $Si_{1-x}Ge_x$ applications including emitter layers in Si bipolar junction transistors (BJT),[1] source and drain regions in metal-oxide-semiconductor transistors, electromigration-resistant selectively-grown epitaxial zero-level metallization layers,[2,3] and etch stop layers.[4] Device designs employing $Si_{1-x}Ge_x$/Si heterostructures provide additional degrees of freedom over traditional Si devices, and permit both bandgap engineering and higher hole mobilities,[5] associated with $Si_{1-x}Ge_x$ layers strained in compression. Due to its bandgap discontinuity with Si, a $Si_{1-x}Ge_x$-base heterojunction bipolar transistor (HBT) can have higher emitter injection efficiency than an equivalent Si BJT while maintaining a high base dopant concentration. Thus, higher current gains are possible without increasing the base resistance. In addition, a graded Ge concentration provides a built-in electric field which reduces the transit time of minority carriers across the base. HBTs utilizing p-type $Si_{1-x}Ge_x$ base layers have been shown to have higher current gains and faster switching speeds, up to 160 GHz,[6] than those obtained with Si homojunction devices. Accurate measurements of electrical properties as a function of alloy composition x and hole concentration p in the ultra-high doping regime (> 10^{19} cm^{-3}) for strained p-type $Si_{1-x}Ge_x(001)$ layers are necessary for the design of future high-performance devices.

Reported B equilibrium solid solubilities in Si range from 8×10^{20} cm^{-3} at 1400 °C[7] to ≈ 1-1.5$\times10^{20}$ cm^{-3} at 1000 °C[8,9] and 2×10^{19} cm^{-3} at 700 °C.[8] Electrically-active B concentrations of 1-3$\times10^{20}$ cm^{-3} have been reported for Si(001):B layers grown by ultra-high

vacuum chemical-vapor deposition[10] and solid-source molecular-beam epitaxy.[11] However, the reaction paths leading to the incorporation of both electrically-active as well as inactive B are not well understood.

Many of the problems associated with B-doped $Si_{1-x}Ge_x$ are related to the manufacturability of electronic-quality epitaxial thin films at a reasonable cost. Gas-source molecular-beam epitaxy (GS-MBE) and ultra-high-vacuum chemical vapor deposition (UHV-CVD) offer advantages over solid-source MBE for the growth of Si, Ge, and $Si_{1-x}Ge_x$ layers. These include the elimination of high-temperature evaporation sources, reduced particulate contamination, higher sample throughput, better conformal coverage and the capability for selective epitaxy on patterned substrates.[12]

While initial research on GS-MBE was carried out using silane (SiH_4) as the source gas,[13] disilane (Si_2H_6) was found to yield considerably higher deposition rates.[14] The T_s dependence of the growth rate curve follows the general form expected for chemical-vapor deposition (CVD) in which R saturates at high temperatures in an impingement-flux limited growth regime, while at low temperatures, R decreases exponentially with $1/T_s$ indicative of surface reaction limited growth. In investigations of the mechanisms and kinetics controlling Si atomic-layer epitaxy, Lubben et al.[15] of our group showed that the higher reactivity of Si_2H_6 is primarily due to the fact that the Si-Si bond is weaker than the Si-H bond.[16] Si GS-MBE deposition rates R from Si_2H_6 are well described over a wide range in incident fluxes $J_{Si_2H_6}$ ($0.3\text{-}7.7\times10^{16}$ $cm^{-2}s^{-1}$) and growth temperatures T_s (500-950 °C) using a model, with no fitting parameters, based upon dissociative Si_2H_6 chemisorption followed by a series of surface decomposition reactions with the rate-limiting step being first-order hydrogen

desorption from Si monohydride[17] for which the activation energy is 2.04 eV.[18] The zero-coverage Si_2H_6 reactive sticking probability in the impingement-flux-limited growth regime, $T_s \gtrsim 700$ °C, was found by Bramblett et al.[17] of our group to be 0.036, more than two orders of magnitude higher than that for SiH_4.[19]

1.1. Effects of Ge concentration on H_2 desorption and $Si_{1-x}Ge_x(001)$ layer growth kinetics

One potential disadvantage of GS-MBE and UHV-CVD is that the kinetics of gas-source $Si_{1-x}Ge_x$ layer growth are complex.[20] In general, layer growth rates R from hydride precursors depend upon precursor adsorption kinetics which, in turn, are a sensitive function of H_2 desorption kinetics. The key factors in predicting R_{SiGe} are the Ge surface segregation rate, resultant steady-state elemental surface coverages, and hydrogen binding energies from these species.[20-26]

Our group has recently used isotopically-tagged *in-situ* D_2 TPD to probe Ge segregation and H desorption pathways from GS-MBE $Si_{1-x}Ge_x$ layers.[20-22] TPD spectra from $Si_{1-x}Ge_x(001)$ surfaces contain β_1, β_1', β_2, α_1 and α_2 peaks due to Si 2×1 monodeuteride $^{D}\backslash Si-Si/^{D}$, mixed Si-Ge dimer 2×1 monodeuteride $^{D}\backslash Si-Ge/^{D}$, Si 1×1 dideuteride $^{D}\backslash Si/^{D}$, Ge 2×1 monodeuteride $^{D}\backslash Ge-Ge/^{D}$, and Ge 1×1 dideuteride $^{D}\backslash Ge/^{D}$ surface species. Kim et al.[20-22] of our group observed that the monodeuteride binding energies E_{Si} at Si sites and E_{Ge} at Ge sites both decrease linearly with increasing Ge surface coverage θ_{Ge}. At all Ge coverages, however, E_{Si} is much larger than E_{Ge} and the steady-state H coverage θ_H on Si sites is much larger than on Ge. It was shown that D atoms diffuse preferentially to Si sites,

at which their binding energy is higher than on Ge, and desorb from there. Thus, $Si_{1-x}Ge_x$ growth kinetics are dominated by H desorption from Si sites.[22] The overall dangling-bond density, as measured by the saturation deuterium coverage θ_D is independent of x.[22] These results were incorporated into a predictive model, with no fitting parameters, for the growth rate R_{SiGe} and composition x of GS-MBE $Si_{1-x}Ge_x$ as a function of the precursor fluxes $J_{Si_2H_6}$ and $J_{Ge_2H_6}$ and the growth temperature T_s.[20] Calculated results show very good agreement with experiment.

1.2. B incorporation

Our group has previously demonstrated[27] that for Si(001) and Ge(001) layers grown by gas-source molecular-beam epitaxy (GS-MBE) from $B_2H_6/Si_2H_6/Ge_2H_6$ mixtures, C_B decreases exponentially with $1/T_s$ at constant flux ratio, and increases linearly with increasing flux ratio $J_{B_2H_6}/J_{Si_2H_6}$, or $J_{B_2H_6}/J_{Ge_2H_6}$, at constant film growth temperature T_s for B concentrations below 2×10^{19} cm^{-3}. B incorporation is thermally-activated and B_2H_6 reactive sticking probabilities on Si(001) surfaces range from $\approx 6.4\times10^{-4}$ at $T_s = 600$ °C to 1.4×10^{-3} at 950 °C[27] while Si deposition from Si_2H_6 is precursor-mediated.[28] B_2H_6 reactive sticking probabilities on Ge(001) surfaces range from $\approx 8\times10^{-4}$ at $T_s = 300$ °C to 1.2×10^{-5} at 600 °C.[16,29]

1.3. B clustering

Si films with B concentrations far exceeding bulk solubility limits are of particular interest for nanoscale electronic device fabrication such as base layers in high frequency Si and $Si/Si_{1-x}Ge_x$ heterostructure bipolar transistors.[6] Although high dopant concentrations can

be achieved by ion implantation, spreading of B profiles due to transient-enhanced diffusion during post-annealing limits the formation of shallow abrupt junctions at submicron scales.[30] GS-MBE offers the possibility of achieving ultra-high doping concentrations, transport properties equivalent to bulk Si, and the formation of abrupt doping profiles *in-situ* without subsequent annealing.[31,32]

While the ability to prepare kinetically-controlled ultra-high B-doped Si film structures represents an important advance, there is still little understanding of the reaction path leading to the incorporation of B in non-electrically-active sites during GS-MBE growth of Si(001):B at ultra-high B concentrations. For other common p- and n-type dopants such as Al, Ga, P, and Sb, the electrically-active fraction progressively decreases as the dopant concentration is increased above the kinetic solubility limit.[33] This is due to the formation of precipitates which, once nucleated, act as sinks for dopant atoms and thus decrease the doping concentration in substitutional Si sites.[34] The second-phase precipitates typically exceed 10 nm in size and can therefore be detected by transmission electron microscopy (TEM). In the case of ultra-high B doping, however, there are no credible reports of observed precipitates in as-grown layers suggesting that, if they are present, they must be in the form of small ($\lesssim$ 50 atoms) dispersed clusters. Moreover, unlike other dopants, the concentration N_B of electrically-active B in GS-MBE Si(001) continues to increase with increasing C_B even as the electrically active fraction of B atoms decreases.[31]

It has been suggested that B clustering is the cause of incomplete B activation in ion-implanted Si.[35] However, there has been no clear explanation of either the reaction path leading to inactive B incorporation or the site and local bonding configuration into which the

inactive B is incorporated during film growth. A study of B ion-implanted depth distributions measured by secondary ion mass spectrometry (SIMS) predicts that B clusters larger than five atoms are unstable.[30] B-Si interactions in small clusters have been modeled using *ab initio* methods based on density functional theory and the local density aproximation.[36,37] The lowest-energy configuration for B clusters was proposed to be B pairs aligned along ⟨001⟩ directions and occupying single Si lattice sites.

1.4. Statement of objectives

The ultimate goal of this research program is to understand, model, and control GS-MBE growth kinetics, B incorporation kinetics, and the B bonding environment for B-doped GS-MBE $Si_{1-x}Ge_x$ layers grown on Si(001) from $Si_2H_6/Ge_2H_6/B_2H_6$ mixtures as a function of T_s and incident precursor flux ratios. Investigations are focused on three major kinetic processes: (1) the effects of Ge and B on hydrogen desorption kinetics (2) Ge and B surface segregation during GS-MBE growth, and (3) the incorporation pathway and local bonding configuration of B in electrically-inactive lattice sites. From these experimental results, a detailed understanding of the complex effects of B doping on H desorption kinetics from $Si_{1-x}Ge_x$ layers was developed.

Segregation enthalpies were determined for B in $Si_{1-x}Ge_x$ layers with $x = 0$ and 0.18. Growth kinetics have been modeled for B-doped Si, and B-doped $Si_{1-x}Ge_x$. The maximum electrically-active B incorporation limit was determined, and the B incorporation mechanism giving rise to electrically-inactive B was discovered. A detailed study of B incorporation revealed that under conditions where the steady-state segregated B coverage exceeds the

second-layer saturation coverage of 0.5 ML, a parallel B incorporation mechanism becomes active. In this regime, B concentrations as a function of B_2H_6 impingement flux increase at a greater than linear rate, and the increase corresponds to incorporation in the form of B pairs on single lattice sites. All B pair bonds, as well as those of the surrounding matrix, are fully saturated leading to electrical deactivation of B dopant atoms.

1.5. Publications

The results of my research are summarized in the following publications presented as chapters 4 through 7.

Chapter 4:

Effects of high B doping on Si(001) dangling bond densities, H desorption, and film growth kinetics during gas-source molecular-beam epitaxy. G. Glass, H. Kim, M.R. Sardela, Q. Lu, J.R.A. Carlsson, J.R. Abelson, and J.E. Greene, Surface Science, **392**, 63 (1997),

Si(001):B gas-source molecular-beam epitaxy: Boron surface segregation and its effect on film growth kinetics. H. Kim, G. Glass, T. Spila, N. Taylor, S.Y. Park, J.R. Abelson, and J.E. Greene, Journal of Applied Physics, **82**, 2288 (1997),

Effects of B doping on hydrogen desorption from Si(001) during gas-source molecular-beam epitaxy from Si_2H_6 and B_2H_6. H. Kim, G. Glass, S.Y. Park, T. Spila, N. Taylor, J.R. Abelson, and J.E. Greene. Applied Physics Letters, **69**, 3869 (1996).

Chapter 5:

Ultra-high B doping during Si(001) gas-source molecular-beam epitaxy: B incorporation, electrical activation, and hole transport. G. Glass, H. Kim, P. Desjardins, N. Taylor, T. Spila, Q. Lu, and J.E. Greene, submitted Physical Review B 6/99.

Chapter 6:

Electrically active and inactive B lattice sites in ultra-highly B doped Si(001): An x-ray near-edge absorption fine-structure and high-resolution diffraction study. A. Vailionis, G. Glass, P. Desjardins, David G. Cahill, and J.E. Greene, Physical Review Letters **82**, 4464 (1999).

Chapter 7:

$Si_{1-x}Ge_x(001)$:B gas-source molecular-beam epitaxy: Boron surface segregation and its effect on layer growth kinetics. H. Kim, G. Glass, and J.E. Greene, submitted, Journal of Applied Physics 7/99.

In addition, the following papers, not contained in the thesis, discuss further results which were obtained during the course of my research.

1. B incorporation and hole transport in fully strained heteroepitaxial $Si_{1-x}Ge_x$ grown on Si(001) by gas-source molecular-beam epitaxy from Si_2H_6, Ge_2H_6 and B_2H_6. Q. Lu, M.R. Sardela, N. Taylor, G. Glass, T.R. Bramblett, T. Spila, J.R. Abelson, and J.E. Greene, Journal of Crystal Growth, **179**, 97 (1997).
2. Arsenic-doped Si(001) gas-source molecular-beam epitaxy: Growth kinetics and transport properties. J.A.N.T. Soares, H. Kim, G. Glass, P. Desjardins and J.E. Greene, Applied Physics Letters, **74**, 1290 (1999).
3. Structure of the Si(011)16×2 surface and hydrogen desorption kinetics investigated using temperature programmed desorption. H. Kim, N. Taylor, T. Spila, G. Glass, S.Y. Park, J.E. Greene, and J.R. Abelson, Surface Science **380**, L496 (1997).
4. Growth of $Si_{1-x}Ge_x(011)$ on Si(011)16×2 by gas-source molecular-beam epitaxy: Growth kinetics, Ge incorporation, and surface phase transitions. N. Taylor, H. Kim, T. Spila, J.A. Eades, G. Glass, P. Desjardins, and J.E. Greene, Journal of Applied Physics **85**, 501 (1999).
5. Ultra-high B doping during $Si_{0.82}Ge_{0.18}(001)$ gas-source molecular-beam epitaxy: B incorporation, electrical activation, and hole transport. G. Glass, H. Kim, J.A.N.T. Soares and J.E. Greene, in preparation.

6. Growth kinetics of CVD Si(001):B growth from $SiH_4/B_2H_6/H_2$: A robust physical model. G. Glass, H. Kim, K. Violette and J.E. Greene, in preparation.
7. Raman spectroscopy of ultra-highly B doped Si(001) layers grown by gas-source molecular-beam epitaxy: Effects of the interaction of substitutional and paired B atoms on the Si-Si line position and width. G. Glass, J.A.N.T. Soares, M. Stohr and J.E. Greene, in preparation.

1.6. References

1. T. Uchino, T. Shiba, T. Kikuchi, Y. Tamaki, A. Watanabe, and Y. Kiyota, IEEE Trans. Elec. Dev. **42**, 406 (1995).
2. Y. Kinoshita, K. Imai, H. Yoshida, H. Suzuki, T. Tatsumi, and T. Yamazaki, Proc. Internat. Electr. Dev. Meeting, San Francisco, December, 1994, p. 441.
3. Y. Kiyota, T. Nakamura, S. Suzuki, and T. Inada, IEEE Trans. Elec. **E79C**, 554 (1996).
4. R.R.A. Syms, B.M. Hardcastle, and R.A. Lawes, Sensors & Actuators **A63**, 61 (1997).
5. Q. Lu, M.R. Sardela, Jr., T.R. Bramblett, and J.E. Greene, J. Appl. Phys. **80**, 4458 (1996).
6. U. Konig, IEE Colloquium Advances in Semiconductor Dev. **25**, 6 (1999); T. Uchino, T. Shiba, T. Kikuchi, Y. Tamaki, A. Watanabe, and Y. Kiyota, IEEE Trans. Elec. Dev. **42**, 406 (1995).
7. S.M. Sze, *Physics of Semiconductor Devices* (John Wiley and Sons, New York, 1981, 2nd Edition).
8. F.N. Schwettman, J. Appl. Phys. **45**, 1918 (1974).
9. G.L. Vick and K.M. Whittle, J. Electrochem. Soc. **119**, 1142 (1969).
10. B.S. Meyerson, in *Springer Series in Materials Science: Semiconductor Silicon*, edited by G. Harbeke and M.J. Schulz (Springer-Verlag, New York 1988) vol. 13, p. 24.
11. C.P. Parry, R.A. Kubiak, S.M. Newstead, T.E. Whall, and E.H.C. Parker, J. Appl. Phys. **71**, 118 (1992).
12. H. Hirayama, T. Tatsumi, and N. Aizaki, Appl. Phys. Lett. **52**, 2242 (1988)., and K. Aketagawa, T. Tatsumi, and J. Sakai, Appl. Phys. Lett. **59**, 1735 (1991).
13. H. Hiroyuki, T. Tatsumi, A. Ogura, and N. Aizaki, Appl. Phys. Lett. **51**, 2213 (1987).
14. T.R. Bramblett, Q. Lu, T. Karasawa, M.-A. Hasan, S.K. Jo, and J.E. Greene, J. Appl. Phys. **76**, 1884 (1994).
15. D. Lubben, R. Tsu, T.R. Bramblett, and J.E. Greene, J. Vac. Sci. Technol. A **9**, 3003 (1991).
16. Q. Lu, T.R. Bramblett, M.-A. Hasan, and J.E. Greene, J. Appl. Phys. **78**, 6027 (1995).

17. T.R. Bramblett, Q. Lu, T. Karasawa, M.-A. Hasan, S.K. Jo, and J.E. Greene, J. Appl. Phys. **76**, 1884 (1994).

18. K. Sinniah, M.G. Sherman, L.B. Lewis, W.H. Weinberg, J.T. Yates, and K.C. Jandas, J. Chem. Phys. **92**, 5700 (1990).

19. H. Hiroyuki, T. Tatsumi, A. Ogura, and N. Aizaki, Appl. Phys. Lett. **51**, 2213(1987); F. Hirose, M. Suemitsu, N. Miyamoto, Japan. J. Appl. Phys. **28**, L2003 (1989); M. Suemitsu, F. Hirose, Y. Takagywa, and N. Miyamoto, J. Crystal Growth **105**, 203(1990); H. Hirayama, T. Tatsumi, and N. Aizaki, J. Cryst. Growth **95**, 476 (1989).

20. H. Kim, N. Taylor, T. R. Bramblett, and J. E. Greene, J. Appl. Phys. **84**, 6372 (1998).

21. H. Kim, N. Taylor, J.R. Abelson, and J.E. Greene, J. Appl. Phys. **82**, 6062 (1997).

22. H. Kim, P. Desjardins, J. R. Abelson, and J. E. Greene, Phys. Rev. **B58**, 4803 (1998).

23. G. Glass, H. Kim, M.R. Sardela, Q. Lu, J.A. Abelson, and J.E. Greene, Surface Science, **392**, L63 (1997).

24. H. Kim, G. Glass, T. Spila, N. Taylor, J. R. Abelson, and J. E. Greene, J. Appl. Phys. **82**, 2288 (1997).

25. H. Kim, G. Glass, S.Y. Park, T. Spila, N. Taylor, J.R. Abelson, and J.E. Greene, Appl. Phys. Lett. **69**, 3869 (1996).

26. H. Kim and J. E. Greene, J. Vac. Sci. Technol. **A17**, 354 (1999).

27. Q. Lu, T.R. Bramblett, N.-E. Lee, M.-A. Hasan, T. Karasawa, and J.E. Greene, J. Appl. Phys. **77**, 3067 (1995).

28. J.R. Engstrom, L.Q. Xia. M.J. Furjanic, and D.A. Hansen, Appl. Phys. Lett. **63**, 1821 (1993).

29. H. Kim and J.E. Greene, J. Vac. Sci. Technol. **A17**, 354 (1999).

30. P.A. Stolk, H.-J. Gossmann, D.J. Eaglesham, J. M. Poate, Nucl. Inst. and Meth. B **96**, 187 (1995).

31. G. Glass, H. Kim, P. Desjardins, N. Taylor, T. Spila, Q. Lu and J.E. Greene, Submitted, Phys. Rev. B.

32. H. Kim, G. Glass, T. Spila, N. Taylor, S.Y. Park, J.R. Abelson, and J.E. Greene, J. Appl. Phys. **82**, 2288 (1997); G. Glass, H. Kim, M.R. Sardela, Q. Lu, J.R.A. Carlsson, J.R. Abelson, and J.E. Greene, Surf. Sci. **392**, L63 (1997).

33. Reported equilibrium solid solubilities at 900 °C are: 6×10^{20} cm^{-3} for P, 3×10^{19} cm^{-3} for Sb, 2×10^{19} cm^{-3} for Ga, and 1.5×10^{19} cm^{-3} for Al. For B in Si, reported solid solubilities range from 2×10^{19} cm^{-3} at 700 °C to 8×10^{20} cm^{-3} at 1400 °C. See *Impurities and Defects in Group IV Elements and III-V Compounds*, eds.: O. Madelung and M. Schulz, Landolt-Börnstein, New Series, Group III, Vol. 22, Pt. a (Springer, Berlin, 1989).

34. P. Ostoja, D. Nobili, A. Armigliato, and R. Angelucci, J. Electrochem. Soc. **123**, 124 (1976).

35. F.N. Schwettmann, J. Appl. Phys. **45**, 1918 (1974).

36. E. Tarnow, J. Phys. Condens. Matter **4**, 5405 (1992).

37. J. Zhu, T. Diaz dela Rubia, L. H. Yang, C. Mailhiot, and G.H. Gilmer, Phys. Rev. B **54**, 4741 (1996

CHAPTER 2. Background

B has been the primary p-type dopant in Si device fabrication for more than 30 years, yet there is still no consensus on the mechanism leading to B deactivation at high concentrations. Reports of B precipitates observed in transmission electron microscopy (TEM) images from ion-implanted Si[1] with $C_B > 1\times10^{17}$ cm^{-3} were later shown to be incorrect. The features were actually dislocation loops, as determined by $\bar{g}\cdot\bar{b}$ analyses of TEM images ($\bar{g}$ is the diffraction vector and $\bar{b}$ is the dislocation Burgers' vector).[2] The loops form as Si self-interstitials, created during implantation, condense during post-implant annealing to yield regions with inserted {113} planes.[3] Similar structures have been observed, following annealing at 900 °C for 100 hours, in B-doped Czochralski-grown Si with $C_B = 1\times10^{19}$ cm^{-3}.[4] In this case, the thermally-generated Si self-interstitials condense on {112} planes. Electrical deactivation of B acceptors has been reported to be linked to the presence of the above dislocation structures.[3]

2.1. B "precipitation"

Armigliato et al.[5] were among the first groups to publish data regarding B precipitation in bulk Si. This study consisted of annealing highly doped bulk wafers, and performing electrical measurements and TEM analyses before and after annealing. The study claims observations of B precipitates in the concentration range C_B $2\text{-}5\times10^{20}$ cm^{-3} after 240 hours at 1100 °C. The oxygen content in the wafers was not quantified, and the possibility of the precipitate being an oxide, or even heterogenous nucleation of a silicon boride on an oxide precipitate was a possibility. This group noted in the same publication, in agreement with

others,[6] that drive-in diffusion from a borosilicate glass layer resulted in a surface B concentration in Si which was much greater (up to a factor of three) than the "equilibrium" solid solubility value. The literature is also congested with reports of B ion implantation studies claiming to determine equilibrium solid-solubility values.[7] Ion implantation studies claiming to report TEM evidence for precipites, in fact demonstrate ion damage-induced dislocation loop growth.[8]

A report by Wijarankula[9] demonstrates that wafers grown by the Czochralski method, doped to concentrations near the reported solubility limit, 1.7×10^{19} cm^{-3}, fail to exhibit precipitates even after 100 hours of annealing at 900 °C, nor when annealed for 50 additional hours at 1050 °C. These samples were reported to contain dislocation loops which lie in {110} planes with Burgers vectors of the type a/2<110>, and sides parallel to either <110> or <112> directions. Within these large (~1 μm) loops, much smaller (15 nm) rhombus-shaped dislocation loops were found which lie in {211} planes with Burgers vectors of the type a/6<211> bound by <211> line segments. The unique feature of {11X} (x=2,3) planes is that they can incorporate interstitial atoms in a manner which is energetically favorable.[10] It was observed that the density of these dislocation loops is dependent upon C_B suggesting that B increases the concentration of interstitial Si atoms present after thermal processing. Furthermore, since the a/3<111>-type stacking faults in Si are known to be produced via a condensation of Si interstitials, the presence of the faults, and their subsequent growth during annealing further supports the assertion that interstitial species were present in abundance. This indicated that B acts as a trap for Si-self interstitials, and spurred the following investigations into the link between B-related defects and Si-self interstitials.

2.2. Interstitial-enhanced B diffusion and B clustering

The relationship between Si-self interstitial formation and B diffusion was explained by Fahey[11] et al. in their report on the phenomenon of oxidation enhanced diffusion (OED) of B in Si. OED is caused by injection of Si-self interstitials from the surface during oxidation. The presence of Si-self interstitials was shown to enhance the diffusion rate of B in Si, and B diffusion was found to proceed via a kick-out mechanism.

Ion implantation of B has been shown to result in incomplete electrical activation for implanted doses above 2×10^{15} cm^{-2} resulting in peak carrier concentrations ~ 5×10^{19} cm^{-3}. However Si-coimplantations, leading to amorphization, increased peak carrier concentrations to ~ 10^{20} cm^{-3}.[7,12] Ion-induced damage is reduced in a subsequent annealing step following implantation. During the anneals, dislocation loops form and grow. Diffusion models which incorporate Si self interstitial diffusion as the limiting step for dislocation loop growth have been successful in predicting B diffusional behavior.[13] Stolk et al.[14] noted that B diffusion rates were enhanced by over an order of magnitude during the initial stages of annealing and applied the name transient enhanced diffusion (TED) to the phenomenon. TED has been shown to occur when Si is damaged by ion implantation, and B is present at peak concentrations as low as 5×10^{17} cm^{-3}. Fast and slow diffusing B species are present simultaneously.

TED during activation anneals of shallow B implants causes significant uncontrolled peak broadening. At high B concentrations ($C_B > 5\times10^{19}$ cm^{-3}), only a portion of the B dose becomes electrically-activated and a correlation was found between the slow diffusing species and inactive B concentrations. The above observations and the considerable economic

consequences of TED spurred Zhu et al.[15] to perform *ab-initio* pseudopotential calculations on a larger scale than previously attempted. The lowest energy B cluster configuration was found to be a split-substitutional (dumb-bell) interstitialcy. A reaction path is predicted as follows:

$B_s + Si_i \rightarrow B_s\text{-}Si_i$ substitutional B/ interstitial Si complex. $\Delta E = -1.1$ eV (2.1)

$B_s\text{-}Si_i \leftrightarrow B_i + Si$ kick-out of substitutional B (2.2)

$B_s\text{-}Si_i + B_s \rightarrow B\text{-}B$ dumb-bell interstitialcy $\Delta E = -1.8$ eV (2.3)

In the above reaction steps, Si_i represents a Si atom on an interstitial site, B_i is a B atom on an interstitial site, and Si and B_s are Si an B atoms on substitutional lattice sites. The reversible reaction in equation 2.2 is the dominant B diffusion mechanism in Si, and occurs more rapidly in the presence of high Si-self interstitial concentrations. The dumb-bell species created in equation 2.3 has a diffusion rate at least two orders of magnitude lower than the reported value for B diffusion at low concentrations. B atoms composing the B interstitialcy are trigonally, rather than tetrahedrally, bonded. Therefore, the pair is electrically-inactive, since all B bonds as well as those of their Si neighbors are saturated. The B pairs are aligned along <100> axes on a single substitutional lattice site. Larger clusters, such as B_6, and B_{12} are also predicted. However, large kinetic barriers reduce their likelihood of formation.[16]

2.3. Near edge x-ray absorption fine-structure spectroscopy and B bonding

The possible existence of small B clusters is difficult to test experimentally due to their weak scattering power. However, near-edge x-ray absorption fine structure spectroscopy

(NEXAFS) has been shown to be capable of distinguishing sp^2 from sp^3 bonding in inorganic B-containing compounds.[17,18] In BF_3, hexagonal BN, and B_2O_3, where B is bonded to three atoms in a planar trigonal configuration, the 2p orbitals are split resulting in π (originating from $2p_z$ atomic orbitals) and σ (arising from hybridized 2s, $2p_x$, and $2p_y$ atomic orbitals) molecular orbitals.[19] As a consequence, B in sp^2 coordination yields a sharp intense low-energy NEXAFS peak corresponding to a $1s \rightarrow 2p_z$ (π^*) excitation and a broad high-energy feature corresponding to the $1s \rightarrow \sigma^*$ transition. In contrast, for tetrahedrally sp^3 bonded B (e.g., in KBF_4 and cubic BN), all three hybridized p-states are degenerate giving rise to only σ bonds. Therefore, NEXAFS spectra from sp^3-coordinated B compounds exhibit a single broad feature originating from overlapping $1s \rightarrow \sigma^*$ transitions.[17,18] Chapter 6 describes the use of this technique in the determination of the bonding environment surrounding electrically active and inactive B atoms in ultra-highly doped GS-MBE Si(001):B.

2.4. Temperature programmed desorption (TPD)

TPD is a widely used surface science probe for investigating gas/solid adsorption and desorption kinetics. Under the proper experimental conditions, it allows the determination of desorption activation energies, pre-exponential factors, number density of desorbing species, and the kinetic order of the desorption reaction. A programmed temperature rise, typically linear ramping, is applied to the substrate and the local partial pressure in a continuously pumped system is recorded by a mass spectrometer to produce the desorption spectra. The apparatus is composed of two independently pumped chambers, connected by an orifice. The sample is in the first chamber and can be rotated to a direct line-of-site position to front of the

mass spectrometer in the second chamber. Desorption spectra are recorded from the front face of the sample with negligible contribution from sample holder, chamber walls, etc.

According to Redhead,[20] the pressure p* of the desorbing speciescan be expressed as a function of the desorption rate N(t),

$$\frac{dp^*}{dt} + \frac{p^*}{\tau} = aN(t) \tag{2.4}$$

where τ is the residence time and a is a constant related to system geometry including chamber volume, sample size, etc. For very high pumping speeds or at sufficiently low heating rate ($\zeta = dT/dt$), $\tau \rightarrow 0$ and the desorption rate N(t) becomes proportional to the rate of pressure increase. General equations describing desorption kinetics have been derived by Polanyi and Wigner.[21] The rate change in coverage θ of an adsorbed species is given by,

$$\frac{d\theta}{dt} = -\nu\theta^n \exp\left(-\frac{E_d}{kT_s}\right) \tag{2.5}$$

where n is the reaction order, ν is a pre-exponential factor, k is Boltzman's constant, T_s is the sample temperature, and E_d is the desorption activation energy. For high pumping speeds, where $P \propto -d\theta/dT$, the maximum occurs in the P versus T curve when[22]

$$\frac{dP}{dT} = 0 = \frac{d}{dT}\left(-\frac{d\theta}{dT}\right) = -\nu\exp\left(-\frac{E_d}{kT_p}\right)\left[n\theta_p^{n-1}\left(\frac{d\theta}{dT}\right)_{T_p} - \theta_p^n\left(\frac{E_d}{kT_p}\right)\right]. \tag{2.6}$$

The solution to the above equation, with the relationship $dT = \zeta dt$, yields,

$$\ln\left(\frac{T_p\theta_p^{n-1}}{\zeta}\right) = \frac{E_d}{kT_p} + \ln\left(\frac{E_d}{n\nu k}\right) \tag{2.7}$$

where T_p is the temperature at which the desorption signal intensity is at a maximum and θ_p is the coverage at T_p. From equation 2.7, we see that if the kinetic order is 1, T_p and the peak

half-width are independent of initial coverage and the shape of the spectrum is non-symmetric. For second-order desorption, T_p decreases, the half-width increases with increasing initial coverage, and spectral shapes are symmetric.

TPD spectra can be simulated by expressing coverage θ as a function of T_s. From equation 2.5 with the relationship $dT = \zeta dt$, [22]

$$\ln\left(\frac{\theta(T)}{\theta_o}\right) = -\frac{\nu}{\zeta} I(T) \tag{2.8}$$

for first-order desorption and

$$\theta(T) = \frac{\theta_o}{1 + (\frac{\nu}{\zeta})\theta_o I(T)} \tag{2.9}$$

for second-order desorption. θ_o in equations 2.8 and 2.9 is the initial coverage and I(T) is given by

$$I(T) = \frac{E_d}{k}\left[\frac{e^{-\varepsilon}}{\varepsilon^2}\sum_{n=1}^{\infty}\frac{(-1)^{n+1}n!}{\varepsilon^{n-1}}\right]_{To}^{T} \tag{2.10}$$

in which $\varepsilon = E_a/kT$. Example TPD spectra, calculated using $E_d = 2.60$ eV, $\nu = 1\times10^{13}$ s^{-1}, and $\zeta = 2$ °C s^{-1}, are shown in Fig. 2.1 for first-order and second-order desorption. Fig. 2.2 shows the effects of desorption activation energy and pre-exponential factor on TPD peak position and shape for first-order desorption kinetics. The peak temperature increases with increasing activation energy and/or decreasing pre-exponential factor.

2.5. Hydrogen adsorption and desorption on Si(001) and Ge(001)

The clean Si(001) surface exhibits a 2×1 reconstruction consisting of σ-bonded Si-Si dimers in 90°-rotated domains. The dangling bonds on each dimer form relatively weak π bonds.[23-25] Research on the surface structure of hydrogenated Si (001) using LEED, EELS, and photoemission spectroscopy have shown that there are three types of surface reconstructions: 1×1, 2×1, and 3×1.[26-29] The 2×1 reconstruction, in which the surface consists of monohydride phase, is produced by H adsorption of up to 1 ML at low temperature (T_s< 400 °C) or by saturated adsorption of H at elevated substrate temperature (T_s > 400 °C). Additional H exposure at lower temperature, for example at room temperature, yields a 1×1 surface structure which has an ideal H coverage of 2 ML.[26-28] In 1985 Chabal et al[29] reported, following saturation exposure at 100 °C, a 3×1 phase composed of alternating monohydride and dihydride units.

H_2 desorption kinetics from Si(001) have been studied using various surface analysis techniques including TPD, laser-induced thermal-desorption (LITD), and isothermal desorption.[30-34] TPD studies have shown that there are two desorption peaks, labeled β_1 and β_2, arising from 2×1 monohydride and 1×1 dihydride phases, respectively. A typical D_2 TPD spectrum from a clean Si(001) surface is shown in Fig. 2.3 fitted using desorption equations described in section 2.4. The fitted results were obtained with E_d and ν equal to 1.88 eV and 1×10^{13} s^{-1} for β_2 and 2.52 eV and 1×10^{15} s^{-1} for β_1, in reasonable agreement with refs. 30-34.

The desorption of hydrogen from the monohydride phase on Si (001) follows first order kinetics over a broad range of coverage as first observed by Sinniah et al.[30] This is due to concerted desorption of H_2 from "paired" hydrogen atoms on a single Si dimer. The pairing

of hydrogen atoms is caused by an attractive interaction between unpaired dangling bonds. Pairing of isolated dangling bonds results in π bond formation and hence lowers the surface free energy by $\approx$ 0.8 eV/bond as determined by Boland using scanning tunneling spectroscopy.[35] Later, Höfer et al. showed, using optical second-harmonic generation, that hydrogen desorption kinetics depart from first order when $\theta_H < 0.1$ ML.[36] This is because desorption at such low coverages becomes limited by bimolecular recombination and is thus second order.

Desorption of hydrogen from the dihydride phase on Si (001) follows second-order kinetics,[34] indicating that it is limited by recombination. However, the detailed desorption mechanism is still not understood. The presently accepted mechanism is recombination from adjacent dihydride units leaving each dimer with one H.

The Ge(001) 2×1 surface has a structure similar to that of the Si(001) and consists of buckled dimer rows along <110> directions. However, there is disagreement regarding the existence of the Ge dihydride phase. The first TPD study of Ge(001):H reported only one desorption peak which was attributed to desorption from the monohydride phase.[37] IR absorption spectra from H-adsorbed Ge(001) also showed monohydride-related features.[38] However, high-resolution EELS revealed the coexistence of a small dihydride phase following room temperature adsorption of hydrogen or deuterium.[39] More recent TPD studies, including our own,[40] have also shown a low temperature shoulder attributed to the formation of a small amount of the dihydride phase following high hydrogen exposures.[41]

2.6. Dopant and Ge surface segregation during growth

Modern microelectronic device fabrication requires precise control of doping concentration and depth distributions. The ideal dopant should have high incorporation probabilities, high electrical activation, and not affect matrix growth kinetics. However, dopant atoms have different covalent radii, surface energies, and bonding energies than the matrix atoms and therefore, often exhibit strong surface segregation. Surface segregation during film growth results in dopant accumulation at the film surface with surface-to-bulk concentration ratios over 1000.[42]

Greene et al.[42] developed a surface segregation model in which the segregation flux is driven by the variation in the free energy at the surface and the strain energy and is controlled by the dopant diffusion coefficient. At elevated film temperatures, dopant surface segregation approaches equilibrium values and the ratio between surface concentration (θ_s) and bulk concentration (x) decreases with increasing temperature. The segregation ratio r_s is given by,[42]

$$r_s = \frac{\theta_s}{x} = \frac{1-\theta_s}{1-x}\exp\left(-\frac{\Delta H_s}{kT_s}\right) \tag{2.11}$$

where ΔH_s is the Gibbsian segregation enthalphy. At low temperatures, where the segregation rate is less than the film growth rate, segregation becomes kinetically limited and $r_s(T_s)$ decreases with decreasing temperature. The transition temperature T^* between kinetically-limited and equilibrium dopant segregation decreases with decreasing film growth rate.[42]

2.7. References

1. S. Solmi, E. Landi, and F. Baruffaldi, J. Appl. Phys. 68, 3250 (1990).

2. P. Hirsch, A. Howie, R. Nicholson, D.W. Pashley, and M.J. Whelan, *Electron Microscopy of Thin Crystals*, (Krieger Publishing Company, Malabar, FL 1977), p. 263.

3. P.A. Stolk, H.J. Gossmann, D.J. Eaglesham, and J.M. Poate, Nuc. Inst. Methods Phys. Res. B **96**, 187 (1995) and S. Takeda, Jpn. J. Appl. Phys. **30**, L639 (1991).

4. W. Wijaranakula, J. Appl. Phys. **74**, 3783 (1993).

5. A. Armigliato, D. Nobili, P. Ostoja, M. Servidori, and S. Solme, in *Semiconductor Silicon 1977*, edited by H. Huff and E. Sirtl (The Electrochemical Society, Princeton, NJ, 1977), Vol. 77-2, p. 638.

6. G.L. Vick and K.M. Whittle, J. Electrochem. Soc. **119**, 1142 (1969).

7. F.N. Schwettman, J. Appl. Phys. **45**, 1918 (1974).

8. S. Solmi, E. Landi, and F. Baruffaldi, J. Appl. Phys. 68, 3250 (1990).

9. W. Wijaranakula, J. Appl. Phys. **74**, 3783 (1993).

10. S. Takeda, Jpn. J. Appl. Phys. **30**, L639 (1991)., and A. Bourret, Institute of Physics Conf. Series **87**, 39 (1987).

11. P.M. Fahey, P.B. Griffin, and J.D. Plummer, Rev. Mod. Phys. **61**, 289 (1989).

12. N. Nakano, L. Marville, and R. Reif, J. Appl. Phys. **72**, 3641(1992)., and N. Nakano, L. Marville, and R. Reif, J. Appl. Phys. **72**, 1961(1992).

13. K. Uwasawa, T. Uchida, T. Ikezawa, M. Hane, T. Matsuki, H. Kato, and K. Ishida, International Electron Device Meeting, San Francisco, CA, Dec. 11-14 1994, p. 873.

14. P.A. Stolk, H.-J. Gossman, D.J. Eaglesham, and J.M. Poate, Mat. Sci. Eng. B, **36**, 275 (1996), M.D. Johnson, M.J. Caturla, and T.D. de la Rubia, J. Appl. Phys. **84**, 1963 (1998).

15. J. Zhu, T.D. de la Rubia, L.H. Yang, C. Mailhiot, G.H. Gilmer, Phys. Rev. B **54**, 4741 (1996); Appl. Phys. Lett. **74**, 3657 (1999).

16. ed. E. Emin Boron Rich Solids AIP Conf. No. 140 1986., and J. Yamauchi, N. Aoki, and I. Mizushima Phys. Rev. B **55**, R10245(1997).

17. W.H.E. Schwarz, L. Mensching, K.H. Hallmeier, and R. Szargan, Chem. Phys. **82**, 57 (1983).

18. L.J. Terminello, A. Chaiken, D.A. Lapiano-Smith, D.L. Doll, and T. Sato, J. Vac. Sci. Technol. A **12**, 2462 (1994).

19. See for example J. Stöhr, *NEXAFS Spectroscopy*, Springer Series in Surface Science, Vol. 25 (Springer, New York, 1996) and references therein.

20. P. A. Redhead, Vacuum **12**, 203 (1962).

21. D. A. King, Surface Science **47**, 384 1975).

22. F. M. Lord and J. S. Kittelberger, Surface Science **43**, 173 (1974).

23. J. A. Appelbaum, G. A. Baraff, and D. R. Hamann, Phys. Rev. **B14**, 588 (1976).

24. R. J. Hamers, R. M. Tromp, and J. E. Demuth, Phys. Rev. **B34**, 5343 (1986).

25. R. M. Tromp, R. J. Hamers, and J. E. Demuth, Science **234**,304 (1986).

26. F. Stucki, J.A. Schaefer, J.R. Anderson, G.J. Lapeyre, and W. Gŏpel, Solid State Communications, **47**, 795 (1983).

27. T. Sakurai and H.D. Hagstrom, Phys. Rev. **B14**, 1593 (1976).

28. S. Ciraci, R. Butz, E.M. Oellig, and H. Wagner, Phys. Rev. **B30**, 711 (1984).

29. Y.J. Chabal and K. Raghavachari, Phys. Rev. Lett. **54**, 1055 (1985).

30. K. Sinniah, M.G. Sherman, L.B. Lewis, W.H. Weinberg, J.T. Yates, and K.C. Janda, J. Chem. Phys. **92**, 5700 (1990).

31. P. Gupta, V. L. Colvin, and S.M. Goerge, Phys. Rev. **B37**, 8234 (1988).

32. A.M. Greenlief, S. M. Gates, and P. A. Holbert, Chem. Phys. Lett. **159**, 202 (1989).

33. M. L. Wise, B. G. Koehler, P. Gupta, P. A. Coon, and S.M. Goerge, Surf. Sci. **258**, 166 (1991).

34. M. C. Flowers, N. B. H. Jonathan, Y. Liu and A. Morris, J. Chem. Phys. **99**, 7038 (1993).

35. J.J. Boland, Advances in Physics, **42**, 129 (1993).

36. U. Höfer, L. Li, and T.F. Heinz, Phys. Rev. **B45**, 9485 (1992).

37. L. Surnev and M. Tikhov, Surface Science **138**, 40 (1984).

38. Y. J. Chabal, Surface Science **168**, 594 (1986).

39. L. Papagno, X. Y. Shen, J. Anderson, G. Schirripa Spàgnolo, and G. J. Lapeyre, Phys. Rev. **B34**, 7188 (1986).

40. H. Kim, P. Desjardins, J. R. Abelson and J. E. Greene, Phys. Rev. B. in press.

41. S. M. Cohen, T. I. Hukka, Y. L. Yang, and M. P. D'evelyn, Thin Solid Films **225**, 155 (1993).

42. S. A. Barnett and J. E. Greene, Surf. Sci. **151**, 67 (1985).

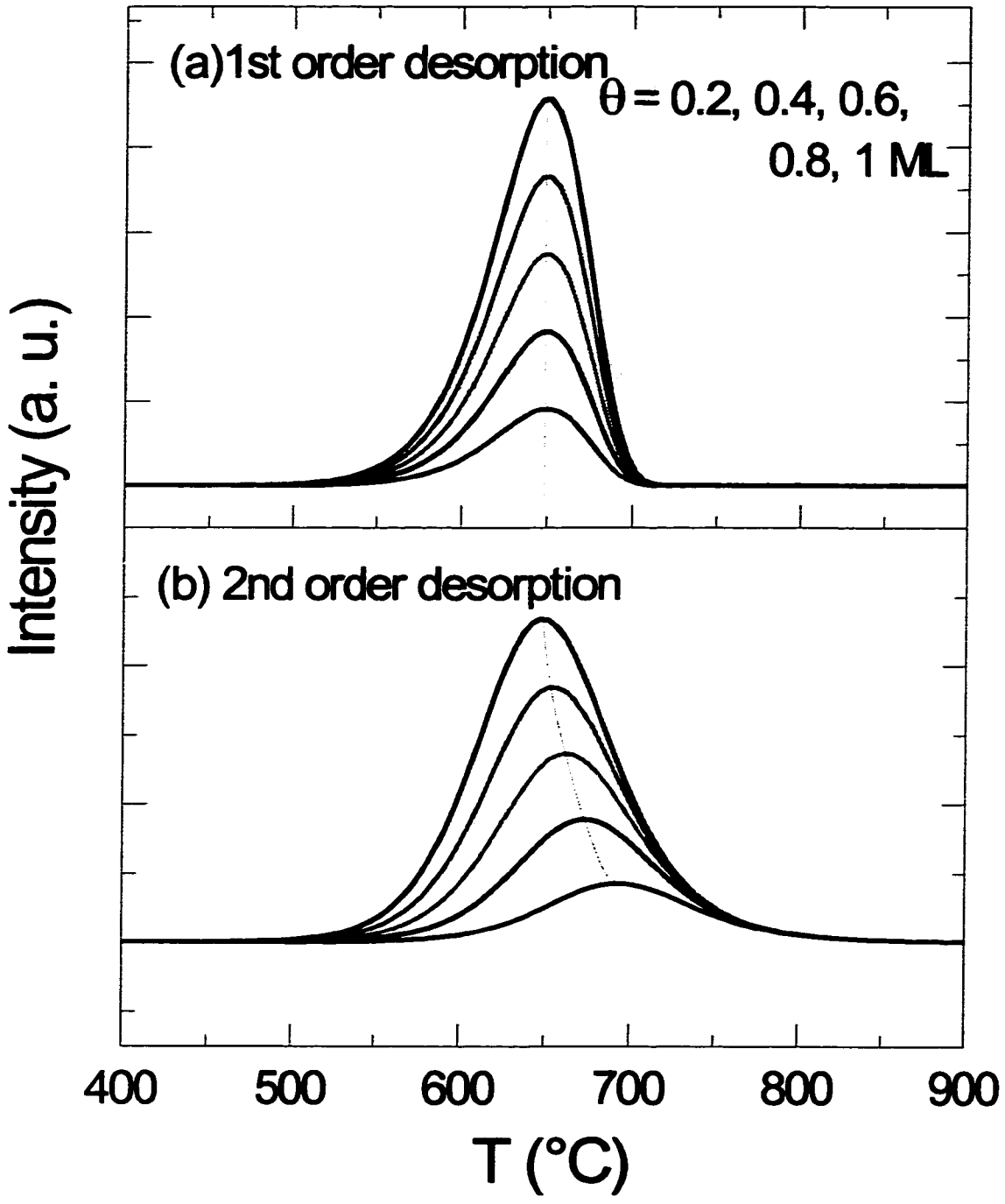

Figure 2.1. Simulated TPD spectra showing the difference between (a) first order and (b) second order desorption.

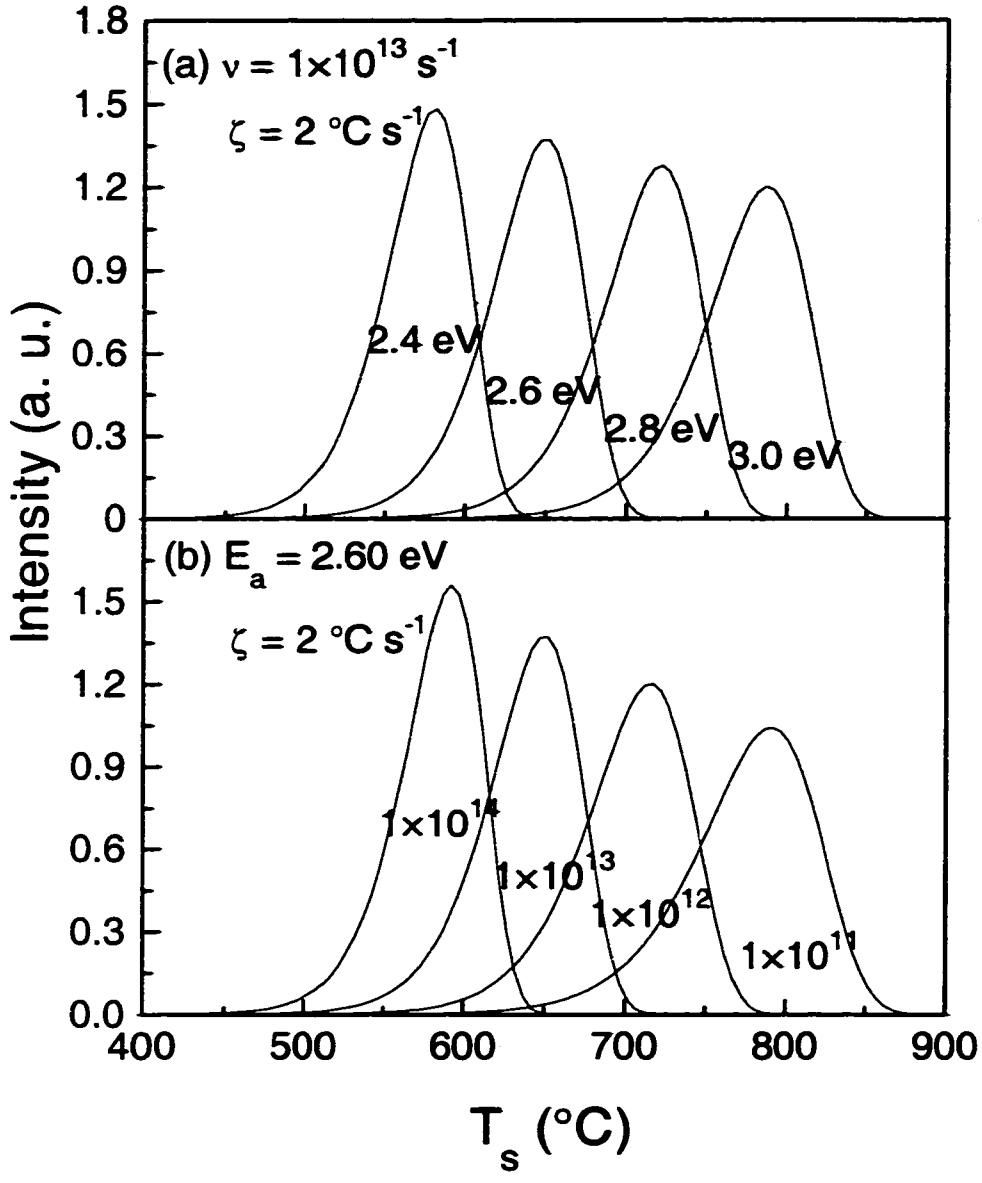

Figure 2.2. Simulated TPD spectra for first-order desorption showing the effects of (a) activation energy and (b) pre-exponential factor.

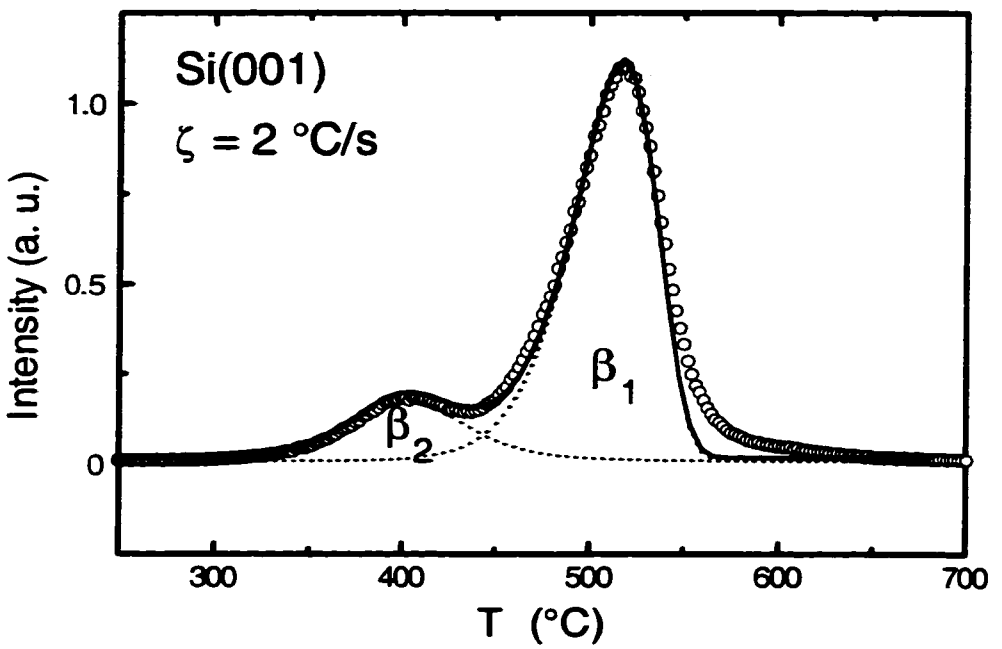

Figure 2.3. D_2 TPD spectrum from deuterium saturated Si(001). Solid lines are calculated spectra.

CHAPTER 3. Experimental procedures

3.1. Gas-source molecular-beam epitaxy system

All layers were grown in the stainless steel multi-chamber ultra-high vacuum system shown schematically in Fig. 3.1. The system is evacuated using a combination of ion and turbomolecular pumps to provide a base pressure of $\approx 1\times10^{-10}$ Torr in the transfer chamber and $\approx 5\times10^{-11}$ Torr in the growth, analysis, and STM chambers. Samples are introduced via a high-vacuum load-lock to the transfer chamber, with a maximum pressure during transfer of 1×10^{-7} Torr. The growth chamber, equipped with reflection high-energy electron diffraction (RHEED) and a quadrupole mass spectrometer (QMS), is connected to an analytical station containing provisions for Auger electron spectroscopy (AES), electron energy loss spectroscopy, and low-energy electron diffraction (LEED). TPD measurements are performed in a chamber attached to the analytical station and containing a heavily differentially-pumped Extrel QMS.

B-doped $Si_{1-x}Ge_x(001)$ layers were grown from Si_2H_6, Ge_2H_6 and B_2H_6 molecular beams delivered to the substrate through individual directed tubular dosers located 3 cm from the substrate at an angle of 45°. The dosers are coupled to feedback-controlled constant-pressure reservoirs in which pressures are separately monitored using capacitance manometers whose signals are in turn used to control variable leak valves. Valve sequencing, pressures, gas flows, and substrate temperature are all computer controlled.

3.2. Substrates and cleaning procedure

The Si(001) substrates were 1x3 cm^2 plates cleaved from 0.5-mm-thick n-type (resistivity = 23-28 Ω-cm, n = $1\text{-}2\times10^{14}$ cm^{-3}) wafers. Initial cleaning consisted of degreasing by successive rinses in warm trichloroethane, acetone, propanol, and deionized water. The substrates were then subjected to four wet-chemical oxidation/etch cycles consisting of the following steps: 2 min in a 2:1:1 solution of H_2O:HCl:H_2O_2, rinse in fresh deionized water, and a 30 s etch in dilute (10%) HF. They were blown dry with ultra-high-purity N_2, exposed to a UV/ozone treatment which consists of UV irradiation from a low-pressure Hg lamp (15 mW-cm^{-2}) for 30 minutes in air to remove C-containing species,[1] and introduced into the deposition system through the transfer chamber. The substrates were degassed at 600 °C for 4 h, cooled to 200 °C, and then rapidly heated at ≈ 100 °C-s^{-1} to 1100 °C for 1 min to remove the oxide. The pressure increase during oxide desorption was ≤ 3×10^{-9} Torr for a duration of less than 10 s.

Substrates processed using the above procedure exhibited 2×1 RHEED patterns consisting of well-defined diffraction spots, rather than streaks, with sharp Kikuchi lines and essentially equi-intense fundamental and half-order reflections. The layer surfaces were thus atomically smooth with relatively large terraces. No C or O was detected by *in-situ* AES. Substrate temperatures were determined using Pt-Rh thermocouples calibrated by optical pyrometry.

Undoped Si buffer layers, 200 Å thick for Hall-effect samples and 6000 Å for all others, were grown at 800 °C prior to commencing $Si_{1-x}Ge_x$(001):B film growth. The buffer

layers serve two purposes. They cover any remaining surface contamination while simultaneously providing a more uniform distribution of terrace lengths.[2]

3.3. Sample characterization

TPD measurements were carried out *in-situ*. Following Si(001):B growth, the films were quenched to < 200 °C and exposed to atomic deuterium until saturation coverage. For this purpose, D_2 was delivered through a doser identical to those described above, but with a hot W filament near the outlet to crack the gas. All H was exchanged for D as demonstrated by TPD. The TPD experiments themselves have no measurable effect on B surface segregation, as shown by the fact that the ratio of the B (KLL 179 eV) to Si (LMM 92 eV) AES peak intensities remain constant, and successive TPD measurements yield identical results. For TPD analyses, samples were heated at a linear rate of 2 °C s^{-1}. The experiments were performed with the sample 2 mm from the 5-mm-diameter hole in the skimmer cone of a heavily differentially-pumped Extrel QMS. Deuterium was employed rather than hydrogen in order to suppress the background signal.

Deposited film thicknesses were measured using microstylus profilometry while B concentrations in as-deposited layers were determined using a Cameca IMS-5F secondary ion mass spectrometer (SIMS) operated with a 10 keV O_2^+ primary ion beam to detect ^{11}B. Quantification, with an experimental uncertainty of ±10%, was accomplished by comparison to B ion-implanted bulk $Si_{1-x}Ge_x(001)$ standards with x within ± 1% of experimental layer value. Other than intentionally introduced B, the films contained no detectable impurities.

High resolution x-ray diffraction (HR-XRD) measurements were performed using a Philips X'pert four-axis diffractometer with a collimating x-ray mirror, Bartels four-crystal Ge(022) monochromator, and an Euler sample cradle with independent computer-controlled drive of all sample rotation angles. The instrument is capable of positioning samples to within 1 arc-s. Cu $K\alpha_1$ radiation (λ = 1.540597 Å) with angular divergence < 12 arc-s and a wavelength spread of $\approx 2\times10^{-5}$ was incident at an angle ω with respect to the sample surface. Overview ω-2θ scans (θ is the diffraction angle) were performed using a wide-aperture ($\approx 2°$) detector with a rotation rate twice that of the sample. In order to investigate the orientation dependence of x-ray scattering distributions from the films, the detector acceptance was reduced to $\approx$ 12 arc-s by placing a three-reflection Ge crystal analyzer between the sample and the detector. High-resolution reciprocal space maps were then constructed from successive ω-2θ scans, centered at different values of ω. Recorded intensities are plotted as two-dimensional topographical contour maps as a function of wavevector perpendicular $k_\perp$ and parallel $k_\parallel$ to the surface.

Resistivity and Hall-effect measurements were carried out as a function of temperature between 25 and 300 K. Samples were measured in the van der Pauw configuration[3] with ohmic contacts formed by evaporating Al through a mask and annealing the sample in high vacuum at 300 °C for 60 s. In-clad Pt electrical leads were soldered to the Al contacts. The magnetic field strength for the Hall measurements was 10 kG. Lightly doped n-type substrates ($n = 1\times10^{14}$ cm^{-3}) were used in order to create a large depletion layer which extends deep (3-3.5 μm) into the substrate while being of negligible width (< 30 Å) in all films in this study ($p = 10^{17}$-10^{22} cm^{-3}) due to the large difference in doping levels.[4] The depletion region

electrically isolates the substrate from the film during measurement. The minimum film thickness for Hall effect samples was 1500 Å.

Cross-sectional transmission electron microscopy (XTEM) examinations were performed in a Philips CM12 microscope operated at 120 kV while high-resolution lattice images were obtained at 300 kV using an Hitachi H9000 microscope. XTEM samples were scribed and cleaved into 2x4 mm^2 pieces which were glued film-to-film and then cut with a diamond saw into 2×1.5 mm slabs approximately 0.4 mm thick. The samples were then glued to pyrex glass plates and polished from both sides with 500 grit SiC paper then with 0.3 μm alumina polishing wheels to reduce the total thickness to 20-25 μm. Final thinning to electron transparency was achieved by Ar^+ ion milling from both sides. The incident beam angle and energy were progressively reduced from 15 to 11° and 5 to 3.5 keV in order to minimize radiation damage artifacts and to obtain samples with relatively even thickness distributions. The samples were cooled during ion milling such that their temperature never exceeded 100 °C.

NEXAFS spectra, using both the total electron yield (TEY) and the fluorescence yield (FY) detection techniques, were acquired near the B 188 eV *K*-edge at the Canadian Grasshopper beamline of the Synchrotron Radiation Center (SRC) in Stoughton, Wisconsin.[5] Pressure during NEXAFS measurements was 1×10^{-8} Torr. TEY data was acquired by measuring the current required to maintain charge neutrality of the ungrounded sample with respect to ground. FY data was acquired with a high-voltage channel-plate detector. In the energy range used in these experiments, TEY is more surface sensitive, with electron escape depths of ~ 10 Å, while FY is essentially a bulk probe, with fluorescence depths > 1000 Å.[5]

3.4. References

1. J.P. Noel, J.E. Greene, N.L. Rowell, S. Kechang, and D.C. Houghton, Appl. Phys. Lett. **55**, 1525 (1989), X.J. Zhang, G. Xue, A. Agarwal, R. Tsu, M.A. Hasan, J.E. Greene, and A. Rockett, J. Vac. Sci. Technol. A **11**, 2553 (1993).
2. P. Desjardins and J.E. Greene, J. Appl. Phys. **79**, 1423 (1996).
3. L.J. van der Pauw, Philips Res. Rep. **13**, 1 (1958).
4. B.G. Streetman, *Solid State Electronic Devices*, 3rd ed. (Prentice Hall, Englewood Cliffs, N.J.).
5. M. Kasrai, Z. Yin, G.M. Bancroft, and K.H. Tan, J. Vac. Sci. Technol. A **11** 2694 (1993).

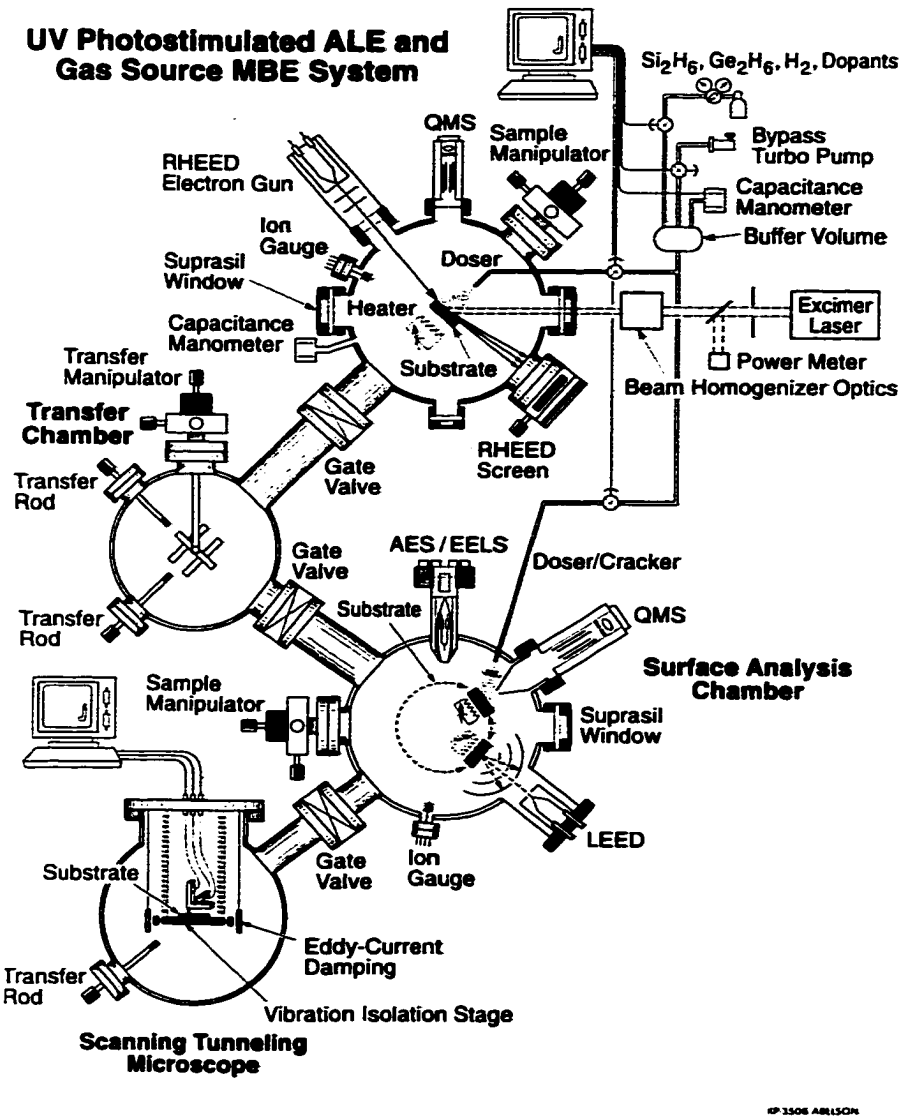

Figure 3.1. Schematic drawing of the multi-chamber GS-MBE growth and analysis system.

CHAPTER 4. Si(001):B gas-source molecular-beam epitaxy: Boron surface segregation and its effect on film growth kinetics

4.1. Introduction

In this chapter, I present the results of experiments utilizing *in-situ* D_2 temperature programmed desorption (TPD) and Auger electron spectroscopy (AES) to determine B surface coverages θ_B as a function of C_B ($5x10^{16}$-$1.7x10^{22}$ cm^{-3}) and T_s (500-800 °C) during GS-MBE Si(001):B growth. This data is used to explain the complex layer growth kinetics via a model accounting for B-induced changes in surface dangling bond density and H desorption kinetics.

4.2. Results

4.2.1. Film growth

Doped Si(001) layers, 0.12-0.20 μm thick, were grown at $T_s = 500$ to 800 °C with B concentrations C_B between $5x10^{16}$ and $1.7x10^{22}$ cm^{-3}. Typical zero-order Laue-zone RHEED patterns are shown in Fig. 4.1. Films grown at $T_s \leq 600$ °C with $C_B \lesssim 5x10^{19}$ cm^{-3} exhibited 2x1 patterns consisting of well-defined diffraction spots, rather than streaks, with sharp Kikuchi lines and essentially equi-intense fundamental and half-order reflections. The layer surfaces were thus atomically smooth with relatively large terraces. The RHEED pattern in Fig. 4.1a is from a film grown at $T_s = 550$ °C with $C_B = 8.5x10^{19}$ cm^{-3}. At higher B concentrations, the reflections become streaky as shown in Fig. 4.1b for a film with

$C_B = 2x10^{21}$ cm^{-3} ($T_s = 550$ °C), the fundamental rods broaden, the half-order to fundamental rod intensity ratio decreases, and the amount of diffuse scattering increases; all are indicative of increased atomic-scale surface roughening.

RHEED patterns from films grown with $C_B \gtrsim 5x10^{19}$ cm^{-3} at $T_s = 700$ °C and $\gtrsim 1x10^{19}$ cm^{-3} at 800 °C exhibit, in addition, indications of larger-scale surface roughening. An example is presented in Fig. 4.1c for a film with $C_B = 3.5x10^{20}$ cm^{-3} ($T_s = 800$ °C). Streaks, inclined with respect to the surface normal at angles of 25.2°, signifying the presence of {113} facets, are visible emanating from the tops and bottoms of both fundamental and half-order diffraction rods. (113 facets have also been observed by XTEM in B-doped solid-source MBE Si films grown at $T_s = 600$ °C with $C_B > 1x10^{17}$ cm^{-3}.)[1] With still higher B concentrations, $C_B > 10^{21}$ cm^{-3}, three-dimensional transmission diffraction patterns were observed at $T_s \geq 700$ °C indicating an extremely rough surface. A typical result is shown in Fig 4.1d. TEM, XTEM, and HR-XRD reciprocal lattice mapping revealed no indication of dislocations or other extended defects in films with $C_B < 5x10^{20}$ cm^{-3}. The primary defects observed in films with higher B concentrations were {111} stacking faults.

Figure 4.2 shows undoped GS-MBE Si(001) growth rates as a function of temperature for a Si_2H_6 flux $J_{Si_2H_6} = 2.2x10^{16}$ cm^{-2} s^{-1}. The curve follows the general form expected for chemical vapor deposition in which R saturates at high temperatures in an impingement-flux-limited growth mode while at low temperatures R decreases exponentially with $1/T_s$ indicative of surface-reaction-limited growth. For the Si_2H_6 flux used in the present experiments, temperature ranges for flux-limited and reaction-limited regimes are $T_s \gtrsim 750$ °C and $T_s \lesssim 625$ °C, respectively. The calculated curve in Fig. 4.2 shows that the undoped $R(T_s)$ data

are well described by a model, developed in reference 2, based upon dissociative Si_2H_6 chemisorption followed by a series of surface decomposition reactions with the rate-limiting step being first-order hydrogen desorption from Si monohydride. The model contains no fitting parameters.

I find, in agreement with reference 3, that the use of B_2H_6 to provide B doping at concentrations up to $\approx 10^{19}\,cm^{-3}$ has no significant effect on GS-MBE Si growth rates. However, concurrent B doping during GS-MBE Si(001) with incident B_2H_6/Si_2H_6 flux ratios greater than ≈ 0.005, corresponding to $C_B \gtrsim 1.5x10^{19}\,cm^{-3}$ at $T_s = 550\,°C$ to $1x10^{20}$ at 800 °C, decreases the negative slope of $R(T_s)$ in the surface reaction limited regime. This has the effect of increasing R at low growth temperatures and decreasing it at higher temperatures as shown in Fig. 4.2 for Si(001):B films grown with $C_B = 1x10^{20}\,cm^{-3}$.

Figure 4.3 is a plot of R as a function C_B for 200-nm-thick films grown at $T_s = 550$, 600, 700, and 800 °C. The incident B_2H_6 flux was increased from $2.2x10^{12}$ to $6.6x10^{16}\,cm^{-2}\,s^{-1}$ ($J_{B_2H_6}/J_{Si_2H_6} = 1x10^{-4}$ to 3 with $J_{Si_2H_6}$ maintained at $2.2x10^{16}\,cm^{-2}\,s^{-1}$). R remains constant with increasing B concentrations up to $\approx 10^{19}\,cm^{-3}$, as noted above. At higher B doping levels, however, R increases by $\approx$ 50% at $T_s = 550$ °C (and by 60% at 500 °C, not shown). With $T_s \geq 600$ °C, R decreases by comparable fractions and the B concentration range over which the growth rate change is observed increases with increasing growth temperatures.

Typical SIMS profiles through a B modulation-doped sample are presented in Fig. 4.4. The Si(001) film was grown at $T_s = 600$ °C with successive B-doped regions deposited for the same time and separated by 0.25-μm-thick undoped buffer layers. $J_{Si_2H_6}$ was constant at

$2.2x10^{16}$ cm^{-2} s^{-1} while $J_{B_2H_6}$ was varied to provide C_B values from $1.7x10^{18}$ to $4.7x10^{20}$ cm^{-3}. In the more than 60 films grown for these experiments, there was no measurable B segregation in layers with $C_B \lesssim 2x10^{18}$ cm^{-3}. SIMS profiles from these layers are essentially flat with the leading and trailing edges abrupt to within the experimental resolution, 8 nm per concentration decade. At higher B concentrations, however, significant B segregation is observed. The B incorporation probability during Si film growth is initially depressed, giving rise to SIMS profiles with "missing" B at the back side, as B accumulates at the surface until a steady-state ratio r_B of the surface to bulk B fractions is achieved. The value of r_B depends upon T_s, R, and $J_{B_2H_6}$. After turning off the B_2H_6 flux, the excess B at the surface acts as a reservoir to continue doping what was intended to be undoped buffer layers. A comparison of the widths of the profiles in Fig. 4.4 clearly shows, in agreement with the results in Fig. 4.3, that the Si deposition rate at 600 °C decreases with increasing C_B at high $J_{Si_2H_6} / J_{B_2H_6}$ ratios.

4.2.2. TPD measurements

Typical D_2 TPD results from B-doped Si(001) films are reproduced in Figs. 4.5 and 4.6. Spectra from films with B concentrations less than $\approx 1x10^{18}$ cm^{-3} (see, for example, Fig. 4.5a) are identical to those from clean Si(001) surfaces.[4] They consist of two peaks, labeled β_2 and β_1, due to desorption from the 1x1 dideuteride phase and the 2x1 monodeuteride phases, respectively. The peaks are centered at 405 and 515 °C. While β_2 desorption is second order, β_1 follows first order kinetics, except at very low deuterium coverages $\theta_D < 0.1$ ML,[5] due to π-bonding-induced pairing of dangling bonds on single dimers.[6]

At higher B concentrations, the TPD spectra change dramatically. The D_2 desorption onset temperature is reduced, the desorption features are broadened indicative of the presence of additional peaks, the high-temperature feature decreases in intensity while the low-temperature feature increases, and the total integrated area under the peaks decreases. Figures 4.5b, 4.5c, 4.5d, and 4.5e are TPD spectra from $T_s = 550$ °C Si(001) layers with $C_B = 9x10^{18}$, $4x10^{19}$, $2.5x10^{20}$ and $5.3x10^{20}$ cm^{-3}, respectively. The positions of the β_1 and β_2 peaks remain constant while two new peaks emerge, one at low temperature and one between the β_1 and β_2 peaks. The new low-temperature peak reduces the deuterium desorption onset temperature from 320 °C for Si(001) with $C_B \lesssim 1x10^{18}$ cm^{-3} to ≈ 250 °C with $C_B = 5.3x10^{20}$ cm^{-3}. Similar results were obtained with Si(001):B films grown at 600 °C except for an increase in the intensity ratio between the high-temperature and low-temperature features and in the total integrated area under the peaks. Thus, the 600 °C spectra are essentially identical to 550 °C spectra obtained from samples with lower B concentrations. An example TPD spectrum from a $T_s = 600$ °C film with $C_B = 4x10^{19}$ cm^{-3} (compare with Fig. 4.5c) is shown in Fig. 4.5f.

TPD spectra from layers with $C_B > 1x10^{19}$ cm^{-3} grown at higher temperatures follow the general trends observed in 600 °C samples, but become increasingly distorted as T_s is increased. Figure 6 shows TPD spectra from 800 °C films with $C_B = 2x10^{19}$, $1.2x10^{20}$, $3.5x10^{20}$, and $1.5x10^{21}$ cm^{-3}. The high-temperature TPD features are much wider than those observed at lower growth temperatures and overlap the low-temperature TPD features. In addition, at B concentrations $\gtrsim 10^{21}$ cm^{-3}, a new peak emerges near 300 °C and continues to increase in intensity. This peak strongly resembles the TPD feature in Fig. 4.7 obtained from

an amorphous B film grown from B_2H_6 at 600 °C. The a-B layer was thick enough that no Si substrate signal was detected by AES.

4.2.3. Calculated TPD spectra

All TPD spectra from B-doped epitaxial Si(001) layers were fitted using the standard Polanyi-Wigner analysis in which the desorption rate $d\theta_D/dT$ is expressed as[7]

$$\frac{d\theta_D}{dT} = \left(\frac{\nu\theta_D^n}{\zeta}\right)\exp(-E_d/kT) \tag{4.1}$$

where v is the attempt frequency, θ_D is the instantaneous D coverage, n is the order of the desorption reaction, ζ is the sample heating rate, E_d is the desorption activation energy, and k is Boltzmann's constant. At high pumping speeds,[8]

$$\ln\left(\frac{\theta_D(T)}{\theta_o}\right) = \frac{\nu}{\zeta}I(T) \tag{4.2}$$

for first-order desorption and

$$\theta_D(T) = \frac{\theta_o}{1+\left(\frac{\nu}{\zeta}\right)\theta_o I(T)} \tag{4.3}$$

for second-order desorption. θ_o in equations 4.2 and 4.3 is the initial coverage and I(T) is given by

$$I(T) = \frac{E_d}{k}\left|\frac{e^{-\varepsilon}}{\varepsilon^2}\sum_{n=1}^{\infty}\frac{(-1)^{n+1}n!}{\varepsilon^{n-1}}\right|_{To}^{T} \tag{4.4}$$

in which $\varepsilon = E_d/kT$.

Spectra from samples with $C_B \lesssim 1\times10^{18}$ cm^{-3}, such as the results shown in Fig. 4.5a, were fitted with E_d and v equal to 1.88 eV and 1×10^{13} s^{-1} for β_2 and 2.52 eV and 1×10^{15} s^{-1} for

β_1 as previously obtained for D_2 TPD from clean bulk Si(001) surfaces.[4] The agreement between measured and calculated spectra is very good except at high temperatures where the measured curves for both bulk Si(001) and the Si(001):B films are higher than the calculated curves due to the fact that β_1 desorption deviates from first-order kinetics at low deuterium (and hydrogen) coverages.[9]

All D_2 TPD spectra from films grown at T_s = 500-600 °C with C_B between $2x10^{18}$ and $3x10^{20}$ cm^{-3} were found to be well fit with four peaks: the initial β_2 and β_1 peaks together with two lower-temperature B-induced β_1^* and β_2^* peaks at 330 and 470 °C. Examples of fitted spectra are shown in Figs. 4.5b-4.5d for 550 °C and Fig. 4.5f for 600 °C samples. Best fit values for E_d and v are 1.56 eV and $1x10^{12}$ s^{-1} for β_2^* and 2.29 eV and $3x10^{14}$ s^{-1} for β_1^*, both peaks second order, again in agreement with our previous results for bulk Si(001) surfaces with known B coverages.[4]

TPD spectra from Si(001) films grown at $T_s \leq 600$ °C, but with $C_B > 5x10^{20}$ cm^{-3}, were also well fit using the above parameters except at the low temperature side where they exhibited an additional peak centered near 300 °C (see, for example, Fig. 4.5e). We believe that this new feature is an indication that the surface B coverage has exceeded the saturation value $\theta_{sat,B}$ of 0.5 ML and is due to desorption from surface B-D bonds consistent with the D_2 TPD spectra in Fig. 4.7 from an amorphous B film on Si.

At T_s = 700 and 800 °C with $C_B \gtrsim 5x10^{19}$ and $1x10^{19}$ cm^{-3}, respectively, where RHEED patterns from Si(001) layers reveal the existence of 113 facets, the TPD spectra are more complex as shown in Fig. 4.6. These results could not be fit with the same four peaks. The measured high-temperature features were much wider than β_1 and the β_2^* peak position

did not match the low-temperature feature. Further attempts to fit these spectra would have to include desorption from 113 facets. The unreconstructed Si(113) surface consists of alternating single-atom-wide 001 and 111 steps in the $[33\bar{2}]$ direction while the reconstructed Si(113)3x2 surface is composed of dimers along $[1\bar{1}0]$ on 001 steps and adatoms rebonded across 001 and 111 steps.[10] There are no reported hydrogen desorption results for Si(113).

4.2.4. B surface coverage

At all growth temperatures investigated, the total integrated TPD intensity decreased with increasing C_B. Examples were presented in Fig 4.5 for $T_s = 550$ °C. These results show that the saturated deuterium coverage decreases with increasing B concentration in the films. This is due to the rapid decrease in β_1 while the integrated intensity under β_1^* increases slowly with increasing C_B. Ion channeling, cross-sectional transmission electron microscopy, and electrical measurements[11] together with STM analyses[12,13] have shown that trivalent B atoms deposited on Si(001) move, primarily due to their smaller size,[4] to the second atomic layer and have a saturation coverage of 0.5 ML. Based upon STM results,[12,13] the primary B-induced Si(001) surface reconstruction at high coverages is a c4x4 structural subunit containing four second-layer B atoms, two first-layer Si dimers having B backbonds, an unmodified first-layer Si dimer with Si backbonds, and a dimer vacancy. Thus, the decrease we observe in β_1 with increasing B concentration can be understood as being due to both B-induced dimer vacancies and a decrease in the dangling bond density associated with Si dimers having Si backbonds while the increase in β_1^* is due to the rising number density of Si dimers with B backbonds.

The overall decrease in θ_D with increasing C_B, and hence θ_B, is caused by two primary factors. The first is simply the fact that the Si dimer vacancy population increases in direct proportion to θ_B. This effect is exacerbated, however, by the partial deactivation of Si^* (where Si^* signifies a B-backbonded Si adatom) dangling bonds resulting from charge transfer from Si^* adatoms to subsurface B, similar to the case for B/Si(111)$\sqrt{3}\times\sqrt{3}$ in which charge transfer was deduced from tunneling spectra.[14] The Si-B bond length, 2.0-2.1 Å,[15] is considerably shorter than Si-Si, 2.35 Å, and B has both a higher electronegativity than Si and an empty sp^3 orbital. Using measured β_1 and β_1^* integrated TPD peak intensities from bulk Si(001) wafers with known B coverages,[4] we find that approximately one dangling bond per Si^* dimer is deactivated.

The deactivation of Si dangling bonds reduces the tendency for D atoms to pair up on single dimers and thus leads to the observed second-order β_1^* desorption kinetics. The lower activation energies measured for deuterium desorption from Si^*-D and Si^*-D_2 compared to Si-D and Si-D_2 result from the combination of Si^*-B backbond charge transfer and the additional strain in Si^* dimers.

Based upon the ordered c4x4 B subunit described above, the normalized coverage $\theta_{n,Si}$ of surface Si dimer atoms with Si backbonds decreases with increasing θ_B as

$$\theta_{n,Si} = 1 - 1.5\theta_B \qquad (4.5)$$

and is represented by the solid line in Fig. 4.8. At the same time, the normalized coverage θ_{n,Si^*} associated with Si^* dimer atoms increases from 0 to 0.50. However, since approximately half of these latter dangling bonds are deactivated, the effective value of θ_{n,Si^*} is

$$\theta_{n,Si^*} \simeq 0.5\theta_B \qquad (4.6)$$

as given by the dashed line in Fig. 4.8. The normalized integrated intensities under the $\bullet_1$ and β_1^* TPD peaks I_{n,β_1} and I_{n,β_1^*} are also plotted in Fig. 4.8. B coverages in this case were obtained by setting the measured ratio $I_{n,\beta_1^*}/I_{n,\beta_1} = \theta_{n,Si^*}/\theta_{n,Si}$. The results show that β_1 and β_1^* TPD intensities from Si:B films grown at constant T_s vary linearly with θ_B and exhibit good agreement with $\theta_{n,Si}(\theta_B)$ and $\theta_{n,Si^*}(\theta_B)$, respectively. There is, however, a tendency for the calculated values of $\theta_{n,Si}$ and θ_{n,Si^*} to slightly overestimate I_{n,β_1} and I_{n,β_1^*} as the B coverage approaches saturation. This is due primarily to the fact that the B-induced c4x4 subunit also exists, although with lower probability, in other polymorphs[12,13] and the overall fraction of deactivated Si^* dangling bonds is actually a bit less than half.

Using the data in Fig. 4.8, the B surface coverage θ_B was plotted as a function of the bulk B concentration C_B, obtained from SIMS measurements. Fig. 4.9a shows results for $T_s = 550$ °C. Saturation B coverage, $\theta_B = 0.5$ ML, is obtained at $C_B \simeq 5\text{x}10^{20}$ cm^{-3} with $T_s = 550$ °C and $J_{Si_2H_6} = 2.2\text{x}10^{16}$ cm^{-3}.

Estimates of second-layer B surface coverages in samples for which there was no TPD evidence for B in the first atomic layer (ie, $\theta_B \leq \theta_{sat,B}$) were obtained by AES, using the B KL_2L_2 (178 eV) and Si $L_{2,3}VV$ (92 eV) lines, for comparison to θ_B values obtained by TPD. AES sensitivity factors and electron escape lengths were taken from ref. 16 and calibration was provided using a Si(111)$\left(\sqrt{3}\times\sqrt{3}\right)$ test sample which was known to have 0.33 ML of B in the third layer.[17] In analyzing the data, two limits were considered. In the first case, the B concentration in the bulk film is assumed to be constant and equal to C_B with excess segregated B located only in the second atomic layer. In case two, the excess B is evenly

distributed in the second and third atomic layer. Both sets of results are shown at Fig 4.9b and indicate, based upon the TPD data, that the majority of segregated B is in layer two with an increasingly smaller fraction of excess B in subsequent layers.

4.3. Discussion

Gibbsian surface segregation is described by the equation[18]

$$r_B = \frac{1\theta_B}{1 x_B} \exp\left(\frac{\Delta H_s}{kT_s}\right), \tag{4.7}$$

where r_B is the steady-state ratio of the surface coverage θ_B to the bulk B fraction x_B and ΔH_s is the segregation enthalpy. Expressing θ_B in terms of x_B, or C_B, and accounting for the fact that $\theta_{sat,B} = 0.5$ ML,[18-20] yields

$$\theta_B = \frac{0.5\, x_B \exp\left(\frac{\Delta H_s}{kT_s}\right)}{1 x_B + x_B \exp\left(\frac{\Delta H_s}{kT_s}\right)} = \frac{0.5\, C_B \exp\left(\frac{\Delta H_s}{kT_s}\right)}{n_{Si}\, C_B \left\{1 - \exp\left(\frac{\Delta H_s}{kT_s}\right)\right\}} \tag{4.8}$$

where n_{Si} is the bulk Si atom density, 5×10^{22} cm^{-3}. Equation 4.8 is fitted to our θ_B vs C_B data in Fig. 4.9a. Very good agreement is obtained using a segregation enthalpy $\Delta H_s = -0.53$ eV. This is the first result for GS-MBE Si:B and is in reasonable agreement with reported ΔH_s values for B in solid-source MBE Si. Krüger and Osten[19] found $\Delta H_s = -0.44$ eV in MBE Si(001):B based upon fitting SIMS depth profiles while Frésart et al.[20] obtained $\Delta H_s = -0.33$ eV in Si(111):B. In the latter case, the enthalpy was estimated using uncalibrated peak-to-peak AES measurements which, based upon our own AES results, tend to underestimate θ_B and, hence, $|\Delta H_s|$. Other comparable results for segregating species in solid-

source MBE Si(001) include the group-IV alloying element Ge, ΔH_s = -0.28 eV,[21] and oversize group-III and group-V dopants, In (ΔH_s = -0.85 eV)[22] and Sb (ΔH_s = -1.2 eV).[18]

At elevated film temperatures, dopant surface segregation approaches equilibrium values and r_B decreases with increasing temperature, while at low temperatures, where the segregation rate is of the order of or less than the film growth rate, segregation becomes kinetically limited and $r_B(T_s)$ decreases with decreasing temperature.[18] The transition T^* between kinetically-limited and equilibrium dopant segregation decreases with decreasing film growth rate.[18] For solid-source MBE Si:B, T^* was found to range from 650 °C with R = 1 μm h^{-1} to 600 °C at R = 0.36 μm h^{-1}.[23] The present case is more complex since the steady-state hydrogen coverage $\theta_H(T_s,R)$ during GS-MBE also affects the B segregation rate. Nevertheless, using the solid-source MBE results as a guideline and accounting for the relatively low Si_2H_6 fluxes used in these experiments ($J_{Si_2H_6}$ = 2.2x10^{16} cm^{-2} s^{-1} corresponding to R = 0.03-0.06 μm h^{-1} at 550 °C and 0.3-0.2 μm h^{-1} at 600 °C), it is reasonable to expect that dopant segregation at $T_s \geq$ 550 °C should be in the equilibrium regime. This is consistent with TPD spectra from films grown at 550 and 600 °C and having the same bulk B concentration (see, for example, Figs. 4.5c and 4.5f for which C_B = 4x10^{19} cm^{-3} and θ_B is 0.30 and 0.24, respectively) showing that r_B decreases with increasing T_s.

The film deposition rate during GS-MBE Si(001) from Si_2H_6 is given by[2]

$$R_{Si} = \frac{2 S_{Si_2H_6} J_{Si_2H_6}}{n_{Si}} \theta_{db}^2 . \qquad (4.9)$$

where $S_{Si_2H_6}$ is the Si_2H_6 reactive sticking probability, 0.036,[2] and θ_{db} is the dangling bond coverage. The change in the surface dangling bond density during GS-MBE of undoped Si(001) from Si_2H_6 is given by[2]

$$\frac{d\theta_{db}}{dt} = \frac{2 J_{Si_2H_6} S_{Si_2H_6} \theta_{db}^2}{N_s} + k_d (1 \ \theta_{db})^n \tag{4.10}$$

where Si_2H_6 adsorption is second order and hydrogen desorption is first order (n = 1). Thus, at steady-state,

$$\theta_{db} = \frac{N_s k_d}{4 S_{Si_2H_6} J_{Si_2H_6}} \left\{ \left(1 + \frac{8 S_{Si_2H_6} J_{Si_2H_6}}{N_s k_d} \right)^{1/2} - 1 \right\}. \tag{4.11}$$

In the case of Si(001):B, there are two types of surface Si dimer atoms, Si with Si backbonds and Si^* with B backbonds. As in equation 4.10, the total dangling bond coverage θ_{db} can be expressed as

$$\theta_{db} = f\theta_{n,Si} + f^*\theta_{n,Si^*} \tag{4.12}$$

in which $\theta_{n,Si}$ and θ_{n,Si^*} are the normalized coverages of Si and Si^* while f and f^* are the corresponding dangling-bond site fractions. Thus, for the surface Si phase, f is given by equation 4.17 above.

For Si:B film growth, we neglect the direct volume contribution of B to the film deposition rate since x_B is always less than 0.1 and for most cases of interest, less than 0.002. However, as discussed above, the presence of second-layer B atoms affects the total dangling bond coverage, which can be expressed as

$$\theta_{db} = f\theta_{n,Si} + f^*\theta_{n,Si^*} \tag{4.13}$$

in which f and f^* are the site fractions of Si and Si^* which are unoccupied by H. From equations 4.5, 4.6, and 4.8,

$$\theta_{n,Si} = \frac{n_{Si} - C_B\left\{1 - 0.25\exp\left(\frac{-\Delta H_s}{kT_s}\right)\right\}}{n_{Si} - C_B\left\{1 - \exp\left(\frac{-\Delta H_s}{kT_s}\right)\right\}} \simeq \frac{1 + 0.25\frac{C_B}{n_{Si}}\exp\left(\frac{-\Delta H_s}{kT_s}\right)}{1 + \frac{C_B}{n_{Si}}\exp\left(\frac{-\Delta H_s}{kT_s}\right)} \tag{4.14}$$

and

$$\theta_{n,Si^*} = \frac{0.25\exp\left(\frac{-\Delta H_s}{kT_s}\right)}{n_{Si} - C_B\left\{1 - \exp\left(\frac{-\Delta H_s}{kT_s}\right)\right\}} \simeq \frac{0.25\frac{C_B}{n_{Si}}\exp\left(\frac{-\Delta H_s}{kT_s}\right)}{1 + \frac{C_B}{n_{Si}}\exp\left(\frac{-\Delta H_s}{kT_s}\right)} \tag{4.15}$$

Combining equations 4.9-4.12, the growth rate of Si:B is given by,

$$R_{Si} = \frac{2 S_{Si_2H_6} J_{Si_2H_6}}{n_{Si}} \times \left(\frac{f + 0.25(f+f^*)\frac{C_B}{n_{Si}}\exp\left(\frac{-\Delta H_s}{kT_s}\right)}{1 + \frac{C_B}{n_{Si}}\exp\left(\frac{-\Delta H_s}{kT_s}\right)} \right)^2 . \tag{4.16}$$

The term f in equation 4.16 can be expressed as a function of temperature during steady-state film growth,[2]

$$f = \frac{N_s k_d}{4 S_{Si_2H_6} J_{Si_2H_6}} \left\{ \left(1 + \frac{8 S_{Si_2H_6} J_{Si_2H_6}}{N_s k_d} \right)^{1/2} - 1 \right\} \tag{4.17}$$

where $S_{Si_2H_6} = 0.036$ and $k_d(s^{-1}) = 7.9\times10^{11}\exp(-2.04eV/kT_s)$. Equation 4.17 gives $f = 0.19$, 0.49, 0.87, and 0.99 with $T_s = 550$, 600, 700, and 800 °C. An initial estimate for f^* is obtained by measuring the fractional area, up to the film growth temperature T_s, under the corresponding β_1^* TPD peak. This yields $f^* = 0.67$, 0.89, 0.99, and 1 with $T_s = 550$, 600, 700, and 800 °C. These values are expected to be underestimates, primarily due to the rapid heating

rate during TPD. Nevertheless, R vs C_B curves calculated from equations 4.16 and 4.17 using these values exhibit good agreement at $T_s \leq 600$ °C while at higher temperatures, the calculated curves, although they exhibit the correct shape, yield growth rates which are too low. Best fits were obtained using $f^* = 0.81$, 1.0, 1.4, and 2.2. These results, shown for 200-nm-thick films in Fig. 4.3, agree very well with the experimental data. The necessity of using f^* values increasingly larger than unity to describe film growth kinetics at $T_s \geq 700$ °C is due to the presence of the {113} facets giving rise to higher surface site densities. In addition, the 113 surfaces can be expected to exhibit different Si_2H_6 reactive sticking probabilities and, as shown by the TPD spectra in Fig. 4.6, different B and Si^*/Si site distributions.

Equations 4.16 and 4.17 were also used to calculate Si:B film growth rates as a function of temperature with C_B constant. $f^*(T_s)$ values were obtained from an equation similar to 4.17, but written to account for the second-order desorption kinetics observed for β_1^*,

$$f^* = \left(1 + \sqrt{\frac{2 S_{Si_2H_6} J_{Si_2H_6}}{N_S k_d^*}} \right)^{-1} \tag{4.18}$$

where $k_d^* = v^* \exp(-E^*/kT_s)$ is the hydrogen desorption rate coefficient from surface Si^* dimer atoms. Good agreement with T_s = 550 and 600 °C experimental results were obtained using $v^* = 5 \times 10^{11}$ s^{-1} and $E_d^* = 1.77$ eV, which yields f^* values similar to those obtained from direct measurements of β_1^* TPD fractional areas. An example of the agreement between calculated and measured $R(T_s)$ results is shown in Fig. 4.2 for films grown with C_B 1×10^{20} cm^{-3}. The overall fit, even at high growth temperatures where 113 facetting requires the use of f^* values greater than one, is reasonable.

The above analysis shows, as expected from the shape of the Si(001):B $R(T_s)$ curve in Fig. 4.2 and the TPD results, that the activation energy for hydrogen desorption from Si^* surface atoms with B backbonds during steady-state film growth is significantly lower than from Si-backbonded surface atoms. That is, second-layer B atoms, whose concentration is enhanced by segregation, weaken surface Si-H bonds. Thus, in the lower-temperature $T_s \leq 550$ °C surface-reaction-limited growth regime where steady-state H coverages are high, R increases with increasing C_B as shown in Figs. 4.2 and 4.3. At higher temperatures, corresponding to much lower steady-state θ_H values, the deactivation of Si dangling bonds increasingly becomes the dominant effect of second-layer B atoms and thus R decreases with increasing C_B. Note that in the flux-limited regime, where R remains essentially constant for pure Si growth, it continues to increase for Si:B. This is due to a decrease in $\theta_B(T_s)$ at high temperatures and the presence of the 113 facets.

4.4. Conclusions

I have shown in this chapter that at high B doping concentrations in Si(001) films, ordered B subunits in the second layer weaken surface Si-H bonds while deactivating Si dimer dangling bonds during film growth. These effects are exacerbated by the strong tendency for B segregation giving rise to steady state segregation ratios r_B up to 1200 at 550 °C. The segregation enthalpy ΔH_s was determined to be -0.53 eV. These results were used to model the effects of high B doping on Si:B GS-MBE growth kinetics. R increases with increasing $C_B \geq 2 \times 10^{19}$ cm^{-3} at $T_s \leq 550$ °C, where steady state H coverages are high, due to B-enhanced

H desorption rates. At $T_s \geq 600$ °C, corresponding to much lower steady state θ_H values, R decreases due to B-induced deactivation of Si dangling bonds.

4.5. References

1. X. Lu, Z. Jiang, H. Zhu, X. Zhang, and X. Wang, Appl. Phys. Lett. **68**, 3278 (1996).
2. T.R. Bramblett, Q. Lu, T. Karasawa, M.-A. Hasan, S.K. Jo, and J.E. Greene, J. Appl. Phys. **76**, 1884 (1994).
3. Q. Lu, T.R. Bramblett, N.-E. Lee, M.-A. Hasan, T. Karasawa, and J.E. Greene, J. Appl. Phys. **77**, 3067 (1995).
4. H. Kim, G. Glass, S.Y. Park, T. Spila, N. Taylor, J. R. Abelson, and J. E. Greene, Appl. Phys. Lett. **69**, 3869 (1996).
5. U. Höfer, L. Li, and T. F. Heinz, Phys. Rev. **B45**, 9485 (1992).
6. J. J. Boland, J. Vac. Sci. Technol. **A10**, 2458 (1992).
7. P. A. Redhead, Vacuum **12**, 203 (1962).
8. F. M. Lord, J. S. Kittelberger, Surf. Sci. **43**, 173 (1974).
9. G. Boishin and, L. Surnev, Surf. Sci. **345**, 64 (1966).
10. J. Knall, J. B. Pethica, J. D. Todd, and J. H. Wilson, Phys. Rev. Lett. **66**, 1733 (1991).
11. R.L. Headrick, B.E. Weir, A.F. levi, D.J. Eaglesham, and L.C. Feldman, Appl. Phys. Lett. **57**, 2779 (1990).
12. Y. Wang, and R.J. Hamers, Appl. Phys. Lett. 56, 2057 (1995), and J. Vac. Sci. Technol. **A13**, 1431 (1995).
13. Y. Wang, R.J. Hamers, and E. Kaxiras, Phys. Rev. Lett. **74**, 403 (1995).
14. Ph. Avouris, I.-W. Lyo, F. Bozso, and E. Kaxiras, J. Vac. Sci. Technol. **A8**, 3405 (1990).
15. B. E. Weir, R. L. Headrick, Q. Shen, L.C. Feldman, M. S. Hybertson, M. Needels, M. Schluter, and T. R. Hart, Phys. Rev. **B46**, 12861 (1992).
16. C. C. Chang, Surf. Sci. **48**, 9 (1975).
17. P.J. Chen, M.L. Colaianni, and J.T. Yates, Jr., J. Appl. Phys. **72**, 3155 (1992).
18. S.A. Barnett and J.E. Greene, Surf. Sci. **151**, 67 (1985).
19. D. Krüger and H. J. Osten, Thin Solid Films **258**, 137 (1995).
20. E. de Frésart, K. L. Wang, and S. S. Rhee, Appl. Phys. Lett. **53**, 48 (1988).
21. S. Fukatsu, K. Fujita, H. Yaguchi, Y. Shiraki, and R. Ito, Appl. Phys. Lett. **59**, 2103 (1991).

22. A. Rockett, S. A. Barnett, J. E. Greene, J. Knall, and J. E. Sundgren, J. Vac. Sci. Technol. **A3**, 855 (1985).

23. C.P. Parry, R.A. Kubiak, S.M. Newstead, T.E. Whall, and E.H.C. Parker, Mat. Res. Soc. Symp. Proc. **220**, 79 (1991); C.P. Parry, R.A. Kubiak, S.M. Newstead, E.H.C. Parker, and T.E. Whall, Mat. Res. Soc. Symp. Proc. **220**, 103 (1991).

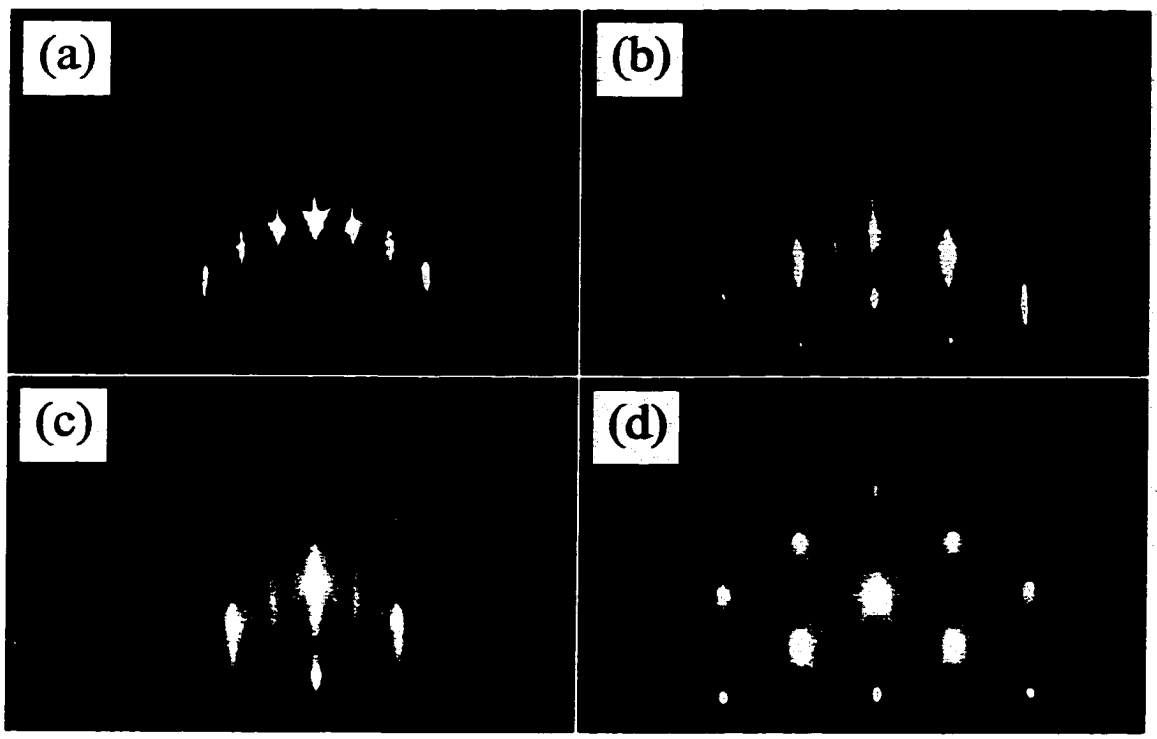

Figure 4.1. RHEED patterns from GS-MBE Si(001):B films grown using Si_2H_6/B_2H_6 mixtures. Film growth temperatures T_s and B concentrations C_B are: (a) $T_s = 550$ °C, $C_B = 8.5 \times 10^{18}$ cm^{-3}, (b) $T_s = 550$ °C, $C_B = 2 \times 10^{21}$ cm^{-3}, (c) $T_s = 800$ °C, $C_B = 3.5 \times 10^{20}$ cm^{-3}, and (d) $T_s = 800$ °C, $C_B = 3 \times 10^{21}$ cm^{-3}.

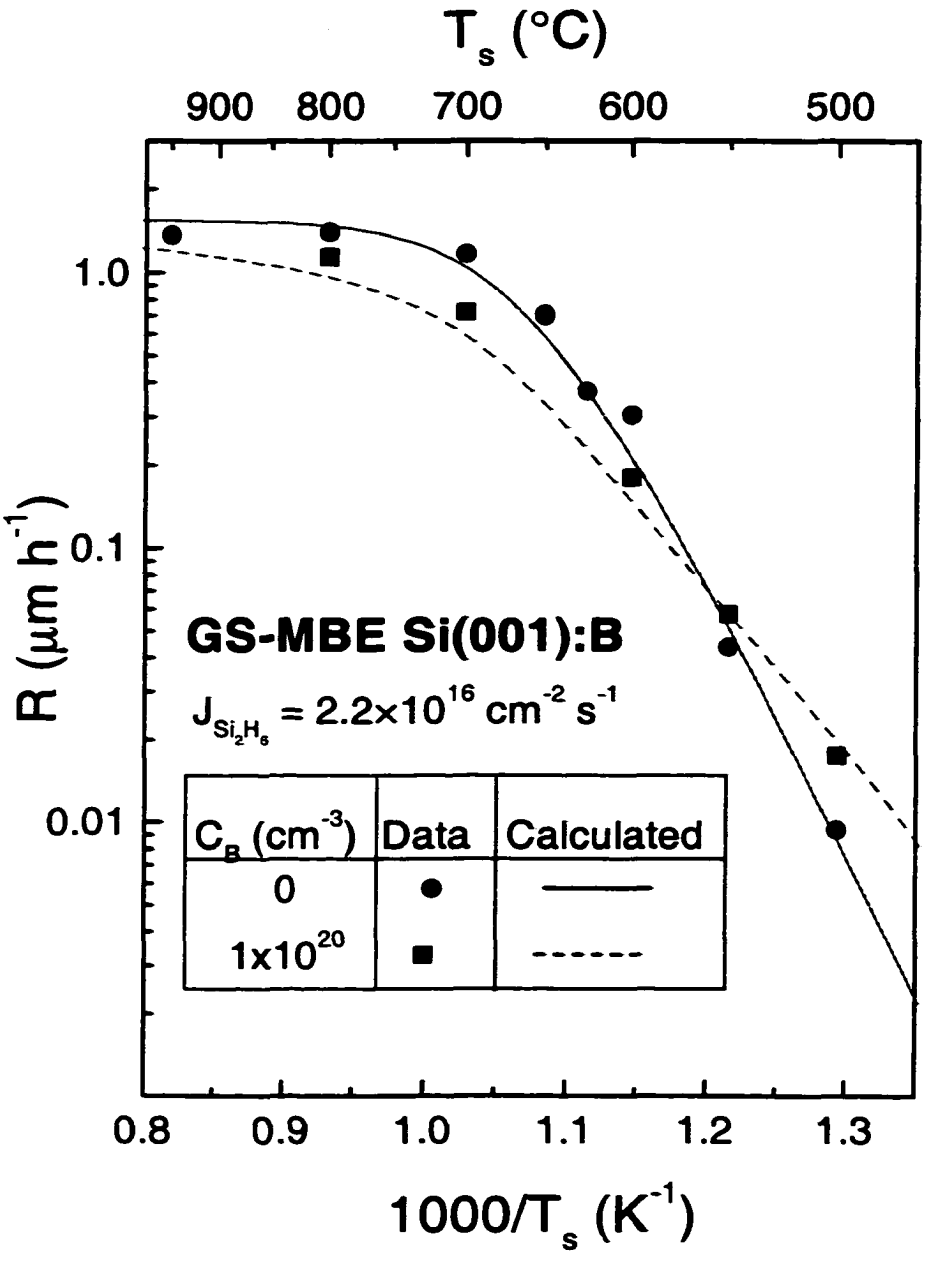

Figure 4.2. Experimental (data points) and calculated (solid line, see section 4) deposition rates R as a function of inverse temperature $1/T_s$ for GS-MBE Si(001) layers grown from Si_2H_6 and GS-MBE Si(001):B layers with $C_B = 1\times10^{20}$ cm^{-3} grown from Si_2H_6/B_2H_6 mixtures.

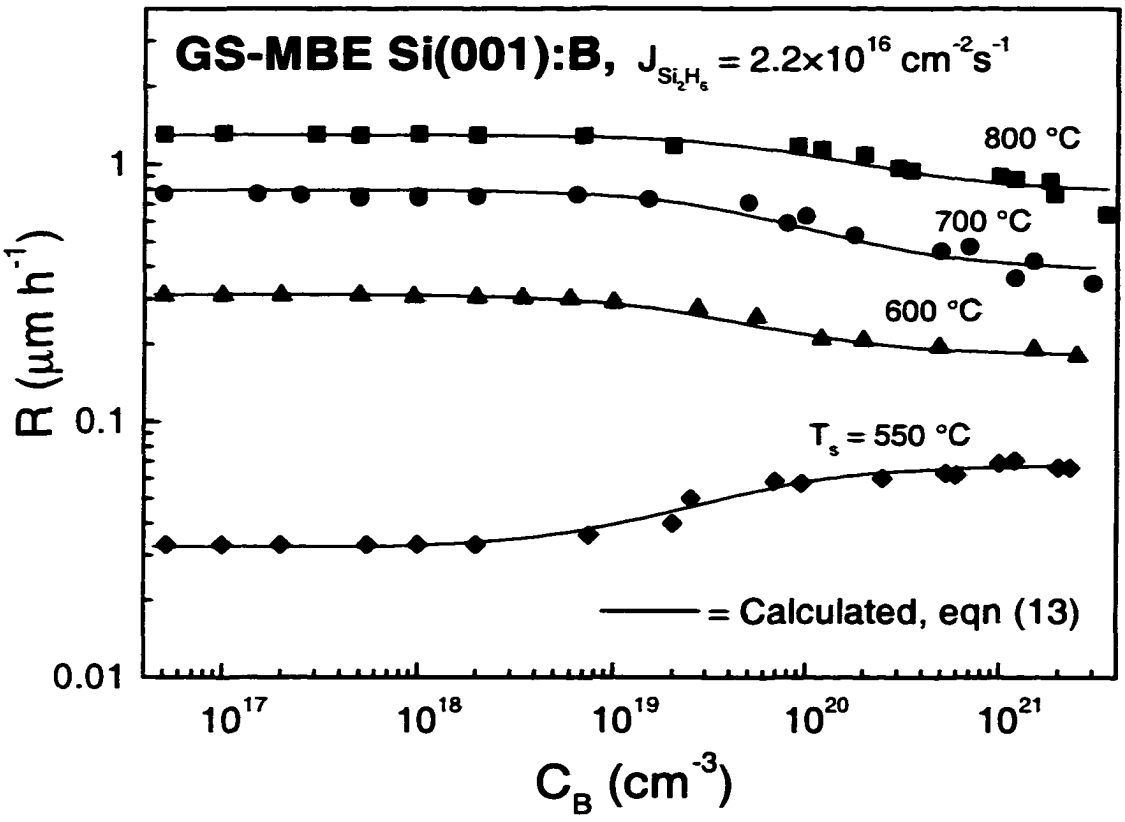

Figure 4.3. Experimental (data points) and calculated (solid lines, see section 4) GS-MBE Si(001):B deposition rates R as a function of the bulk B concentration C_B in layers grown from Si_2H_6/B_2H_6 mixtures with $J_{Si_2H_6} = 2.2\times10^{16}$ cm^{-2} s^{-1}.

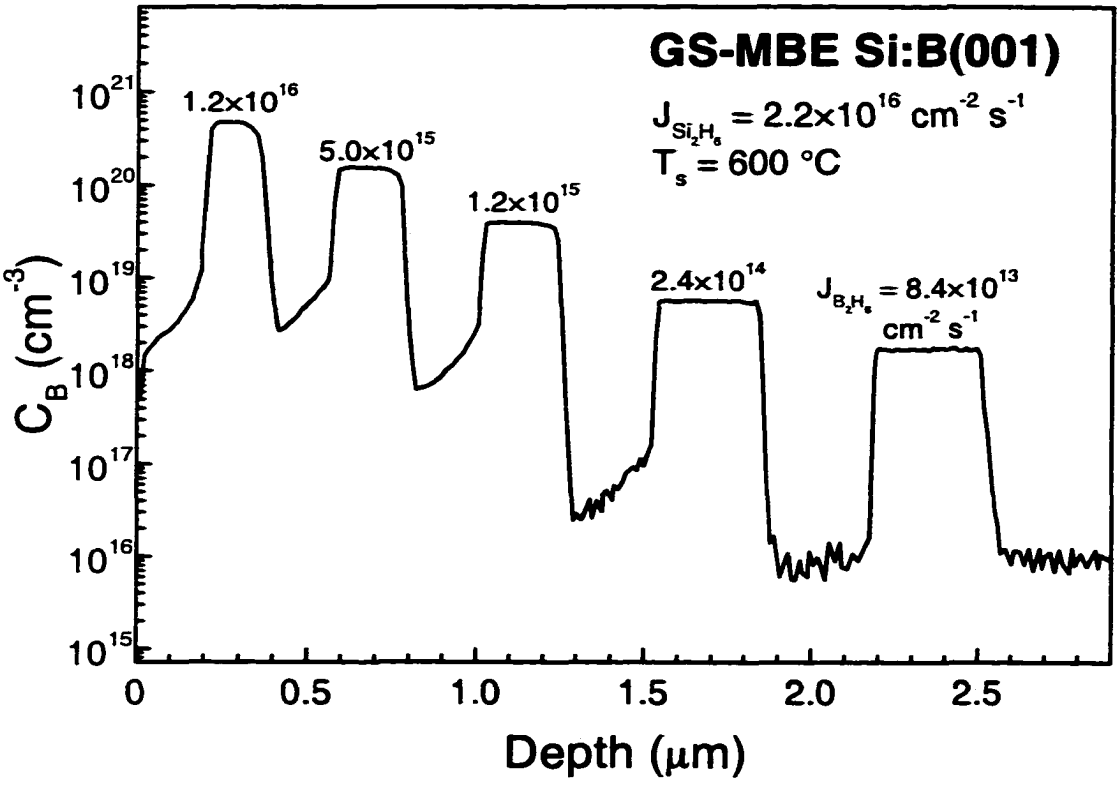

Figure 4.4. SIMS depth profiles through a B modulation-doped Si(001):B film grown by GS-MBE from Si_2H_6 and B_2H_6 at $T_s = 600$ °C. The incident Si_2H_6 flux was $J_{Si_2H_6} = 2.2\times10^{16}$ cm^{-2} s^{-1} while the B flux $J_{B_2H_6}$ was varied from 8.4×10^{13} to 1.2×10^{16} cm^{-2} s^{-1}. The deposition time for each layer was constant at 1 h.

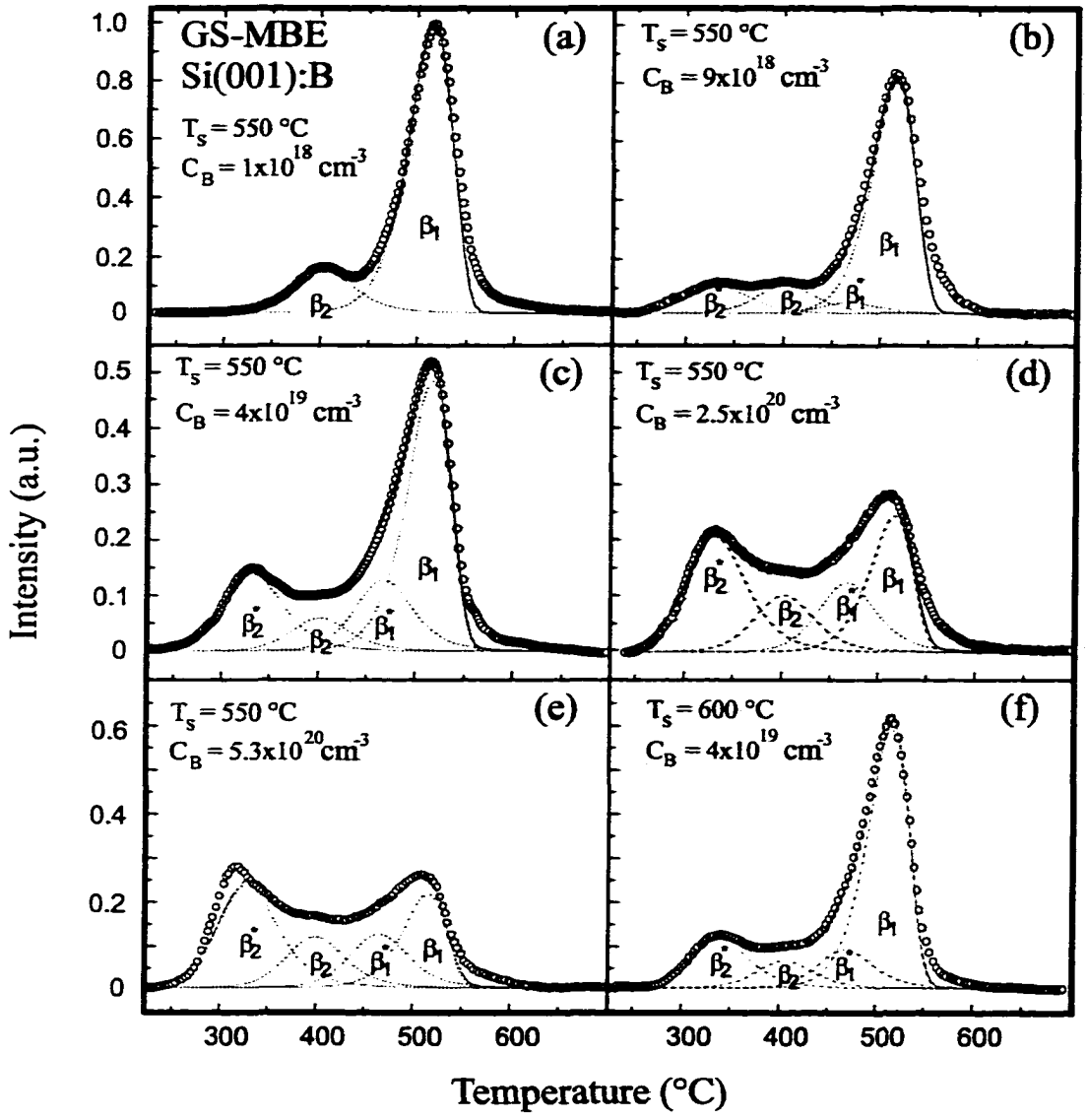

Figure 4.5. D_2 TPD spectra from GS-MBE Si(001) films grown at T_s = 550 °C and 600 °C and doped with different B concentrations C_B. The same intensity scale is used in (a)-(f).

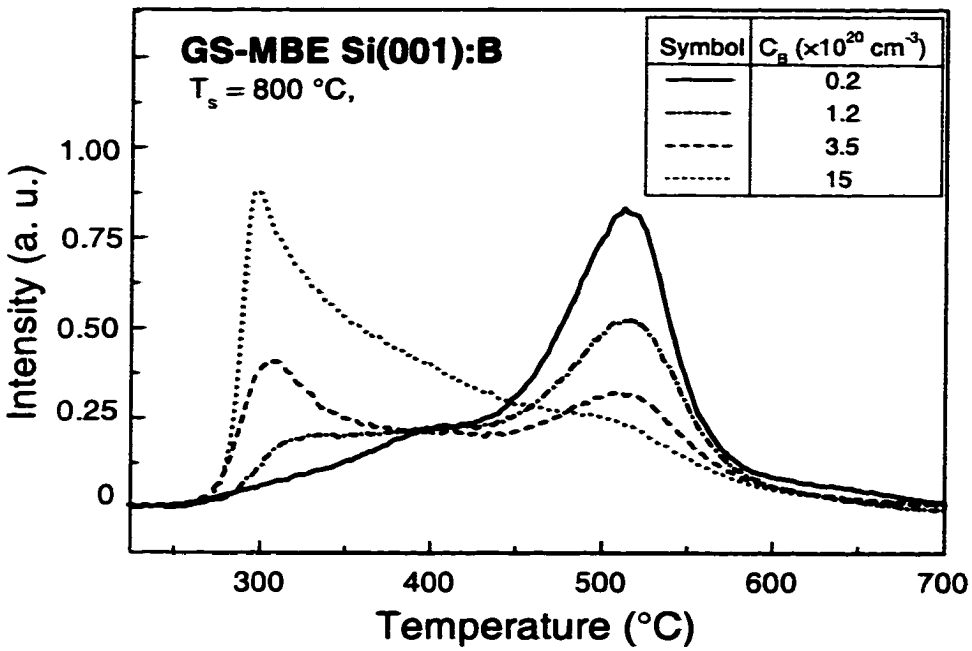

Figure 4.6. D_2 TPD spectra from GS-MBE Si(001) films grown at T_s =800 °C and doped with different B concentrations C_B. The intensity scale is the same as that used in Figure 4.5.

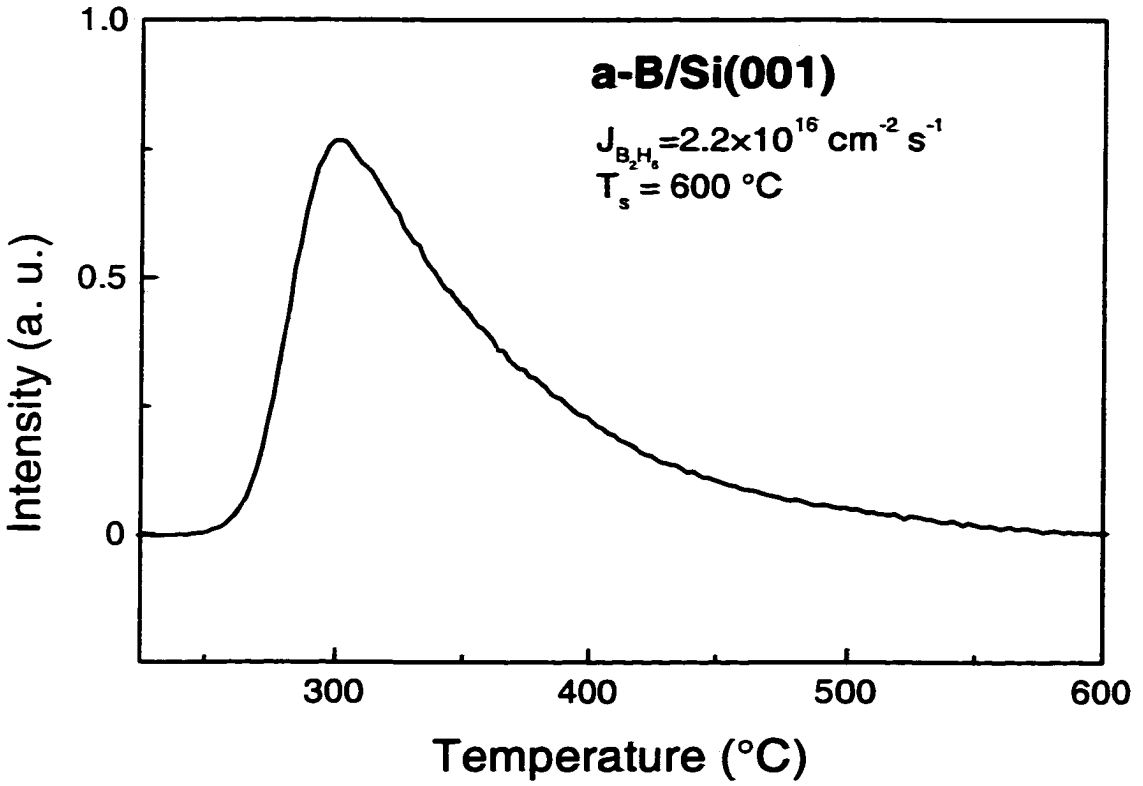

Figure 4.7. D_2 TPD from an amorphous B layer deposited from B_2H_6 on Si(001) at T_s = 600 °C. The intensity scale is the same as that used in Figures 4.5 and 4.6.

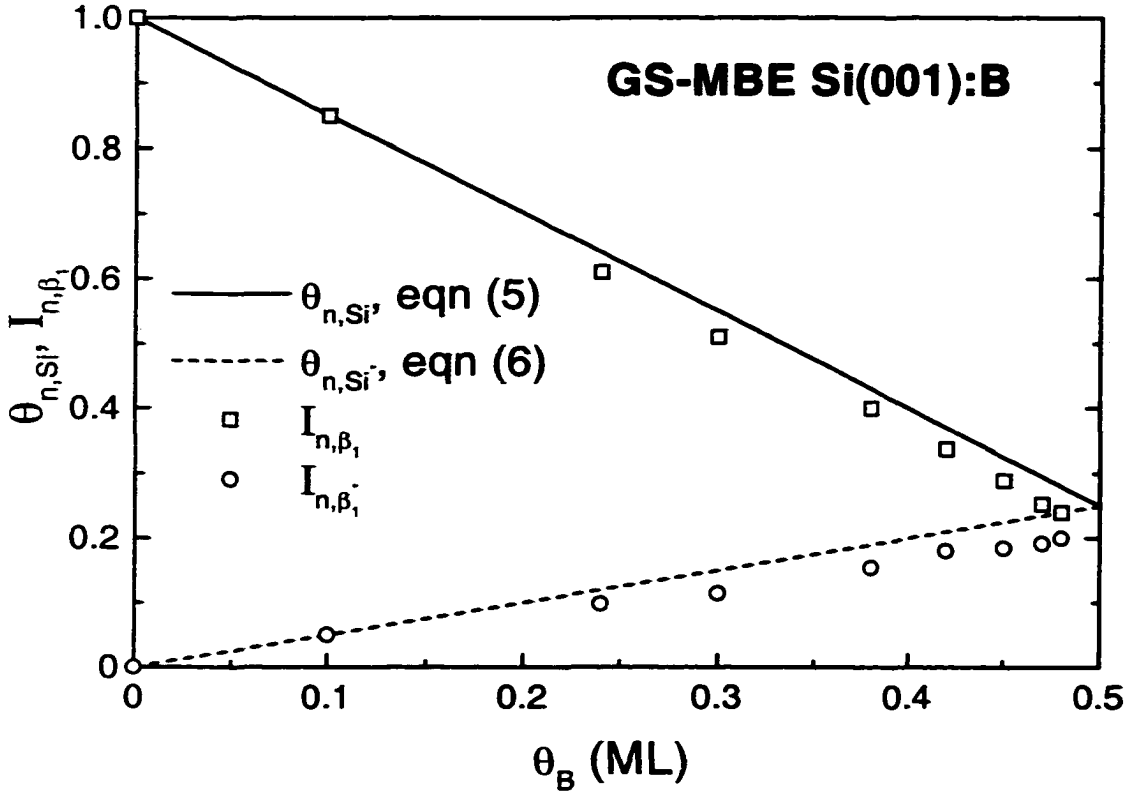

Figure 4.8. Calculated normalized Si and Si^* dimer atom coverages $\theta_{n,Si}$ and θ_{n,Si^*} and measured normalized β_1 and β_1^* D_2 TPD peak intensities I_{n,β_1} and I_{n,β_1^*} as a function of steady-state B surface coverages θ_B on GS-MBE Si(001):B layers grown at T_s = 550 °C.

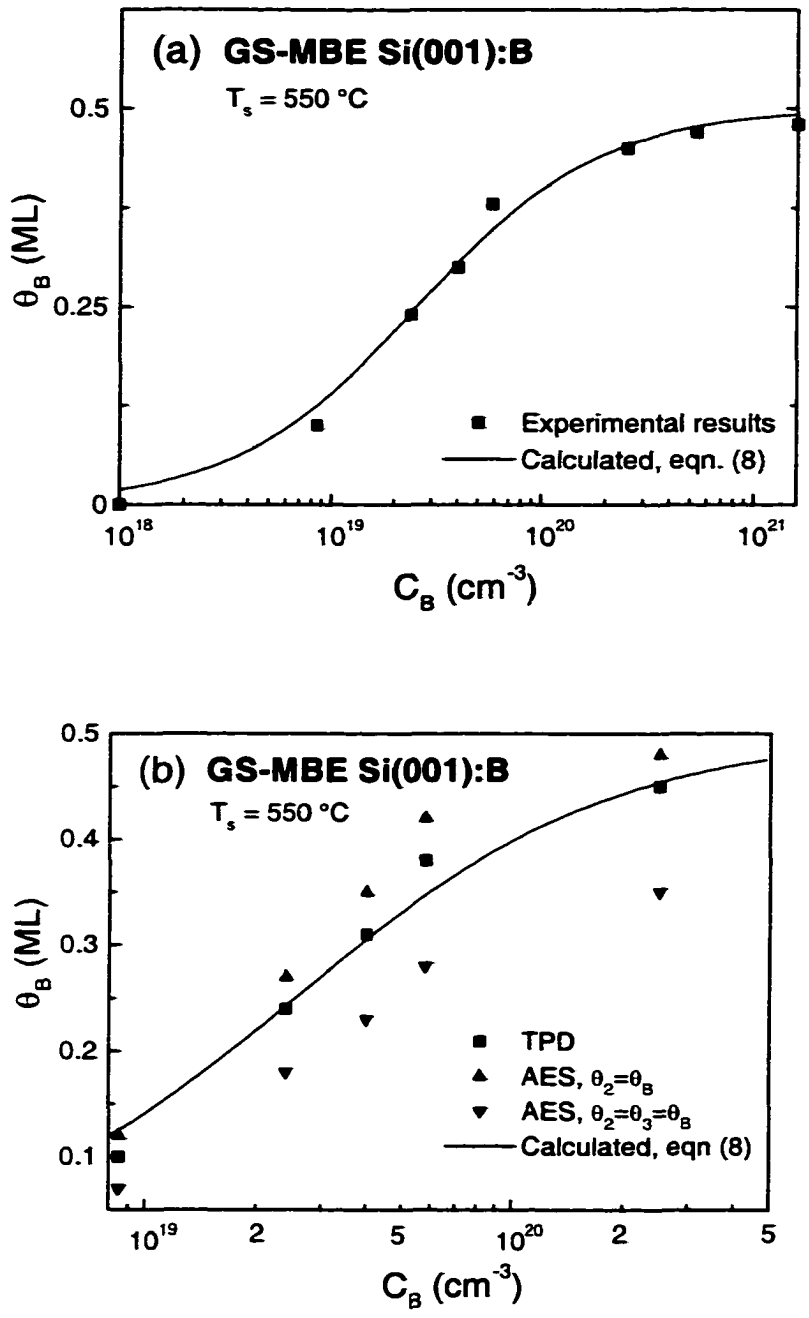

Figure 4.9. (a) B surface coverages θ_B as a function of bulk B concentrations C_B in GS-MBE Si(001):B films grown from Si_2H_6/B_2H_6 mixtures at T_s = 550 °C. (b) θ_B vs C_B data obtained from D_2 TPD measurements (replotted from Figure 9a) compared with data obtained by AES assuming (i) all of the excess segregated B is in layer 2 and (ii) the segregated B is distributed equally in layers 2 and 3.

CHAPTER 5. Ultra-high B doping during Si(001) gas-source molecular-beam epitaxy: B incorporation, electrical activation, and hole transport

5.1. Introduction

I showed in Chapter 4 that B doping at concentrations $C_B > 10^{19}$ cm^{-3} during Si(001) GS-MBE from B_2H_6/Si_2H_6 mixtures leads to complex and competing kinetic effects giving rise to an increase in film growth rates R_{Si} by $\gtrsim$ 50% with increasing $C_B \gtrsim 1x10^{19}$ cm^{-3} at film growth temperatures $T_s \leq 550$ °C and a decrease by corresponding amounts at $T_s \geq 600$ °C.[1-3] At low film growth temperatures where steady-state H coverages θ_H are large, R_{Si} increases due to strong B surface segregation (with enthalpy $\Delta H_s = -0.53$ eV)[3] to the second layer. This enhances H desorption rates, primarily through backbond charge transfer from surface Si-H bonds to B-Si backbonds. At high T_s, θ_H is small and the primary effect of high B coverages is to deactivate surface dangling bonds and, hence, to decrease the density of reactive sites. Hydrogen binding energies and dangling bond coverages as a function of C_B, θ_B, and T_s were quantitatively determined by isotopically-tagged D_2 temperature programmed desorption (TPD). The data were then used to model $R_{Si}(C_B,T_s)$ with no fitting parameters. The results are in very good agreement with measured growth rate data.[3]

In this chapter, I present the results of an investigation of ultra-high B dopant incorporation, electrical activation, and hole transport in defect-free (as judged by TEM) Si(001):B GS-MBE. All B is incorporated into substitutional electrically-active sites for $C_B \leq 2.5x10^{20}$ cm^{-3} ($T_s = 600$ °C), corresponding to a saturation B second-layer coverage θ_B of

0.5 ML as described in Chapter 4. At higher C_B, θ_B exceeds 0.5 ML and an additional B incorporation mechanism becomes operative allowing incorporation of B pairs at substitutional Si sites. The latter are not electrically active but have low charge-scattering cross-sections and thus relatively little effect on carrier mobilities.

5.2. Results

5.2.1. Boron incorporation

More than 70 single-layer and multilayer B-doped Si(001) films were grown in order to determine B incorporation probabilities as a function of $J_{B_2H_6}/J_{Si_2H_6}$ and T_s. A typical SIMS profile through a B modulation-doped sample is presented in Fig. 5.1 for a Si(001) multilayer film grown at $T_s = 600$ °C with successive B-doped regions separated by undoped buffer layers. The deposition time for all layers was 60 min with $J_{Si_2H_6}$ maintained constant at $2.2\text{x}10^{16}$ cm^{-2} s^{-1} while $J_{B_2H_6}$ was varied to provide C_B values from $1.7\text{x}10^{18}$ to $4.7\text{x}10^{20}$ cm^{-3}. SIMS results from layers with $C_B \lesssim 2\text{x}10^{18}$ cm^{-3} exhibit no measurable B segregation and yield profiles which are essentially flat with the leading and trailing edges abrupt to within experimental resolution, 80 Å per concentration decade. Significant B segregation is observed, however, in layers deposited under conditions corresponding to higher steady-state B concentrations. With $C_B \gtrsim 2\text{x}10^{18}$ cm^{-3}, the B incorporation probability is initially depressed giving rise to SIMS profiles with "missing" B at the back side as B accumulates at the surface until a steady-state surface-to-bulk B fraction ratio r_B is achieved. The value of r_B depends upon T_s, R_{Si}, and $J_{B_2H_6}$. After turning off the B_2H_6 flux, the excess B at the surface acts as a reservoir, in multilayer samples, to continue doping what was intended to be undoped buffer layers.

A comparison of the widths of the profiles in Fig. 5.1 clearly shows, in agreement with the results in refs. 2 and 3, that the Si deposition rate at 600 °C decreases with increasing C_B at high $J_{B_2H_6}/J_{Si_2H_6}$ ratios. B doping at concentrations greater than $\approx 5x10^{20}$ cm^{-3} induces surface roughness which propagates in multilayer samples, thus introducing error in the SIMS depth resolution. Therefore, layer thicknesses used for growth rate determinations in samples with high C_B values were obtained from single layer films in order to minimize the number of interfaces.

At constant T_s and $J_{Si_2H_6}$, the total incorporated B concentration C_B, as measured by SIMS, increases linearly with the flux ratio $J_{B_2H_6}/J_{Si_2H_6}$ up to ≈ 0.25 ($J_{B_2H_6} = 5.5x10^{15}$ cm^{-2} s^{-1}) as shown in Fig. 5.2 for layers grown at T_s = 550, 600, 700, and 800 °C. At T_s = 600 °C, for example, Fig. 5.2 shows that $J_{B_2H_6}/J_{Si_2H_6} = 0.25$ corresponds to $C_B = 2.5x10^{20}$ cm^{-3}. The solid lines in Fig. 5.2 were calculated using the procedure outlined in section 5.3.2 and agree well with experimental $C_B(J_{B_2H_6}/J_{Si_2H_6}, T_s)$ data throughout the linear B incorporation range at all growth temperatures. However, as $J_{B_2H_6}/J_{Si_2H_6}$ becomes greater than ≈ 0.3, measured B concentrations exceed calculated values by amounts which increase with the flux ratio and are larger at lower temperatures for a given value of $J_{B_2H_6}/J_{Si_2H_6}$. The inset in Fig. 5.2 shows that the ratio of measured to calculated B concentrations, $C_B/C_{B,calc}$, increases with decreasing T_s yielding $C_B/C_{B,calc}$ values as high as 10 with $J_{B_2H_6}/J_{Si_2H_6} = 3$ and T_s = 550 °C.

Figure 5.3 is a plot of C_B as a function of T_s for incident flux ratios $J_{B_2H_6}/J_{Si_2H_6}$ between $9x10^{-5}$ and 3. With $J_{B_2H_6}/J_{Si_2H_6} \leq 0.1$, the slope of $\ln(C_B)$ vs $1/T_s$ remains constant and negative corresponding to a positive activation energy, the signature of a thermally-activated process,[4] for B chemisorption. At higher $J_{B_2H_6}/J_{Si_2H_6}$ ratios, the slope continuously increases and becomes positive with $J_{B_2H_6}/J_{Si_2H_6} > 2$. The change in slope signifies that additional surface reaction paths

leading to B incorporation become active. The trend toward a more positive slope at higher $J_{B_2H_6}/J_{Si_2H_6}$ values indicates that an additional B incorporation pathway at high B concentrations has a negative activation energy and, hence, is precursor mediated.

5.2.2. Hole concentrations

Effective hole concentrations p_e in B-doped Si(001) films grown at $T_s = 600$ °C with total B concentrations $C_B = 1x10^{17}$-$1.2x10^{22}$ cm^{-3} were determined from temperature-dependent (25-300 K) Hall-effect measurements using the following relationship[5]

$$p_e = \frac{\gamma}{qR_H} \tag{5.1}$$

in which q is the elementary charge, R_H is the Hall coefficient, and γ is the Hall scattering factor defined as the ratio of the Hall mobility to the conductivity mobility. An "effective" hole concentration can be used in equation 5.1 since, as shown below, there is a range in B concentrations over which measured p_e values are larger than the corresponding valence-band hole concentrations, primarily due to changes in the density-of-states (DOS) which decrease the bandgap and give rise to higher effective intrinsic carrier concentrations.[6]

A convenient treatment of hole transport assumes a scattering factor of unity, but this has been shown to result in an overestimate of the dopant concentration in p-type Si.[7-10] γ was calculated by Lin et al.,[11] accounting for the non-parabolic and anisotropic nature of the valence band, to be 0.77 while Lu et al.[12] measured γ as 0.75 for Si(001):B with $C_B = 5x10^{16}$-$1.3x10^{18}$ cm^{-3}. I have used $\gamma = 0.75$ and assumed it to be independent of C_B, consistent with the reported weak functional dependence.[11,12]

Typical curves of p_e versus reciprocal temperature are shown in Fig. 5.4 for samples with $C_B = 1.7x10^{17}$-$1.2x10^{22}$ cm^{-3}. All curves shift in a systematic manner with increasing C_B. For clarity, data are plotted from only nine samples in order to illustrate the primary trends. A data set listing p_e values for all samples at 77, 150, and 300 K is given in Table 5.1.

Three distinct carrier regimes are visible in Fig. 5.4: the itinerant-hole semiconductor regime at low C_B, the metallic regime at high C_B, and an intermediate mixed-conductivity mode. Near room-temperature, the curves from the three lowest doped samples in Fig. 5.4 ($C_B = 1.7$, 3.6, and $13x10^{17}$ cm^{-3}) are in the exhaustion region in which all acceptor states are ionized and $p_e \approx N_B$. In the carrier-freeze-out region at temperatures between $\approx$ 175 and 75 K, p_e initially decreases with decreasing temperature with a slope equal to $-E_B/2k$ in which $E_B = 45$ meV[5] is the B acceptor ionization energy in Si. With further sample cooling, p_e reaches a minimum and then increases again due to hopping conduction through impurity states in the gap.[13] For samples with $C_B > 4x10^{17}$ cm^{-3}, the slopes of the p_e vs 1/T curves in the carrier freeze-out regime become progressively shallower with increasing C_B showing that the energy required to excite holes from the acceptor states to the top of the valence band is decreasing. This, as described in more detail below, is primarily due to tailing in the valence band resulting from the increased hole density and the random spatial distribution of acceptors. The impurity states broaden as well, however this effect is negligible compared to valence-band tailing.[14]

Experimental p_e vs T curves for all films with $C_B < 4x10^{17}$ cm^{-3} were analyzed using the charge neutrality equation written for a single acceptor. The analysis accounted for valence-band spin-orbit splitting, included the full Fermi integral, and used an effective-mass valence-band DOS as in ref. 4. Values of the electrically-active B concentration N_B and unintentional

background donor concentrations N_d were determined based upon nonlinear least-squares fits. The calculated curves exhibit very good agreement with the Hall-effect data. N_B values were equal to C_B within experimental uncertainty and N_d for all samples was $< 9x10^{13}$ cm^{-3}. Since all donors, irrespective of their ionization energy or origin (i.e., impurity or defect-related state) contribute to N_d, the maximum concentration of donor-like defects is $\leq 9x10^{13}$ cm^{-3}. Similarly, the maximum concentration of shallow acceptor-like defects must also be $< 9x10^{13}$ cm^{-3}.

The samples in Fig. 5.4 with $C_B = 5.0x10^{18}$ and $6.0x10^{18}$ cm^{-3} have B concentrations near the metal-semiconductor transition. As the measurement temperature is reduced below 300 K, carrier freeze-out results first in about a 20% decrease in p_e before hopping conduction begins to dominate and increase p_e again until saturation is achieved at temperatures $\lesssim$ 60 K. The combination of valence-band tailing (primarily) and broadening of the acceptor band formed by the overlap of acceptor-state wavefunctions eventually leads to overlap of the impurity and valence bands in films with $C_B \gtrsim 2x10^{19}$ cm^{-3}. Thus, these samples do not exhibit carrier freeze-out and are predominantly metallic in nature over the entire measurement temperature range.

In the intermediate conduction regime described above, prior to the onset of band overlap, increasing the acceptor-state hole density p_{acc} (a function of both C_B and T) eventually results in wavefunction overlap becoming sufficiently large that direct tunneling, or hopping, of carriers between states is a significant component of the overall sample conductivity. Mott[13,15,16] developed a straightforward prescription for characterizing the metal-semiconductor transition. The hydrogenic doping model,[5] accounting for the dielectric constant of the host material (Si, in this case) and the carrier effective mass, is used to estimate the Bohr radius and, hence, the volume ($\simeq 1.2x10^5$ $Å^3$) "occupied" by holes bound to acceptors. The Mott transition is then

defined to occur when p_{acc} becomes sufficiently large that bound hole wavefunctions, whose spatial extent are defined by the above volume, just begin to overlap. Using Mott's criterion, acceptor state overlap becomes significant when $p_{acc} \gtrsim 8x10^{18}$ cm^{-3}. This is consistent with our experimental results in Fig. 5.4 where samples with $C_B \geq 5x10^{18}$ cm^{-3} exhibit very little carrier freeze-out. At even higher C_B, the valence band tail advances into the gap sufficiently that it overlaps with the broadened impurity band.

As noted above, the acceptor ionization energy decreases with increasing C_B for films with B concentrations greater than approximately $4x10^{17}$ cm^{-3}. This should result in $p_e(300K) \approx N_B = C_B$, assuming complete electrical activation, within experimental uncertainty. The data in Fig. 5.4 and Table 5.1 show that it is indeed the case for layers with $C_B \lesssim 2x10^{18}$ cm^{-3}. However, for films with higher B concentrations, $p_e(300K)$ values obtained from Hall effect measurements vary significantly from C_B. That is, layers with C_B between $2x10^{18}$ and $5x10^{20}$ cm^{-3} have $p_e(300K)$ values which are actually larger than C_B by up to a factor of four. Each B atom can only contribute a maximum of one hole to the valence band. The excess increase in carrier concentration results from increased thermal carrier generation due to bandgap narrowing and associated changes in the DOS when C_B exceeds $2x10^{18}$ cm^{-3}.[17]

Bandgap narrowing has been attributed to three primary causes:[14] fluctuations in the local lattice potential due to the random distribution of acceptors, electron-hole correlation, and hole-hole exchange effects. The first effect results in the largest contribution to bandgap narrowing and gives rise to band tailing with the introduction of new states in the gap while the latter two effects, listed in order of decreasing importance, produce rigid shifts in the band edges. As the DOS in the impurity band increases, the band also broadens. However, this contribution is

small compared to band-edge tailing and can generally be ignored.[14] A quantum mechanical description of band-edge tailing due to spatially dependent distortions in the local DOS developed by Lax and Phillips[18] and Frisch and Lloyd[19] was used by Klauder[20] to derive an efficient computational algorithm to describe bandgap narrowing as a function of dopant concentration.

The electron-hole correlation energy arises from Coulomb screening of both the stationary acceptor ions and the minority carrier electrons while the hole-hole exchange energy results from the Pauli exclusion principle which states that no two particles can have the same set of quantum numbers. The exclusion principle gives rise, in addition to an electrostatic repulsive energy, to repulsion between two holes of like spin. However, since the hole population has a random distribution of spin states, the overall repulsive energy decreases which is equivalent to an attractive exchange energy. Electron-hole correlation effects shift the conduction-band edge down, while the hole-hole correlation effects decrease the acceptor level ionization energy. A theory describing changes in the bandgap energy due to hole-hole interactions and electron-hole correlations was originally derived by Mahan[21] and later confirmed by Sterne and Inkson.[22]

Bennett[17] developed a formalism based upon the work of Klauder[20] and Mahan[21] to quantitatively account for each of the above effects in determining the net shift in the valence and conduction band edges as well as the perturbed DOS and hence the effective intrinsic carrier concentrations, $n_{ie} \equiv p_{ie}$, as a function of doping density for both n- and p-type Si. Bennett's treatment was applied to our experimental results in order to obtain the actual hole concentration p, and hence N_B, from the measured data. Calculated p_{ie} values, normalized to the non-degenerate intrinsic carrier concentration p_i, initially increase with C_B, due to bandgap narrowing, then

decrease from a peak value of 4 at $C_B = 7x10^{19}$ cm^{-3} with increasing C_B as the valence-band tail begins to overlap with the B impurity band. When C_B exceeds $5x10^{20}$ cm^{-3}, essentially all transport is metallic and the measured carrier concentration is again equal to the ionized acceptor concentration. A calculated curve for p_{ie}/p_i, based upon Bennett's formalism, is plotted vs C_B in Fig. 5.5. The calculation was carried out between $8x10^{18}$ and $5x10^{20}$ cm^{-3}, due to the simplifications used in the model,[17] and the results extrapolated to $2x10^{18}$ cm^{-3}.

A comparison of our C_B values, determined by SIMS, with p_e, determined by Hall-effect measurements, show that $p_e > C_B$ over the B concentration between $5x10^{18}$ and $\approx 5x10^{20}$ cm^{-3} (see Table 5.1). The ratio p_e/C_B is plotted vs C_B in Fig. 5.5 and shown to agree very well with Bennett's model.[17] I only plot data for $C_B \leq 2.5x10^{20}$ cm^{-3} for which, as established below, and in section 5.2.5, that all B atoms are electrically active. Thus, although the effective carrier concentration is greater than C_B, the electrically-active acceptor density N_B remains equal to the B atom density C_B.

Figure 5.6 is a plot of N_B vs C_B over the entire B doping concentration range, spanning more than four decades, $C_B = 1x10^{17}$-$1.2x10^{22}$ cm^{-3}. The results show that B is incorporated into substitutional electrically-active sites at concentrations up to $2.5x10^{20}$ cm^{-3}. For samples with higher B concentrations, N_B is increasingly less than C_B as larger fractions of B are incorporated into electrically-inactive sites. Nevertheless, N_B still continues to increase even up to the highest doped sample with $C_B = 1.2x10^{22}$ cm^{-3} for which $N_B = 1.3x10^{21}$ cm^{-3}.

5.2.3. Resistivity

Figure 5.7 is a plot of room-temperature resistivity ρ as a function of C_B for GS-MBE Si(001):B. The results are equal to, or lower than, the best bulk Si:B data.[23] ρ decreases with increasing C_B to reach its lowest value ρ_{min} = 300 $\mu\Omega$-cm at $C_B = 2.5x10^{20}$ cm^{-3}, remains approximately constant over a wide range in C_B, and then slowly increases again. As demonstrated in the above section, $C_B = 2.5x10^{20}$ cm^{-3} is the maximum B concentration at which 100% of the dopant atoms are electrically active.

The resistivity is inversely related to the carrier concentration and the mobility through the relation $\rho = (qp\mu)^{-1}$. The initial rapid decrease in $\rho(C_B)$ for $C_B \leq 2.5x10^{20}$ cm^{-3} is controlled primarily by the carrier concentration since, as shown below, the room-temperature carrier mobility changes relatively gradually with C_B in this concentration range. However, as C_B is raised above $2.5x10^{20}$ cm^{-3}, an increasing fraction of the incorporated B is electrically inactive. Thus, p increases much more slowly while μ continues to decrease with the net effect that $\rho(C_B)$ remains relatively constant over the C_B range between $2.5x10^{20}$ and $\simeq 2x10^{21}$ cm^{-3}. This has the practical benefit that it provides a wide process window for fabrication of ultra-low resistivity Si layers for use in high-power and/or current switching applications, local chip-level metallization, and active layers in bipolar and MOS transistors. Eventually, as $C_B > 2x10^{21}$ cm^{-3}, ρ increases as the local strain fields surrounding B atoms in the Si matrix begin to overlap and the atomic planes become sufficiently distorted to disrupt long-range order and give rise to incoherent carrier scattering.

Representative temperature-dependent resistivity data are shown in Fig. 5.8. The curve shapes continuously shift from those characteristic of semiconducting itinerant-hole valence-

band conductivity at low B concentrations to metallic conductivity at high C_B values. The initial decrease in the resistivity of layers with C_B = 1.7, 3.6, and $13x10^{17}$ cm^{-3} as a function of decreasing temperature is caused by a reduction in phonon scattering. However, ρ increases again at temperatures below ≈ 175 K due primarily to a decrease in the hole concentration resulting from carrier freeze-out. ρ(T) curves for layers with $C_B = 5$ and $6x10^{18}$ cm^{-3}, corresponding to the intermediate conduction regime, display a mixed-mode semiconducting plus hopping behavior. They are semiconductor-like in their temperature dependence near 300 K and metallic-like (i.e., no significant T-dependence) at low temperatures. Layers with $C_B \gtrsim 4x10^{19}$ cm^{-3} are predominantly metallic.

As C_B approaches the metal-semiconductor transition, the low-temperature resistivity limit ρ_o changes very rapidly. Fig. 5.8 shows, for example, that ρ_o decreases by more than two orders of magnitude as C_B increases from $1.3x10^{18}$ to $5x10^{18}$ cm^{-3}. As discussed in the previous section, when the B concentration becomes high enough that the acceptor states begin to merge into an impurity band, the local DOS, and hence the sample conductivity, increases rapidly. The rapid rate of decrease in ρ_o with C_B is due to the fact that the state-to-state tunneling probability increases exponentially with decreasing tunneling distance. In the fully metallic regime, Fig. 5.8 shows, in agreement with Fig. 5.7, that as C_B becomes larger than $2.5x10^{20}$ cm^{-3}, ρ increases with increasing C_B.

5.2.4. Hole mobilities

Room-temperature hole conductivity mobilities μ, derived from measured Hall mobilities using the relationship $\mu = \mu_H/\gamma$ with a Hall scattering factor $\gamma = 0.75$, are plotted in Fig. 5.9 as a

function of B concentration. The conductivity mobility was used in order to directly compare the results with literature values for bulk Si:B. Fig. 5.9 shows that the present mobilities are equal to, or greater, than the best bulk data[23,24] and are in good agreement with an empirical relationship (solid line) developed by Caughy and Thomas[25] and refined by Thurber et al.[26] μ ranges from 190 $cm^2\ V^{-1}\ s^{-1}$ with $C_B = 1.8x10^{17}\ cm^{-3}$ to 47 $cm^2\ V^{-1}\ s^{-1}$ with $C_B = 2.5x10^{20}\ cm^{-3}$, the limit of complete dopant electrical activity.

As B concentrations are increased above $2.5x10^{20}\ cm^{-3}$, corresponding to decreasing activated dopant fractions, μ remains approximately constant with C_B up to $1.6x10^{21}\ cm^{-3}$ ($\mu = 41\ cm^2\ V^{-1}\ s^{-1}$) for which the concentration of electrically inactive dopant atoms is $1.1x10^{21}\ cm^{-3}$. This indicates, as discussed further in section 5.3.3, that the scattering cross-section of inactive B is small. At even higher B concentrations, however, the hole mobility decreases rapidly ($\mu = 8\ cm^2\ V^{-1}\ s^{-1}$ with $C_B = 1.2x10^{22}\ cm^{-3}$).

Typical results for μ vs T are plotted in Fig. 5.10 for representative layers with B concentrations ranging from $1.7x10^{17}$ to $4.2x10^{21}\ cm^{-3}$. μ(T) data for the complete set of samples are listed in Table 5.1. The curves in Fig. 5.10 for the three lowest doped layers, C_B = 1.7, 3.6, and $13x10^{17}\ cm^{-3}$, are in very good agreement with published curves for bulk p-type Si.[8,10] μ(T) initially increases with decreasing temperature following a negative power law dependence. Over this temperature range, the mobility is primarily limited by phonon, ionized-impurity, and hole-hole scattering.[4] The power law exponent decreases with increasing carrier concentration due to increasing contributions from ionized-impurity and hole-hole scattering. As T is decreased below 100-150 K, the negative slope of the μ vs T curves decreases and eventually changes sign as hole

carriers continue to freeze out and neutral impurity scattering dominates. Hole mobilities at 77 K vary from 980 $cm^2 V^{-1} s^{-1}$ with $C_B = 1.7x10^{17}$ cm^{-3} to 250 $cm^2 V^{-1} s^{-1}$ with $C_B = 1.3x10^{18}$ cm^{-3}.

At temperatures above 100 K, the two samples in Fig. 5.10 with B concentrations $C_B = 5x10^{18}$ and $6x10^{18}$ cm^{-3}, near the metal-semiconductor transition, exhibit $\mu(T)$ behavior which is qualitatively similar to that of the lower doped samples. However, in this B concentration range, ionized-impurity scattering becomes more important and the transition from scattering dominated by phonons to impurity-dominated scattering shifts to higher temperatures. With further reduction in T, carrier mobilities decrease and then saturate below ≈ 50 K as impurity-band hopping conduction, which is only weakly temperature dependent, increasingly controls carrier transport.

Samples with C_B above $4x10^{19}$ cm^{-3} appear completely metallic. Since the Fermi level is now well within the valence band, carrier freeze-out is no longer observed and impurity scattering dominates at all temperatures. Thus, carrier mobilities for these layers exhibit little temperature dependence. 77 K hole mobilities in this dopant concentration range vary from 62 $cm^2 V^{-1} s^{-1}$ with $C_B = 4x10^{19}$ cm^{-3} to 8 $cm^2 V^{-1} s^{-1}$ with $C_B = 1.2x10^{22}$ cm^{-3}.

5.2.5. Film microstructure and strain

A combination of HR-XRD, reciprocal-lattice mapping, TEM, and XTEM was employed to examine the microstructure, crystalline quality, and strain-state of GS-MBE Si(001):B layers as a function of C_B. High-resolution reciprocal-lattice mapping is more sensitive than TEM to the initial stages of film relaxation through misfit dislocation generation. The resolution for detecting changes in film/substrate lattice-constant misfit in the present high-resolution mapping

measurements is $\approx 2x10^{-5}$ corresponding to an average dislocation separation of 10 μm. In contrast, direct observation by TEM is limited to dislocation densities $\gtrsim 5x10^{3}$ cm^{-1} or changes in residual in-plane stress $\gtrsim 10^{-4}$. All films, even those with the highest B concentrations, $C_B = 1.2x10^{22}$ cm^{-3}, were found to be completely coherent with the substrate.

Figure 5.11a shows a typical overview 004 ω-2θ scan, obtained with an open detector, of the Si substrate and Si:B layer. The film is 6500 Å thick with $C_B = 2.5x10^{20}$ cm^{-3} and was grown at 600 °C. Finite-thickness fringes, which arise due to interference of diffracted waves scattered from a finite number of lattice planes, are observed in the region between the substrate and layer diffraction peaks. The fringes are a measure of the high structural quality of the alloy layer and indicate that lattice planes and interfaces are uniform and flat.[27]

A simulated 004 HR-XRD ω-2θ rocking curve, calculated based upon the fully dynamical formalism developed by Taupin[28] and Takagi,[29] is shown in Fig. 5.11b for comparison. The simulation was carried out assuming a perfectly planar and coherent film/substrate interface and interpolated elastic constants. B surface segregates with an enthalpy of -0.53 eV during Si(001):B film growth by GS-MBE from B_2H_6/Si_2H_6.[3] This results in the formation of a B-depleted region between the film/substrate interface and the film thickness at which a steady-state dopant incorporation rate is achieved.[30] The B depletion zone slightly increases the scattered intensity in the ω-2θ region between the layer and substrate peaks. This is accounted for in the XRD simulation by using a linearly-graded B-depleted layer which is, based upon SIMS depth profile results, 300 Å thick. The measured and simulated curves in Fig. 5.11 are in excellent agreement with respect to the positions and intensities of both the Bragg peaks and the finite-thickness

interference-fringes. From the fitted curve, assuming Vegard's rule, a dopant concentration of $C_B = 2.8x10^{20}$ cm^{-3} is obtained, which agrees well with the SIMS value of $2.5x10^{20}$ cm^{-3}.

Figure 5.11c is a HR-XRD ω-2θ scan from a 6500-Å-thick Si:B layer grown at $T_s = 600$ °C with $C_B = 4.2x10^{21}$ cm^{-3}. The relative peak position and the full-width at half maximum intensity $\Gamma_{\omega-2\theta}$ have increased from 235 and 25 arc-s to 674 and 69 arc-s, respectively, while the finite-thickness fringes have almost disappeared due to surface roughening.

Figure 5.12 shows typical high-resolution reciprocal lattice maps around the asymmetric 115 Bragg reflection from Si:B films with $C_B = 2.5x10^{20}$ and $4.2x10^{21}$ cm^{-3}. Diffracted intensity distributions are plotted as isointensity contours as a function of the reciprocal lattice wavevectors $k_{\|}$ parallel and $k_{\perp}$ perpendicular to the surface. For all samples, including the two ultra-highly doped films shown here, the substrate and film scattering distributions are nearly perfectly aligned in the $k_{\|}$ direction indicating negligible in-plane strain relaxation. From high precision measurements, the degree of strain relaxation is $< 1x10^{-4}$, near the instrument detection limit $2x10^{-5}$, for all samples. Thus, the in-plane Si(001):B lattice constants $a_{\|} = 5.4310 \pm 0.0002$ Å are equal to that of bulk Si. The vertical separation between the film and substrate diffracted intensity distributions increases with C_B indicating a tetragonal distortion. For the two layers corresponding to the data in Fig. 5.12, $a_{\perp} = 5.4180$ Å for the film with $C_B = 2.5x10^{20}$ cm^{-3} and 5.4055 Å with $C_B = 4x10^{21}$ cm^{-3}.

Full width at half-maximum intensity values of the scattering intensity distributions along the ω, ω-2θ, and in-plane $\|$ directions from the Si:B film in Fig. 5.12a ($C_B = 2.5x10^{20}$ cm^{-3}) are $\Gamma_{\omega} = 12$ arc-s, $\Gamma_{\omega-2\theta} = 38$ arc-s, and $\Gamma_{\|} = 10$ arc-s. The square root of the sum of these parameters Γ_t provides the best metric for comparing peak widths independently of peak shape.[31,32] For this

layer, Γ_t = 41 arc-s which is near the minimum theoretical value for this alloy, 21 arc-s, calculated based upon the intrinsic peak width, 6 arc-s, while accounting for strain-broadening due to lattice constant mismatch and finite thickness effects.[32] Peak-width values for the substrate diffracted intensity distribution in Fig. 5.12a are: Γ_ω = 13 arc-s, $\Gamma_{\omega\text{-}2\theta}$ = 22 arc-s, $\Gamma_\parallel$ = 11 arc-s, with Γ_t = 28 arc-s. The similarity in film and substrate Γ_ω values indicates negligible film mosaicity.

Increasing C_B to $4.2\text{x}10^{21}$ cm^{-3} (Fig. 5.12b) causes the peak separation to increase in the $k_\perp$ direction while the film remains coherent with the substrate. For this layer, Γ_t = 102.5 arc-s (Γ_ω = 8.3, $\Gamma_{\omega\text{-}2\theta}$ = 102, and $\Gamma_\parallel$ = 6.1 arc-s) while Γ_t for the substrate is 22.6 arc-s (Γ_ω = 10, $\Gamma_{\omega\text{-}2\theta}$ = 18.7, and $\Gamma_\parallel$ = 8 arc-s). $\Gamma_{\omega\text{-}2\theta}$ for the film peak is now an order of magnitude larger than the corresponding substrate value. However, Γ_ω and $\Gamma_\parallel$ remain near their minimum theoretical values, indicating lack of significant mosaicity. Furthermore, the integrated 115 Bragg intensity I_{115} from the layer peak is weak and the diffuse scattering intensity at angles away from the Bragg peak is high. Thus, I interpret the large Γ_t value from the layer as signifying the presence of large variations in the local microstrain[31] which, at these high B concentrations, causes severe lattice-plane buckling distortions which reduce the 115 peak intensity.

Since all Si:B films are fully coherent with their substrate, $a_\perp$ — plotted in Fig. 5.13 as a function of C_B for layers grown at T_s = 550, 600, and 800 °C — is a direct measure of the tetragonal strain associated with B dopant incorporation. The curves show an initial linear "Vegard's rule" decrease in $a_\perp$ with increasing B concentration, but deviate significantly from linearity when C_B exceeds a critical value C_B^*, which is $\approx 2\text{x}10^{20}$ cm^{-3} at T_s = 550 °C and $2.5\text{x}10^{20}$ cm^{-3} at 600 °C. The latter is consistent with transport measurements (Figs. 5.7 and 5.9)

and N_B vs C_B results (Fig. 5.6) presented in section 5.2.2 showing that for 600 °C films with $C_B > 2.5x10^{20}$ cm^{-3}, an increasing fraction of the incorporated B resides in electrically-inactive sites. A detailed analysis, including an analytical model describing the $a_\perp(C_B)$ data in Fig. 5.13, is presented in section 5.3.1. Note, however, that the behavior of the T_s = 800 °C films is clearly quite different, with C_B^* reduced to $5x10^{19}$ cm^{-3}.

Five ultra-highly doped GS-MBE Si(001):B layers grown at T_s = 600 °C with fully electrically-active B concentrations $C_B = 2.5x10^{20}$ cm^{-3}, well above the reported[33] equilibrium solid-solubility limits, were annealed in UHV at 600-1100 °C for times ranging up to 12 h. HR-XRD, reciprocal-lattice mapping, and Hall-effect analyses of the annealed layers showed that they remained fully coherent and all incorporated B still resides in substitutional sites. This suggests that the reaction path leading to B incorporation in electrically-inactive sites proceeds through surface rather than bulk sites and that, once incorporated, the inactive species are frozen in the lattice at $T_s \leq 600$ °C.

Plan-view 001 bright-field TEM micrographs of GS-MBE Si(001):B layers grown at T_s = 550 and 600 °C with $C_B < 1x10^{20}$ cm^{-3} are completely featureless. An example is presented in Fig. 5.14a for a film with $C_B = 1x10^{20}$ cm^{-3}. The selected-area electron diffraction pattern shown in the inset was obtained near the [001] zone axis and consists only of single-crystal reflections with symmetric intensities. $\bar{1}10$ XTEM images also show that the films are highly perfect (see, for example, Fig. 5.14b) with 111 lattice fringes which are continuous across the film/substrate interface.

Similarly, TEM and XTEM analyses of films with even higher B concentrations, up to the highest value grown ($C_B = 1.2x10^{22}$ cm^{-3}) were found, in agreement with HR-XRD results, to be

free of misfit dislocations and B precipitates. The latter result indicates that B clusters, if present, must be smaller than ≈ 50 Å. However, films with $C_B \geq 2.5x10^{20}$ cm^{-3}, in contrast to lower-doped layers, exhibit mottled dark contrast similar to that reported for ultra-highly B doped Si ($C_B = 3.5x10^{20}$ cm^{-3}) grown by solid-source MBE.[34] Figure 5.15 is a typical XTEM dark-field image, acquired using a $\bar{g}$ = 004 diffraction vector, of a GS-MBE Si:B film grown at $T_s = 600$ °C with $C_B = 3x10^{21}$ cm^{-3}. The image is representative of the entire sample, based upon over 100 fields of view. The film, even though it contains contrast variations throughout, appears everywhere darker than the substrate. The contrast arises from the enormous covalent radius misfit, -32%, between B and Si giving rise to large local atomic displacements of matrix atoms surrounding the B atoms in randomly distributed Si lattice sites. This, in turn, causes destructive interference among diffracted electron beams and results in reduced image brightness, particularly in dark-field imaging conditions.

While all layers grown at $T_s \leq 600$ °C exhibit smooth surfaces as in Fig. 5.15, both RHEED and XTEM analyses reveal extensive surface roughening in layers with $C_B > 5x10^{19}$ cm^{-3} grown at $T_s \geq 700$ °C. Pyramidal surface structures bounded by smooth 113 facets develop with increasing layer thickness. Figure 5.16a is a typical RHEED pattern obtained along a [110] direction of a 6000-Å-thick Si(001):B layer grown at 800 °C with $C_B = 3x10^{20}$ cm^{-3}. Streaks, inclined at angles of 25.2° with respect to the surface normal and signifying the presence of 113 facets, are visible emanating from the tops and bottoms of both fundamental and half-order diffraction rods. At still higher B concentrations, $C_B > 10^{21}$ cm^{-3} (Fig. 5.16b), three-dimensional transmission diffraction patterns, indicative of an extremely rough surface, were observed at $T_s \geq 700$ °C.

An XTEM 110 dark-field image, acquired using a diffraction vector $\bar{g}$ = 004, from a 9000-Å-thick layer grown at 800 °C with $C_B = 3x10^{21}$ cm^{-3} is shown in Fig. 5.16c. The surface undulations have a wavelength of ≈ 1800 Å, with an average height of 400 Å. The slope of the facet surfaces is ≈ 25°, consistent with their being 113. XTEM micrographs show that layers exhibiting significant surface roughening also contain a large number density of dislocation loops and 111 stacking faults. These are clearly evident, for example, as bright contrast features in the dark-field XTEM micrograph in Fig. 5.16c. Based upon $\bar{g} \cdot \bar{b}$ analyses, the loops are composed of 60° dislocations with ⟨110⟩ Burgers' vectors $\bar{b}$. The loops are not directly responsible for appreciable strain relaxation since they do not form misfit dislocation segments at the film/buffer-layer interface.[35] Nevertheless, Figure 5.13 reveals that the degree of strain in ultra-highly doped Si(001):B layers grown with $C_B > 5x10^{19}$ cm^{-3} at T_s = 800 °C is relatively low compared to similarly doped 600 °C films.

The dislocation loops are similar to those observed in annealed B-implanted Si wafers[36] where the loops form when implantation-induced-interstitials condense during subsequent annealing. Transient enhanced diffusion (TED)[36,37] of B occurs during annealing in the presence of Si self-interstitial concentrations estimated to be as high as 10^{19} cm^{-3}.[38] TED is associated with B cluster formation in bulk Si through the formation of fast-diffusing substitutional-B/interstitial-Si complexes[36] which can interact with substitutional B atoms to form split-substitutional B pairs and possibly larger clusters[36,37] (in all cases smaller than the TEM resolution limit, ≈ 50 Å). In the present experiments, I show in section 5.3.1 that the B-pairs impart a small compressive in-plane strain on the Si(001) lattice. Thus, nanoscale B clustering via TED combined with B decoration of dislocation loops and stacking faults during growth at

high temperatures results in reduced in-plane tensile strain and electrical activity in ultra-highly doped films.

5.3. Discussion

I have shown that during GS-MBE of Si(001):B from Si_2H_6/B_2H_6 mixtures, B is incorporated into electrically-active lattice sites via a thermally-activated reaction path for concentrations C_B up to C_B^*. The incorporated B strongly segregates to the second layer where the steady-state coverage θ_B increases with C_B to reach saturation, $\theta_{B,sat}$ = 0.5 ML, when $C_B = C_B^*$. At T_s = 600 °C, C_B^* is 2.5×10^{20} cm^{-3} and $\theta_{B,sat}$ occurs with an incident flux ratio $J_{B_2H_6}/J_{Si_2H_6}$ of 0.25. With further increases in the flux ratio, segregated B in excess of $\theta_{B,sat}$ goes to the first layer where it affects the reaction path of subsequently adsorbed B_2H_6 and results, as discussed below, in the incorporation of non-electrically-active B.

C_B increases linearly with $J_{B_2H_6}/J_{Si_2H_6}$ up to a ratio of 0.25 at T_s = 600 °C, and more rapidly at higher flux ratios. Over the linear range, C_B is equal to N_B, the electrically-active B concentration, while at higher total B concentrations, N_B becomes progressively smaller than C_B. HR-XRD measurements show that $a_\perp$ decreases linearly with C_B for values $\leq C_B^*$ while at higher B concentrations, there is a discontinuous change in $a_\perp(C_B)$ and the curve becomes non-linear. The sum of these results indicates that for film growth conditions giving rise to total doping concentrations above C_B^*, B incorporation occurs through at least two parallel reaction paths.

For most common p- and n-type dopants, including Al, Ga, P, and Sb, the electrically-active dopant fraction progressively decreases as the total doping concentration is increased above the kinetic solubility limit.[39] This is due to the formation of precipitates which, once

nucleated, act as sinks for dopant atoms and thus decrease the doping concentration in substitutional Si sites.[40] In the present case, however, the electrically-active dopant concentration continues to increase even though the active fraction decreases dramatically. Moreover, extensive TEM analyses, in both low- and high-resolution modes, of samples with $C_B > C_B^*$ reveal no evidence of B precipitates, implying that, if present, they must be in the form of small ($\lesssim$ 50 Å, the TEM detection limit for low-Z elements) dispersed nano-clusters.

Temperature-dependent Hall measurements carried out on layers grown with $C_B \leq C_B^*$ at T_s = 600 °C demonstrate that hole mobilities are equal to, or better than, the best bulk Si:B values up to the highest doping concentrations reported and, for layers with higher concentrations, equal to theoretical values. Moreover, the room-temperature hole mobility remains essentially constant even as C_B is increased almost an order of magnitude above C_B^* to $1.6\text{x}10^{21}$ cm^{-3} for which the inactive dopant concentration (C_B-N_B) is $4.8\text{x}10^{20}$ cm^{-3} ($N_B/C_B = 0.3$), demonstrating that electrically-inactive B has a small charge scattering cross-section. As C_B is increased further, however, the film resistivity increases and the hole mobility decreases rapidly indicating the onset of an additional carrier scattering mechanism which, based upon HR-XRD and TEM contrast analyses, is strain-induced disorder.

5.3.1. B-induced strain and microstructural changes

Tensile strain in Si associated with B doping at concentrations above ≈ $5\text{x}10^{18}$ cm^{-3} is quantitatively measurable by HR-XRD. The rate of change in the macroscopic strain state provides useful insights regarding the lattice site, as well as the ensemble, into which B is incorporated. In section 5.2.5, high-resolution reciprocal lattice maps obtained from asymmetric

reflections show that all films remain fully commensurate, even up to the highest B concentrations investigated, 24 at%. The in-plane Si:B layer lattice constants are identical to those of the Si substrate within one part in 10^4. However, as shown in Fig. 5.17, the out-of-plane lattice parameter $a_\perp$ decreases linearly with C_B, consistent with Vegard's rule, demonstrating (together with the combined SIMS and Hall-effect results in Fig. 5.6) that all B is incorporated into electrically-active substitutional sites for concentrations up to C_B^*. The data in this range are very well fit with the expression

$$a_\perp = a_{Si} + \beta N_B, \tag{5.2}$$

for which a_{Si} is the bulk Si lattice parameter (5.4310 Å) and N_B is the active B concentration. β, the strain rate coefficient, is given by

$$\beta = \left[\left(\frac{1+\nu_{Si}}{1-\nu_{Si}}\right)\left(\frac{a_B - a_{Si}}{n_{Si}}\right)\right]. \tag{5.3}$$

ν_{Si} and n_{Si} in equation 5.3 are the Poisson ratio (0.278) and atomic density (5×10^{22} cm^{-3}) of Si while a_B is the lattice constant of diamond-structure B (4.10 Å) calculated using the B tetrahedral covalent radius, 0.88 Å.[41] Substituting these terms into equation 5.3 yields a value for β of -4.02×10^{-23} Å cm^3 in very good agreement with the best fit value in Fig. 5.17 of -4.5×10^{-23} Å cm^3. The experimentally determined value of β was used to calculate the Si-B bond length $r_{Si\text{-}B} = 2.04\pm0.02$ Å following the procedure outlined in Appendix A The result is within the range of that reported by Weir et al.,[42] $r_{Si\text{-}B} = 2.0\text{-}2.1$ Å, based upon an analysis of glancing-angle XRD patterns obtained from an ordered Si(001):B monolayer containing 0.5 ML of B.

As C_B is increased above C_B^*, $a_\perp$ continues to decrease, but at a slower rate, and $a_\perp(C_B)$ becomes non-linear with B incorporated into *both* electrically active and inactive sites. A

comparison of the $a_\perp$ vs C_B relationships for C_B less than and greater than $C_B^* = 2.5\text{x}10^{20}$ cm^{-3} at T_s = 600 °C shows that while the incorporation of electrically-active B results in purely tensile in-plane strain, electrically-inactive B in the configuration gives rise to compression.

Detailed plan-view and cross-sectional TEM analyses, including high-resolution, were carried out on representative samples spanning the entire B concentration and growth-temperature ranges investigated. Consistent with the HR-XRD results, there was no evidence of precipitates or misfit dislocations in any sample. For layers with $C_B \lesssim 2\text{x}10^{20}$ cm^{-3}, the Si:B film/buffer-layer interface is essentially indiscernible, even under dark-field imaging conditions.

The full set of $a_\perp(C_B)$ data, including the kink in the curve signifying the point at which inactive B first begins to be incorporated, is well described, as shown in Fig. 5.17, by the addition of another term to equation 5.3 to yield

$$a_\perp = a_{Si} + \beta N_B + \alpha(C_B - N_B). \qquad (5.4)$$

α, the inactive-B strain coefficient, is $4.8\text{x}10^{-24}$ Å-cm^3. The fact that the entire curve, linear plus nonlinear portions, can be fit with a single value of α suggests that all inactive B is incorporated into a single type of configuration, whose size remains constant irrespective of C_B.

The value of α obtained from equation 5.4 and Fig. 5.17 was used to test potential B cluster bonding configurations. TEM and electronic transport data rule out the presence of large B clusters. Of the small cluster sizes which theory indicates may be stable — clusters with 2, 3, 6, and 12 atoms[37,43-46] — only B pairs are consistent our measured strain behavior. This is in agreement with recent *ab-initio* local-density approximation calculations,[37,45] as well as tight-binding computations employing the Stillinger-Weber potential,[46] which predict that the most

stable B clusters in Si are B pairs. The lowest-energy B-pair configuration is the split-substitutional in which the B-B bond is oriented along ⟨100⟩ with bond lengths $r_{Si-B_{pair}} = 2.01$ and $r_{B-B} = 1.60$ Å.[37,45]

In a bulk crystal, such as was assumed in the above calculations, there is no reason to expect an anisotropy in the ⟨100⟩ orientations of B-B dimer bonds. A strained layer, however, can induce a preferential B-B bond orientation which, in the present case with the films in tension, would correspond to the [001] growth direction. Alternatively, the B-B orientation may be controlled by the reaction path of the incorporating B pair such that its orientation is frozen before film strain can play a role.

I have computed (see Appendix A), based upon the strain coefficient α determined from equation 5.4, the bond length $r_{Si-B_{pair}}$ between nearest-neighbor Si and paired B atoms for three cases: (1) all B pairs aligned along the [001] growth direction, (2) all B pairs aligned in-plane and distributed equally along [100] and [010] directions, and (3) B pairs distributed randomly in the three orthogonal directions. The results yield $r_{Si-B_{pair}}$ = 1.70, 2.18, and 2.01±0.04 Å, respectively. $r_{Si-B_{pair}}$ for case (1) can be dismissed immediately since it is 15% less than r_{Si-B} and therefore unphysical. $r_{Si-B_{pair}}$ for case (3), however, is in agreement with total energy calculations for randomly-aligned ⟨100⟩ B pairs[45] suggesting that non-electrically-active B is incorporated into GS-MBE Si(001) as B pairs in substitutional lattice sites in which the B-B bonds are distributed equally along the three cube axes. This is consistent with the continued increase, although at a slower rate, in N_B with increasing $C_B > C_B^*$ through parallel B and B-pair reaction channels. The B pairs would have an sp^2-bonded trigonally-coordinated symmetry in agreement with our near-edge x-ray absorption fine structure measurements.[47] Moreover, B is

trivalent and should therefore be electrically-inactive, as observed experimentally, due to being bond-saturated in this configuration.

Dark-field $\bar{g} = 004$ XTEM micrographs obtained from layers with $C_B \gtrsim 2x10^{20}$ cm^{-3}, while free of precipitates and misfit dislocations, exhibit a mottled dark contrast with respect to the substrate (Fig. 5.15). Correspondingly, increasing C_B in this concentration range results in HR-XRD Bragg peaks from the film becoming broader and less intense as more diffuse scattering is observed. Reciprocal lattice maps show that peak broadening is particularly pronounced in the ω-2θ direction indicating a wide distribution of interplanar spacings. This is interpreted as being due to lattice plane buckling in the presence of a high concentration of localized B-induced strain fields.

5.3.2. Boron incorporation kinetics

Our group has previously published a detailed predictive model, with no fitting parameters, for the deposition rate R of GS-MBE Si(001) as a function of incident Si_2H_6 flux $J_{Si_2H_6}$ and film growth temperature T_s.[48] The model contains terms accounting for a stepwise reaction path including dissociative chemisorption, a series of surface decomposition reactions, and first-order H_2 desorption from Si monohydride. The Si_2H_6 reactive sticking probability $S_{Si_2H_6}$ exhibits a small negative activation energy, $E_{Si} \approx -0.16$ eV,[49] indicating that chemisorption is precursor-mediated.

The Si(001) growth kinetics model was later extended to predict B concentrations incorporated from Si_2H_6/B_2H_6 mixtures during Si(001):B deposition with $C_B \lesssim 1x10^{19}$ cm^{-3}.[4] B_2H_6 chemisorption, in analogy with Si_2H_6 results, is taken to be second order in this

concentration range and the reactive sticking probability is thermally activated (unlike the case for Si_2H_6) with a small positive activation energy, $E_B = 0.18$ eV. $S_{B_2H_6}$ and $S_{Si_2H_6}$ were found to be independent leading to the following simple expression for C_B,

$$C_{B,calc} = \frac{S_{B_2H_6} J_{B_2H_6}}{S_{Si_2H_6} J_{Si_2H_6}} N_{Si} \qquad (5.5)$$

in which N_{Si} is the atomic density of Si, $5x10^{22}$ cm^{-3}. Figure 5.2 shows that the $\ln(C_B)$ vs $J_{B_2H_6}/J_{Si_2H_6}$ results obtained in the present experiments are well described by equation 5.5 for B concentrations up to C_B^*. Values for $S_{Si_2H_6}(T_s)$ and $S_{B_2H_6}(T_s)$ were taken from refs. 49 and 4, respectively. Note that the overall temperature-dependence for B incorporation in equation 5.5 enters simply through the difference between the activation energies for B and Si chemisorption, where $E_B^{inc} = E_B - E_{Si} = 0.34$ eV.

The C_B vs $1/T_s$ data in Fig. 5.3, obtained with $J_{B_2H_6}/J_{Si_2H_6}$ ratios ranging from $9.3x10^{-5}$ to 0.25, are in excellent agreement with equation 5.5. That is, the slopes of these curves remain constant yielding $E_B^{inc} = 0.34 \pm 0.01$ eV. The reaction path for B incorporation into electrically-active sites in this concentration range proceeds through a B-induced ordered c4x4 reconstruction in the second layer,[3] with a maximum coverage of 0.5 ML, which serves as the reservoir for B incorporation into "bulk" substitutional sites.

Figure 5.3 also shows that E_B^{inc} is no longer constant at $J_{B_2H_6}/J_{Si_2H_6}$ values ≥ 0.3. In this range, E_B^{inc} decreases continuously, indicating the onset of a parallel incorporation path which is precursor mediated, and actually becomes negative for $J_{B_2H_6}/J_{Si_2H_6} \gtrsim 2$. At the highest flux ratio used in these experiments, $J_{B_2H_6}/J_{Si_2H_6} = 3.0$, E_B^{inc} reaches a value of -0.06 eV. $J_{B_2H_6}/J_{Si_2H_6} \geq 0.3$ corresponds to deposition conditions, over the growth-temperature range

550-800 °C, for which B segregation results in second-layer coverages which exceed $\theta_{B,sat}$ with the excess B occupying sites at the outer surface.[2,3]

The inset in Fig. 5.6 shows that while the electrically-active B fraction N_B/C_B decreases rapidly with $C_B > C_B^*$, the total (active plus inactive) B incorporation rate increases as a function of $J_{B_2H_6}/J_{Si_2H_6}$ (see inset in Fig. 5.2). The two results are correlated, and together with post-annealing data showing that N_B/C_B remains constant, indicate that electrically-inactive B is incorporated directly from the growth surface rather than forming in the bulk. Furthermore, the fact that N_B/C_B is observed to increase with increasing T_s is circumstantial evidence that inactive B is chemisorbed directly as B-pairs, i.e. B_2H_6 absorption kinetics become precursor mediated rather than thermally activated in the presence of surface B. (If B_2H_6 adsorption remained second order and B pairs formed via surface diffusion and recombination, then N_B/C_B would be expected to decrease with T_s due simply to a higher B-B encounter probability.)

The total B incorporation probability can be expressed as the product of the individual incorporation probabilities for electrically-active B, $S^{B}_{B_2H_6}$, and inactive B, $S^{B-B}_{B_2H_6}$, where

$$S_{B_2H_6} = \left(S^{B}_{B_2H_6}\right)^{f_a} \left(S^{B-B}_{B_2H_6}\right)^{(1-f_a)} \tag{5.6}$$

and f_a and $(1-f_a)$ are the measured fractions of electrically active and inactive B. This leads to an expression (see Appendix B) for the overall activation energy (i.e., the slope of the $\ln(C_B)$ vs $J_{B_2H_6}/J_{Si_2H_6}$ curves in Fig. 5.3) given by

$$E_B^{inc} = \left\{f_a E_B + (1-f_a) E_{B\text{-}B}\right\} - E_{Si} + K \tag{5.7}$$

where $E_{B\text{-}B}$ is the rate-limiting activation energy for B incorporation as electrically-inactive B pairs on substitutional Si lattice sites and K is a temperature-independent constant. All data in

Figs. 5.2 and 5.3, covering the entire range of $J_{B_2H_6}/J_{Si_2H_6}$ and T_s values investigated in these experiments, including that corresponding to $C_B > C_B^*$, are very well described by the combination of equations 5.5-5.7 with $E_{B\text{-}B} = -0.23 \pm 0.04$. Calculated results are represented in Fig. 5.3 by solid lines.

5.3.3. High-temperature growth ($T_s \geq 700$ °C)

The reaction path for B incorporation into Si at ultra-high doping concentrations becomes more complex at growth temperatures $T_s \geq 700$ °C. This is most easily seen by comparing results obtained at $T_s = 600$ and 800 °C in Fig. 5.13. At the lower growth temperatures, all B atoms are incorporated into substitutional electrically-active sites at concentrations C_B up to C_B^* (2.5×10^{20} cm^{-3} at $T_s = 600$ °C) corresponding to the point at which θ_B in the second layer reaches $\theta_{B,sat} = 0.5$ ML. As C_B is increased above C_B^* with $T_s < 700$ °C, excess B segregates to the outer surface[3] allowing direct incorporation of B in the form of electrically-inactive clusters (see discussion, section 5.3.2). This occurs in addition to (but not at the expense of) the continued incorporation of substitutional electrically-active B from the second layer. The overall B incorporation changes at $T_s \geq 700$ °C, however, as B is found to reside in electrically-inactive sites when $\theta_B < \theta_{B,sat}$; that is, in the absence of B at the outer surface.

For all growth temperatures used in these experiments, B segregation is in the equilibrium regime[3] and, hence, the B segregation ratio decreases with increasing T_s. Thus, the B concentration C_B^* at which θ_B reaches saturation increases with T_s.[30] In addition, Fig. 5.2 shows that the degree of deviation from a linear variation in C_B as a function of $J_{B_2H_6}/J_{Si_2H_6}$ decreases with increasing T_s. Both of these effects would favor higher electrically-active B concentrations

with a correspondingly higher strain at T_s = 800 °C than at 600 °C. However, as shown by the results in Fig. 5.13, the opposite is observed. The B concentration at which both $a_{\perp}(C_B)$ and $N_B(C_B)$ become non-linear and at which B begins to be incorporated into non-electrically-active sites is reduced from $2.5x10^{20}$ cm^{-3} at T_s = 600 °C to $5x10^{19}$ cm^{-3} at 800 °C.

A strong clue toward explaining the B incorporation behavior at high growth temperatures derives from XTEM micrographs (Fig. 5.16c) showing that layers exhibiting significant surface roughening also contain a large number density of dislocation loops and 111 stacking faults. It is well documented that the presence of dislocation loops of the type observed in Fig. 5.16c indicate high Si self-interstitial concentrations.[36,41] The interstitials deactivate B acceptors in a TED-like clustering mechanism, as well as by inducing extended defects which are subsequently decorated by B atoms. The injection mechanism for Si self-interstitials at concentrations in excess of equilibrium values appears to be related to surface roughening. It is clear that this is not a purely thermal effect since post-annealing (up to 1100 °C for 12 h) of 100%-electrically-active B-doped Si(001) layers grown at 600 °C with $C_B = 2x10^{20}$ cm^{-3} and smooth surfaces did not result in any measurable loss in electrical activity.

The above phenomena, including the formation of dislocation loops, are not observed during growth of ultra-highly doped Si(001):B at $T_s \leq 600$ °C due to both thermal quenching and H-induced reduction of adatom surface mobilities.[50] Low growth temperatures, with their associated high steady-state H coverages, do not provide the thermal activation necessary for the massive uphill diffusional transport of atoms required for roughening.[35] At these temperatures, complete electrical activity is maintained for B concentrations up to C_B^*.

5.3.4. Transport properties

The quantitative agreement between the total incorporated B concentration C_B, obtained independently from SIMS and HR-XRD measurements, and active B concentrations N_B determined from Hall-effect results at $C_B = N_B \leq 2.5x10^{20}$ cm^{-3} for GS-MBE Si(001):B films grown at $T_s = 600$ °C indicates that all B atoms in these layers occupy substitutional electrically-active sites in the Si lattice. This is further substantiated by the good agreement in Figs. 5.7 and 5.9 between our measured $\rho(C_B)$ and $\mu(C_B)$ results and theoretical predictions. Room-temperature hole mobilities were found to be equal to maximum theoretical values up to the limit of 100% B activation, $C_B^* = 2.5x10^{20}$ cm^{-3}, and μ_{300K} remained essentially constant for B concentrations even up to almost an order of magnitude higher. This is consistent with inactive B being incorporated as pairs on substitutional Si sites. Such a configuration is expected to lead to relatively small carrier scattering cross-sections since the defect is neutral and resides on a substitutional site. μ_{300K} ranges from 168 to 47 to 41 to 8 $cm^2 V^{-1}s^{-1}$ at $C_B = 1.7x10^{17}$, $2.5x10^{20}$, $1.6x10^{21}$, and $1.2x10^{22}$ cm^{-3}, respectively.

While μ_{300K} remains approximately constant over the B concentration range between $\approx 2.5x10^{20}$ cm^{-3} and $1.6x10^{21}$ cm^{-3} ($N_B/C_B = 0$ to 0.3), it decreases abruptly at higher B concentrations. The decrease is due to additional charge scattering resulting from the breakdown in long-range order due to the high density of randomly-distributed local strain fields emanating from lattice dilatations caused by B and B-pairs residing on substitutional Si sites. The distribution of Si bond lengths and angles becomes progressively wider with increasing C_B at these very high B concentrations.

Temperature-dependent hole mobilities were shown to vary smoothly from being characteristic of itinerant hole transport when C_B is less than $\lesssim 3x10^{18}$ cm^{-3} to hopping conductivity for $C_B \simeq 3x10^{18}$ -10^{19} cm^{-3} to metallic at higher concentrations. In the itinerant hole transport regime, μ is primarily limited by lattice scattering near room temperature and ionized-impurity scattering at low temperatures. As C_B is increased, the transition from phonon-dominated to ionized-impurity dominated scattering shifts to progressively higher temperatures. With C_B above $3x10^{18}$ cm^{-3}, band-tailing significantly reduces carrier freezeout thereby increasing the number density of filled acceptor states sufficiently to allow hopping conduction over the entire measured temperature range. This puts a lower limit on hole mobility. Further increases in $C_B > 10^{19}$ cm^{-3} shifts the conductivity into the metallic regime.

5.4. Conclusions

In this chapter I systematically probed the B bonding configuration, and incorporation kinetics to determine the origin of electrically inactive B species. Si(001) layers doped with B concentrations C_B between $1x10^{17}$ and $1.2x10^{22}$ cm^{-3} were grown on Si(001)2x1 at temperatures T_s = 500-850 °C by GS-MBE from Si_2H_6 and B_2H_6. C_B increases linearly with the incident precursor flux ratio $J_{B_2H_6}/J_{Si_2H_6}$ and, for T_s < 700 °C, B is incorporated into substitutional electrically-active sites at concentrations up to C_B^*. For T_s = 600 °C, C_B^* is $2.5x10^{20}$ cm^{-3}. At higher B concentrations, C_B increases faster than $J_{B_2H_6}/J_{Si_2H_6}$ and there is a large and discontinuous decrease in the electrically-active fraction of incorporated B. However, the total activated B concentration continues to increase and reaches a value of $N_B = 1.3x10^{21}$ cm^{-3} with $C_B = 1.2x10^{22}$ cm^{-3}. Resistivities are in good agreement with theoretical values to C_B^* for which

ρ_{300K} = 300 μΩ-cm. Conductivity mobilities are equal to theoretical maximum values to $C_B = 1.6x10^{21}$ cm^{-3}. HR-XRD and reciprocal space mapping measurements show that all films are fully strained. No B precipitates, or misfit dislocations, were detected by HR-XRD and TEM analyses, even in films with $C_B = 1.2x10^{22}$ cm^{-3} (24 at% B). The lattice constant in the film growth direction $a_\perp$ decreases linearly with increasing C_B up to the limit of full electrical activation and continues to decrease, but non-linearly, with $C_B > C_B^*$.

HR-XRD, SIMS, Hall-effect, and TEM data were used in concert to determine the nature and lattice site of electrically-inactive B. TEM/XTEM analyses reveal that B clusters must be smaller than ≃ 50 Å, from HR-XRD that the macroscopic strain contribution per inactive B atom is constant, and from Hall measurements that the active B concentration continues to increase even when $C_B > C_B^*$. These results indicate that B is present in small highly-dispersed nanoclusters of constant size. Based upon a detailed analysis of the out-of-plane Si(001):B lattice constants as a function of active and inactive B concentrations, I show that inactive B is incorporated as trigonally-coordinated B pairs on single Si sites and oriented with the B-B bond axis randomly aligned along ⟨001⟩ directions.

The fraction of inactive B decreases with increasing temperature indicating that the B pairing reaction is not diffusion controlled. Furthermore, the B concentration as a function of $J_{B_2H_6}/J_{Si_2H_6}$ becomes superlinear when $\theta_B > \theta_{B,sat}$, and the net increase in C_B is essentially equal to the concentration of inactive B. These factors support direct B pair incorporation at the growth surface. During high temperature growth ($T_s \geq 700$ °C), the situation is more complex. In addition to direct B incorporation at the surface, B clustering in the bulk is mediated by large

concentrations of interstitial point defects resulting in B deactivation during growth when C_B exceeds $5x10^{19}$ cm^{-3}.

B strongly surface segregates to the second-layer with a saturation coverage $\theta_{sat,B}$ of 0.5 ML (corresponding to $C_B = C_B^*$ for $T_s < 700$ °C). At higher C_B, $\theta_B > \theta_{sat,B}$ and B accumulates in the upper layer, as shown by thermally programmed desorption measurements. The presence of upper layer B modifies the interaction of B_2H_6 with the Si surface, and opens a parallel reaction channel whereby B incorporates as pairs which are electrically inactive but have a low carrier scattering cross-section. At $C_B > 2x10^{21}$ cm^{-3} carrier mobilities begin to degrade substantially. This is correlated with lattice plane buckling in response to local B-induced strain measured by x-ray diffraction as well as by TEM electron diffraction contrast measurements.

5.5 References

1. H. Kim, G. Glass, S.Y. Park, T. Spila, N. Taylor, J.R. Abelson, and J.E. Greene, Appl. Phys. Lett. **69**, 3869 (1996).
2. G. Glass, H. Kim, M.R. Sardela, Q. Lu, J.R.A. Carlsson, J.R. Abelson, and J.E. Greene, Surf. Sci. **392**, L63 (1997).
3. H. Kim, G. Glass, T. Spila, N. Taylor, S.Y. Park, J.R. Abelson, and J.E. Greene, J. Appl. Phys. **82**, 2288, (1997).
4. Q. Lu, T.R. Bramblett, N.-E. Lee, M.-A. Hasan, T. Karasawa, and J.E. Greene, J. Appl. Phys. **77**, 3067 (1995).
5. S.M. Sze, *Physics of Semiconductor Devices* (John Wiley and Sons, New York, 1981, 2nd Edition).
6. M.A. Shibib and F. A Lindholm, IEEE Trans. Elec. Dev. **ED-27**, 1304 (1980).
7. P.P. Debye and T. Kohane, Phys. Rev. **94**, 724 (1954).
8. F.J. Morin and J.P. Maita, Phys. Rev. **96**, 28 (1954).
9. J. Messier and J.M. Flores, J. Phys. Chem. Solids **24**, 1539 (1963).
10. L.C. Linares and S.S. Li, J. Electrochem. Soc. **128**, 601 (1981).
11. J.F. Lin, S.S. Li, L.C. Linares, and K.W. Teng, Solid State Electronics **24**, 827 (1981).

12. Q. Lu, M.R. Sardela Jr., T.R. Bramblett, and J.E. Greene, J. Appl. Phys. **80**, 4458 (1996).

13. N.F. Mott and W.D. Twose, Adv. Phys. **10**, 107 (1961).

14. D.S. Lee and J.G. Fossum, IEEE Trans. Elec. Dev. **ED-30**, 626 (1983).

15. N.F. Mott, Philos. Mag. **26**, 1015 (1972), N.F. Mott, Phys. Rev. B **44**, 265 (1981).

16. N.F. Mott and M. Kaveh, J. Phys. C **14**, L177 (1981).

17. H.S. Bennett, J. Appl. Phys. **59**, 2837 (1986).

18. M. Lax and J.C. Phillips, Phys. Rev. **110**, 41 (1958).

19. H. Frisch and S. Lloyd, Phys. Rev. **120**, 1175 (1960).

20. J.R. Klauder, Ann. Phys. **14**, 43 (1961). The third-level approximation is used here.

21. G.D. Mahan, J. Appl. Phys. **51**, 2634 (1980).

22. P.A. Sterne and J.C. Inkson, J. Appl. Phys. **52**, 6432 (1981).

23. S. Wagner, J. Electrochem. Soc. **119**, 1570 (1972).

24. G.A. Slack and M.A. Hussain, J. Appl. Phys. **70**, 2694 (1991).

25. D. Caughy and R. Thomas, Proc. IEEE **55**, 2192 (1967).

26. W.R Thurber, R.L. Mattis, Y.M. Liu, and J.J. Filliben, J. Electrochem. Soc. **127**, 2291 (1980).

27. M.A.G. Halliwell, M.H. Lyons, S.T. Davey, M. Hockley, C.G. Tuppen, and C.J. Gibbings, Semicond. Sci. Technol. **4**, 10 (1989); F. Bozso and Ph. Avouris, Phys. Rev. B **38**, 3943 (1988).

28. D. Taupin, Bull. Soc. Franc. Miner. Crist. **87**, 469 (1964).

29. S. Takagi, J. Phys. Soc. Jpn. **26**, 1239 (1969).

30. S.A. Barnett and J.E. Greene, Surf. Sci. **151**, 67 (1985).

31. P. Fewster, Semicond. Sci. Technol. **8**, 1915 (1993).

32. P. Fewster, J. Appl. Crystallogr. **22**, 64 (1989).

33. F.N. Schwettman, J. Appl. Phys. **45**, 1918 (1974), S.M. Sze, *Physics of Semiconductor Devices* (John Wiley and Sons, New York, 1981, 2nd Edition), G.L. Vick and K.M. Whittle, J. Electrochem. Soc. **119**, 1142 (1969).

34. D.D. Perovic, G.C. Weatherly, R.F. Egerton, D.C. Houghton, and T.E. Jackman, Phil. Mag. A **63**, 757 (1991).

35. H. Gao and W. Nix, Ann. Rev. Mater. Sci. **29**, 173 (1999).

36. P.A. Stolk, H.J. Gossmann, D.J. Eaglesham, and J.M. Poate, Nuc. Inst. Methods Phys. Res. B **96**, 187 (1995) and S. Takeda, Jpn. J. Appl. Phys. **30**, L639 (1991).

37. J. Zhu, T.D. de la Rubia, L.H. Yang, C. Mailhiot, G.H. Gilmer, Phys. Rev. B **54**, 4741 (1996); Appl. Phys. Lett. **74**, 3657 (1999).

38. P.A. Stolk, H.-J. Gossman, D.J. Eaglesham, and J.M. Poate, Mat. Sci. Eng. B, **36**, 275 (1996), M.D. Johnson, M.J. Caturla, and T.D. de la Rubia, J. Appl. Phys. **84**, 1963 (1998).

39. Reported equilibrium solid solubilities at 900 °C are: $6x10^{20}$ cm^{-3} for P, $3x10^{19}$ cm^{-3} for Sb, $2x10^{19}$ cm^{-3} for Ga, and $1.5x10^{19}$ cm^{-3} for Al. For B in Si, reported solid solubilities range from $2x10^{19}$ cm^{-3} at 700 °C to $8x10^{20}$ cm^{-3} at 1400 °C. See *Impurities and Defects in Group IV Elements and III-V Compounds*, eds. : O. Madelung and M. Schulz, Landolt-Börnstein, New Series, Group III, Vol. 22, Pt. a (Springer, Berlin, 1989).

40. P. Ostoja, D. Nobili, A. Armigliato, and R. Angelucci, J. Electrochem. Soc. **123**, 124 (1976).

41. *Handbook of Chemistry and Physics*, ed.: D.R. Lide, 77th Edition, (CRC Press, Boca Raton, Florida, 1996).

42. B.E. Weir, R. L Headrick, Q. Shen, L.C. Feldman, M.S. Hybertsen, M. Needels, M. Schluter, and T.R. Hart, Phys. Rev. B **46**, 12861 (1992).

43. R.C. Newman and R.S. Smith, Phys. Lett. **24A**, 671 (1967).

44. J. Yamauchi, N. Aoki, and I. Mizushima Phys. Rev. B **55**, R10 245 (1997).

45. E. Tarnow, J. Phys. Cond. Matter **4**, 5405 (1992).

46. W. Luo, P. B. Rasband, P. Clancy, and B. W. Roberts, J. Appl. Phys. **84**, 2476 (1998).

47. Vailionis, G. Glass, P. Desjardins, David G. Cahill, and J.E. Greene, Phys Rev. Lett. **82**, 4464 (1999).

48. T.R. Bramblett, Q. Lu, T. Karasawa, M.-A. Hasan, S.K. Jo, and J.E. Greene, J. Appl. Phys. **76**, 1884 (1994).

49. J.R. Engstrom, L.Q. Xia. M.J. Furjanic, and D.A. Hansen, Appl. Phys. Lett. **63**, 1821 (1993).

50. J.E. Vasek, Z. Zhang, C.T. Salling, and M.G. Lagally, Phys. Rev. B **51**, 17207, (1995), S. Jeong and A. Oshiyama, Phys. Rev. B **58**, 12958 (1998), J. Nara, T. Sasaki, and T. Ohno, Appl. Surf. Sci. **130-132**, 254 (1998).

Table 5.1. Effective hole concentrations p_e and mobilities μ obtained from temperature-dependent Hall-effect measurements of GS-MBE Si(001):B layers grown at $T_s = 600$ °C with B concentrations C_B ranging from 1.7×10^{17} to 1.2×10^{22} cm^{-3}.

C_B (cm^{-3})	p_e (cm^{-3}) T = 77 K	p_e (cm^{-3}) T = 150 K	p_e (cm^{-3}) T = 300 K	μ ($cm^2V^{-1}s^{-1}$) T = 77 K	μ ($cm^2V^{-1}s^{-1}$) T = 150 K	μ ($cm^2V^{-1}s^{-1}$) T = 300 K
1.7×10^{17}	2.4×10^{15}	7.0×10^{16}	1.8×10^{17}	1002	511	159
2.8×10^{17}	2.0×10^{16}	1.4×10^{17}	2.9×10^{17}	912	484	150
3.6×10^{17}	7.7×10^{15}	1.4×10^{17}	3.7×10^{17}	823	454	148
1.0×10^{18}	2.5×10^{16}	3.8×10^{17}	1.0×10^{18}	323	253	107
1.3×10^{18}	3.0×10^{16}	4.0×10^{17}	1.2×10^{18}	247	205	105
5.0×10^{18}	1.2×10^{19}	8.7×10^{18}	1.1×10^{19}	59	102	87
6.0×10^{18}	1.7×10^{19}	1.1×10^{19}	1.4×10^{19}	58	88	83
1.0×10^{19}	3.1×10^{19}	2.9×10^{19}	3.0×10^{19}	63	65	69
3.9×10^{19}	1.9×10^{20}	1.9×10^{20}	1.7×10^{20}	62	60	51
1.0×10^{20}	3.5×10^{20}	3.5×10^{20}	3.5×10^{20}	69	61	50
1.2×10^{20}	3.7×10^{20}	3.7×10^{20}	3.7×10^{20}	67	62	48
1.8×10^{20}	4.6×10^{20}	4.6×10^{20}	4.6×10^{20}	65	59	46
2.5×10^{20}	5.5×10^{20}	5.5×10^{20}	5.5×10^{20}	65	59	46
4.5×10^{20}	5.6×10^{20}	5.6×10^{20}	5.6×10^{20}	52	51	37
7.0×10^{20}	3.0×10^{20}	3.0×10^{20}	3.0×10^{20}	46	43	42
1.6×10^{21}	4.8×10^{20}	4.8×10^{20}	4.8×10^{20}	46	43	41
2.7×10^{21}	6.5×10^{20}	6.5×10^{20}	6.5×10^{20}	25	24	23
4.2×10^{21}	7.8×10^{20}	7.8×10^{20}	7.8×10^{20}	19	19	19
6.0×10^{21}	9.0×10^{20}	9.0×10^{20}	9.0×10^{20}	12	12	12
1.0×10^{22}	1.2×10^{21}	1.2×10^{21}	1.2×10^{21}	9	9	9
1.2×10^{22}	1.3×10^{21}	1.3×10^{21}	1.3×10^{21}	8	8	8

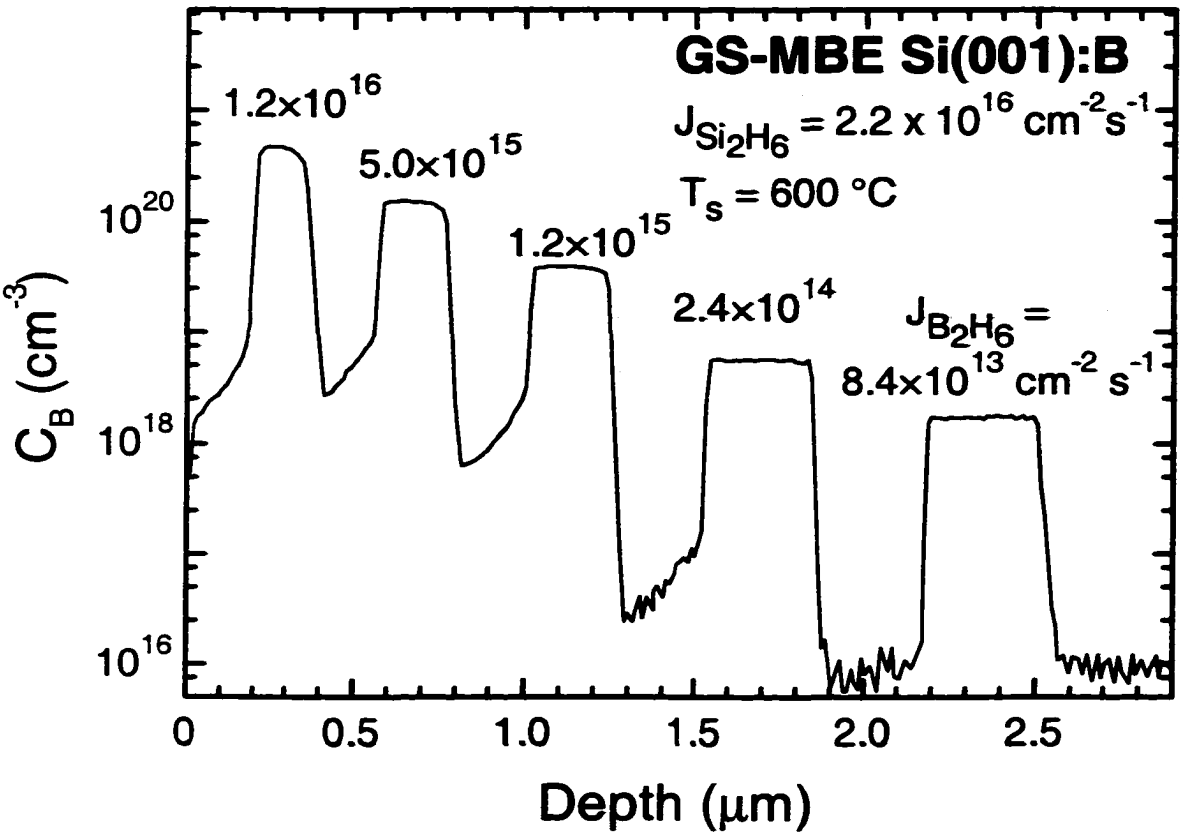

Figure 5.1. SIMS depth profiles through a B modulation-doped Si(001):B film grown by GS-MBE from Si_2H_6 and B_2H_6 at $T_s = 600$ °C. The incident Si_2H_6 flux was $J_{Si_2H_6} = 2.2 \times 10^{16}$ cm^{-2} s^{-1} while the B flux $J_{B_2H_6}$ was varied from 8.4×10^{13} to 1.2×10^{16} cm^{-2} s^{-1}. The deposition time for each layer was constant at 1 h.

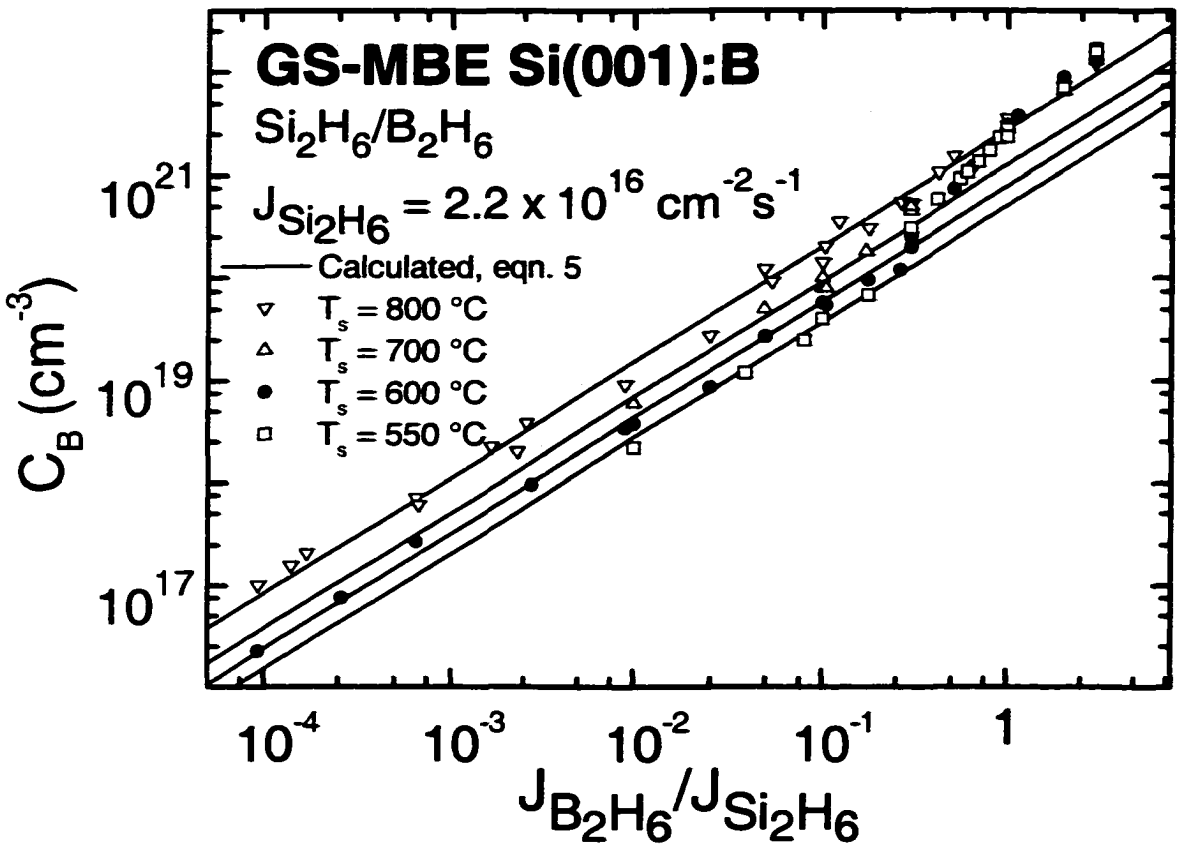

Figure 5.2. Incorporated B concentrations C_B in GS-MBE Si(001) layers as a function of the incident flux ratio $J_{B_2H_6}/J_{Si_2H_6}$ during growth at temperatures T_s of 550, 600, 700, and 800 °C. The inset shows the ratio of measured (SIMS) to calculated (equation 5.5) B concentration C_B as a function of $J_{B_2H_6}/J_{Si_2H_6}$.

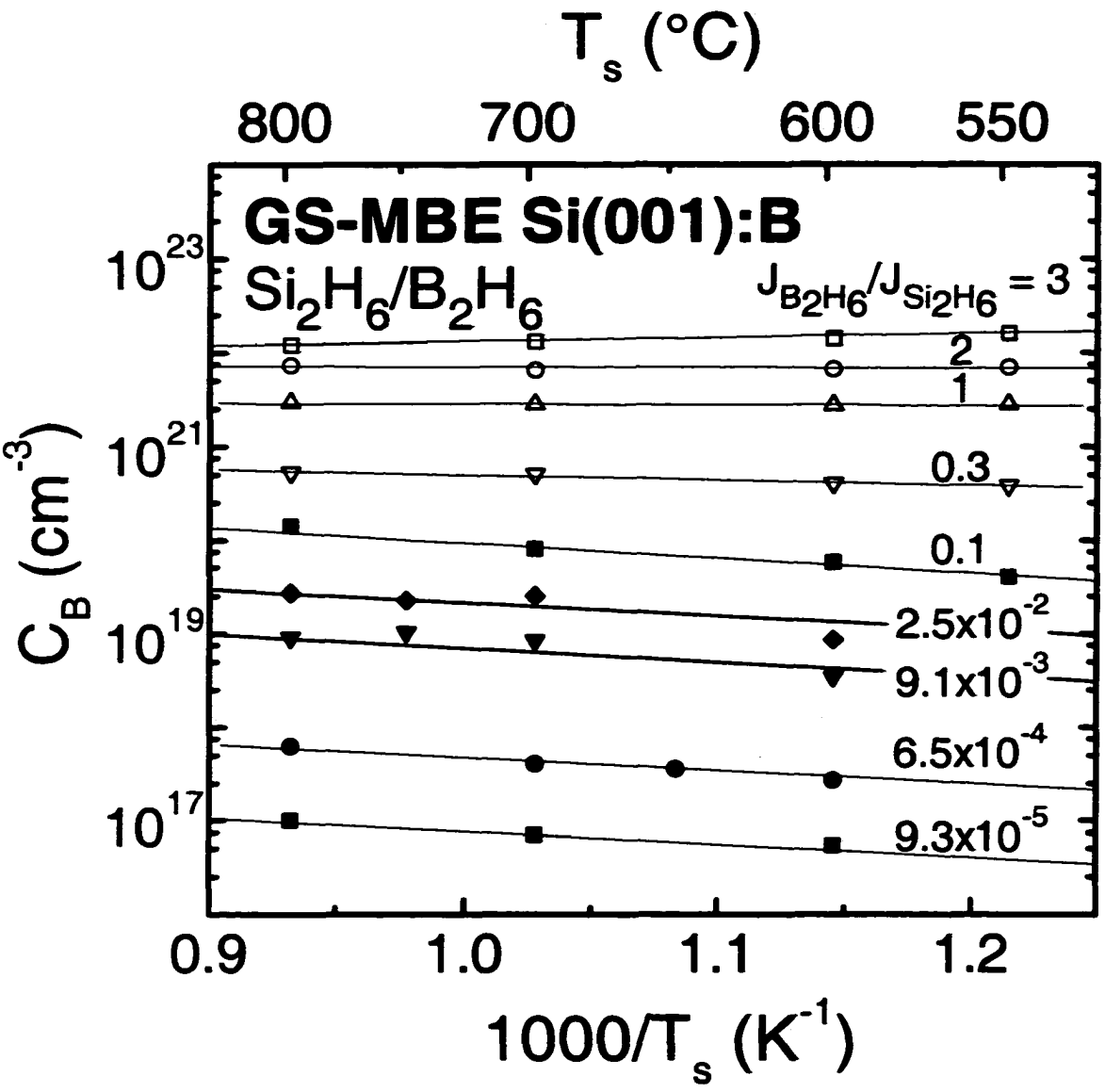

Figure 5.3. Incorporated B concentrations C_B in GS-MBE Si(001) layers as a function of the growth temperature T_s with incident flux ratios $J_{B_2H_6}/J_{Si_2H_6}$ maintained constant at values between 9.3×10^{-5} and 3.0.

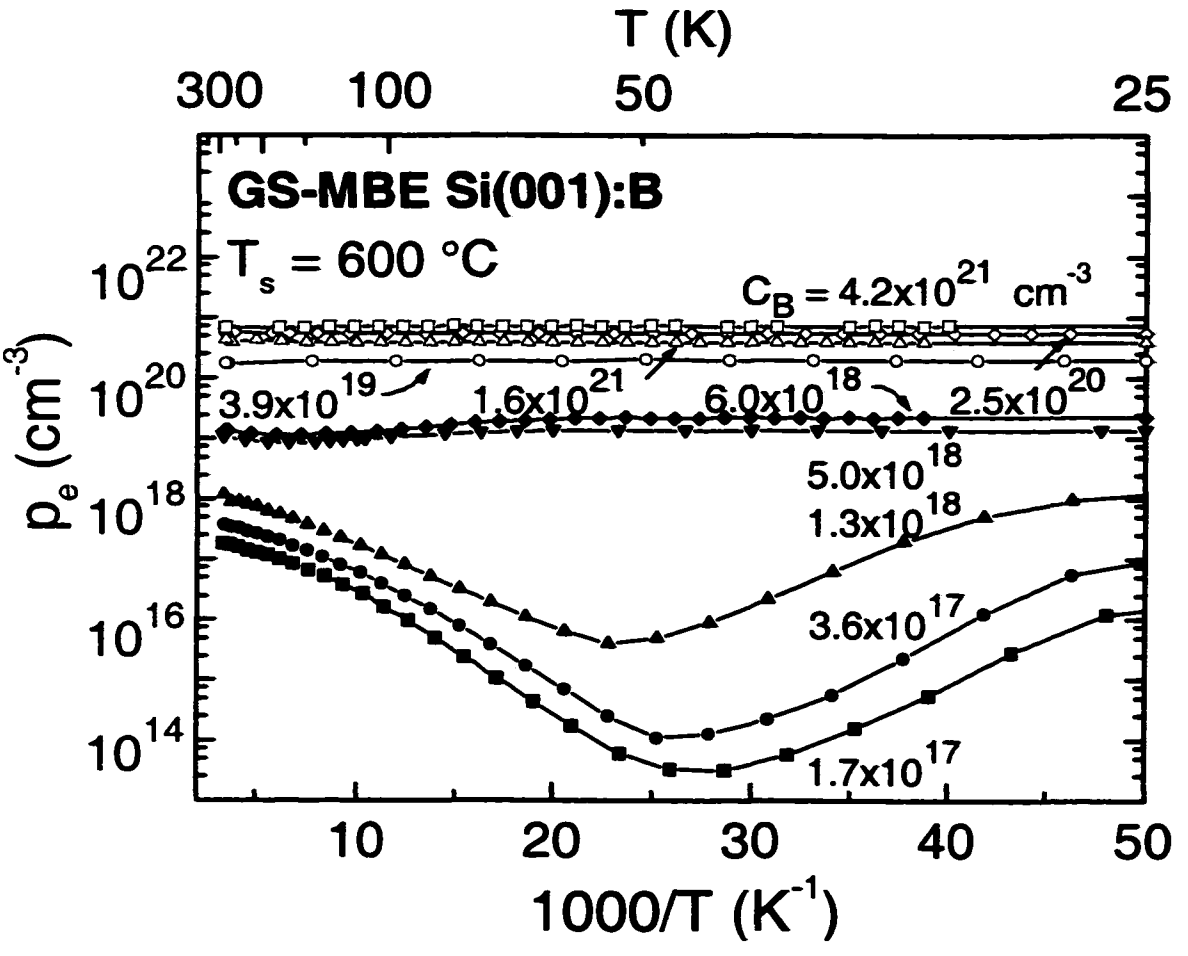

Figure 5.4. Representative data sets showing the effective hole concentration p_e as a function of temperature T for B-doped GS-MBE Si(001) layers grown from Si_2H_6/B_2H_6 mixtures at T_s = 600 °C. C_B is the total incorporated B concentration.

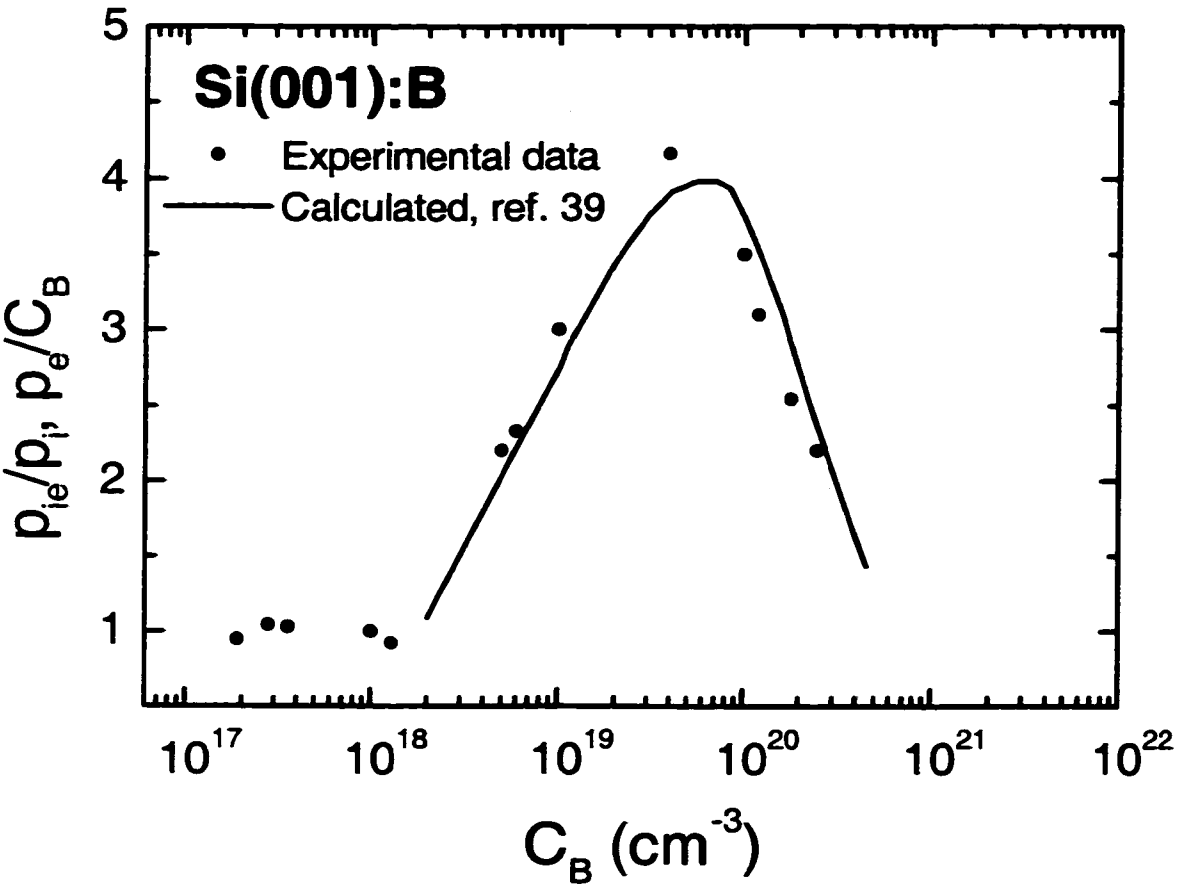

Figure 5.5. Experimental data and calculated (solid line) ratio of the room-temperature effective hole concentration p_e to the total incorporated B concentration C_B plotted as a function of C_B. p_{ie} and p_i are the measured and non-degenerate hole concentrations, respectively. The solid line shows the theoretical curve derived in ref. 17.

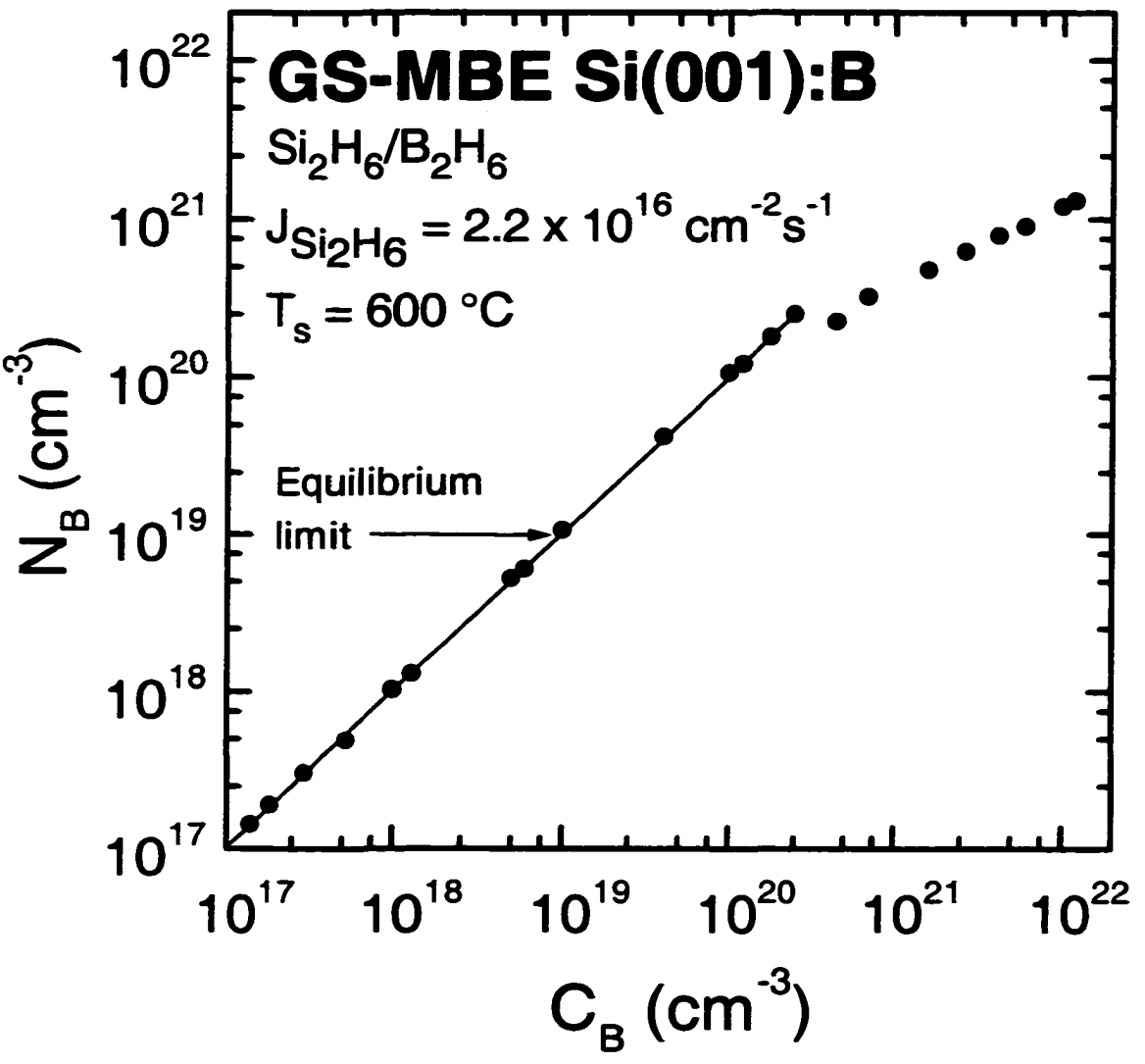

Figure 5.6. B acceptor concentrations N_B determined from Hall-effect measurements vs the total incorporated B concentration C_B obtained from SIMS analyses of GS-MBE Si(001) layers grown from Si_2H_6/B_2H_6 mixtures at T_s = 600 °C. The inset shows the fraction N_B/C_B of electrically-active B as a function of C_B.

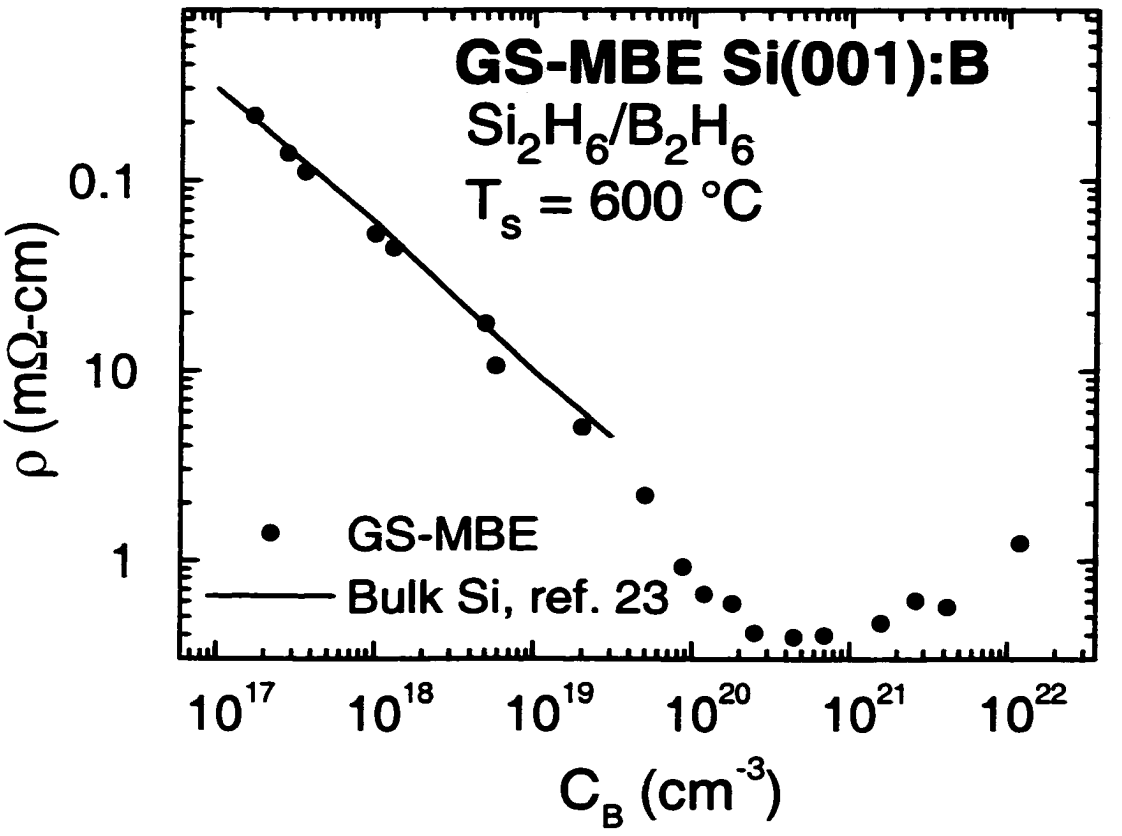

Figure 5.7. Room-temperature resistivity ρ as a function of B concentration C_B in GS-MBE Si(001):B layers grown from Si_2H_6/B_2H_6 mixtures at T_s = 600 °C. The solid line shows bulk Si data taken from ref. 23.

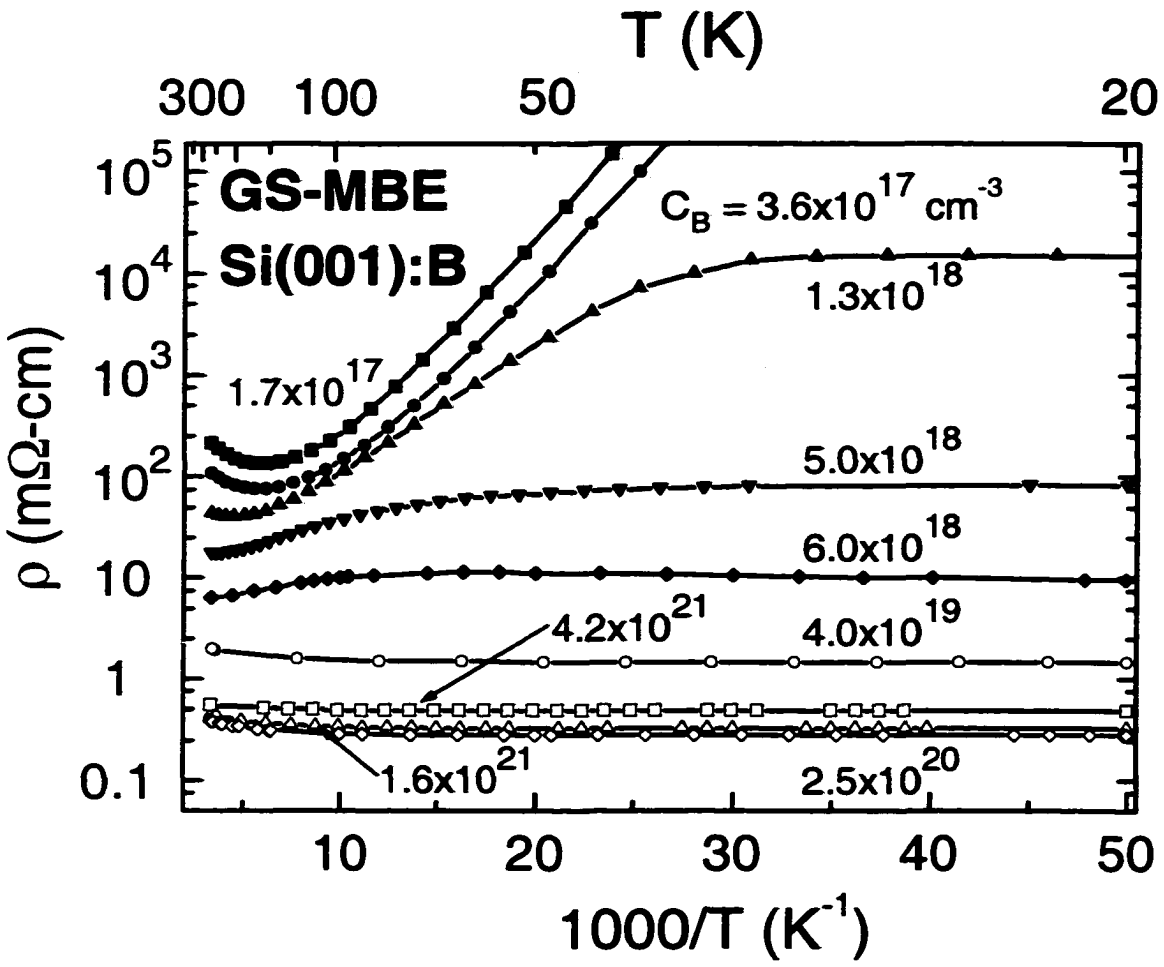

Figure 5.8. Representative data sets showing the resistivity ρ as a function of temperature T for B-doped GS-MBE Si(001) layers grown from Si_2H_6/B_2H_6 mixtures at $T_s = 600$ °C. C_B is the total incorporated B concentration.

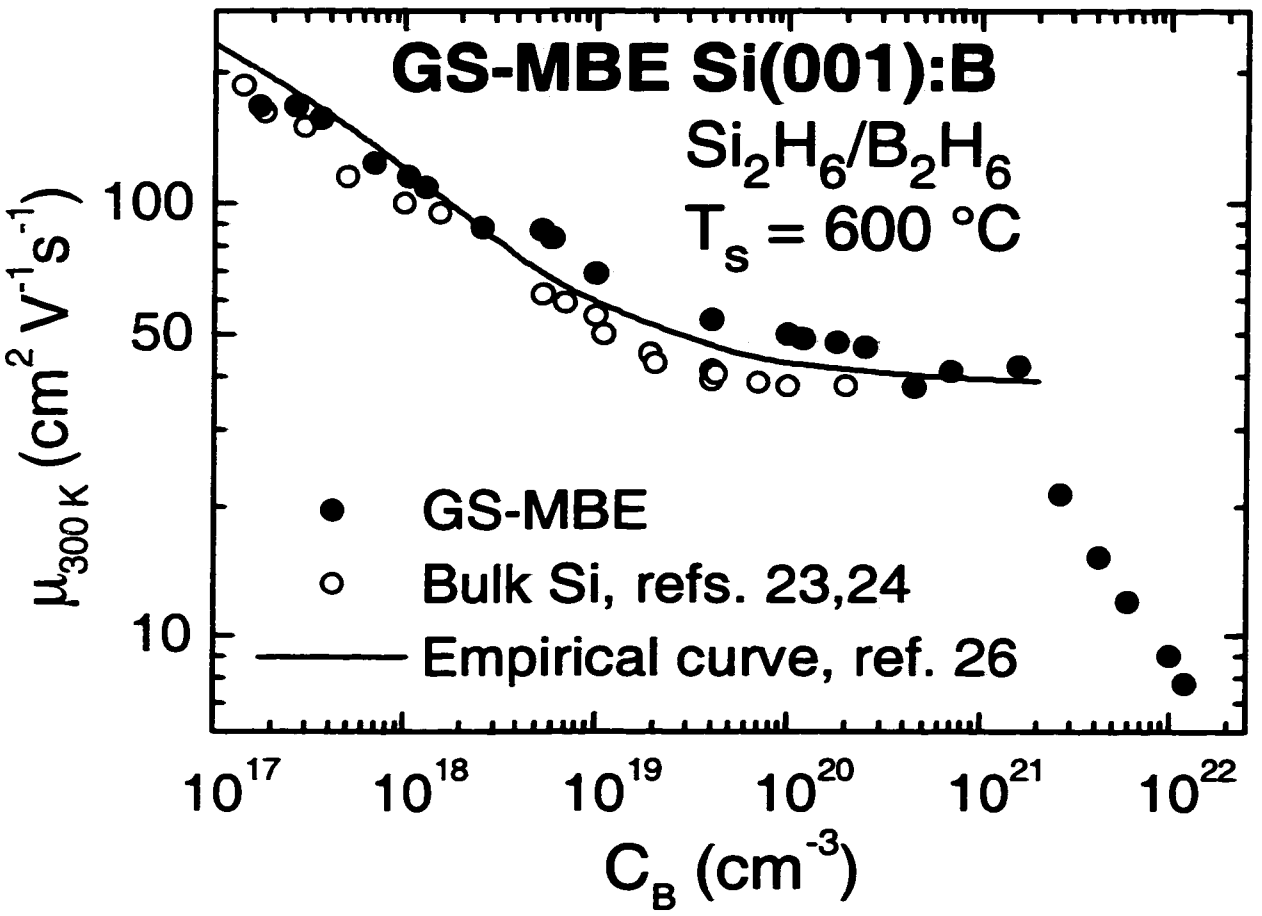

Figure 5.9. Room-temperature hole mobility μ as a function of B concentration C_B in Si:B. The filled circles are experimental data from GS-MBE Si(001):B layers grown from Si_2H_6/B_2H_6 mixtures at T_s = 600 °C, the open circles are bulk Si data taken from refs. 23 and 24, and the solid line is an empirical curve from ref. 26.

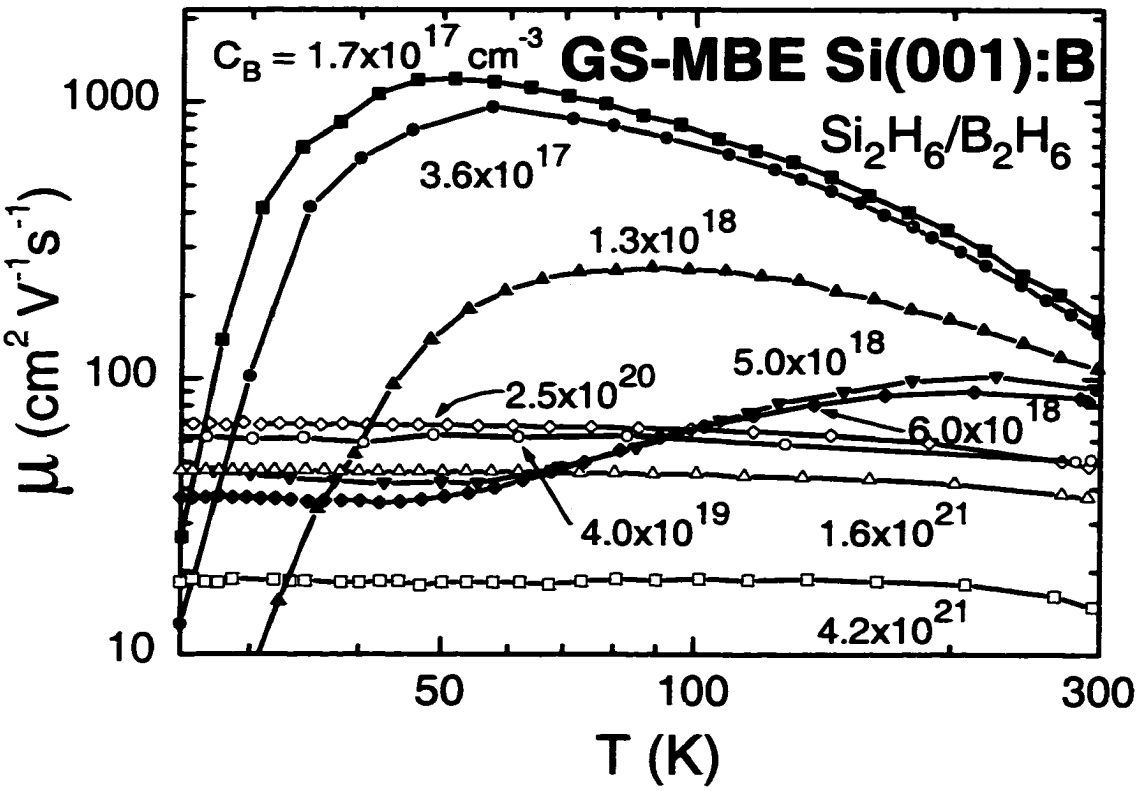

Figure 5.10. Representative data sets showing the hole mobility μ as a function of temperature for B-oped GS-MBE Si(001) layers grown from Si_2H_6/B_2H_6 mixtures at $T_s = 600$ °C. C_B is the total incorporated B.

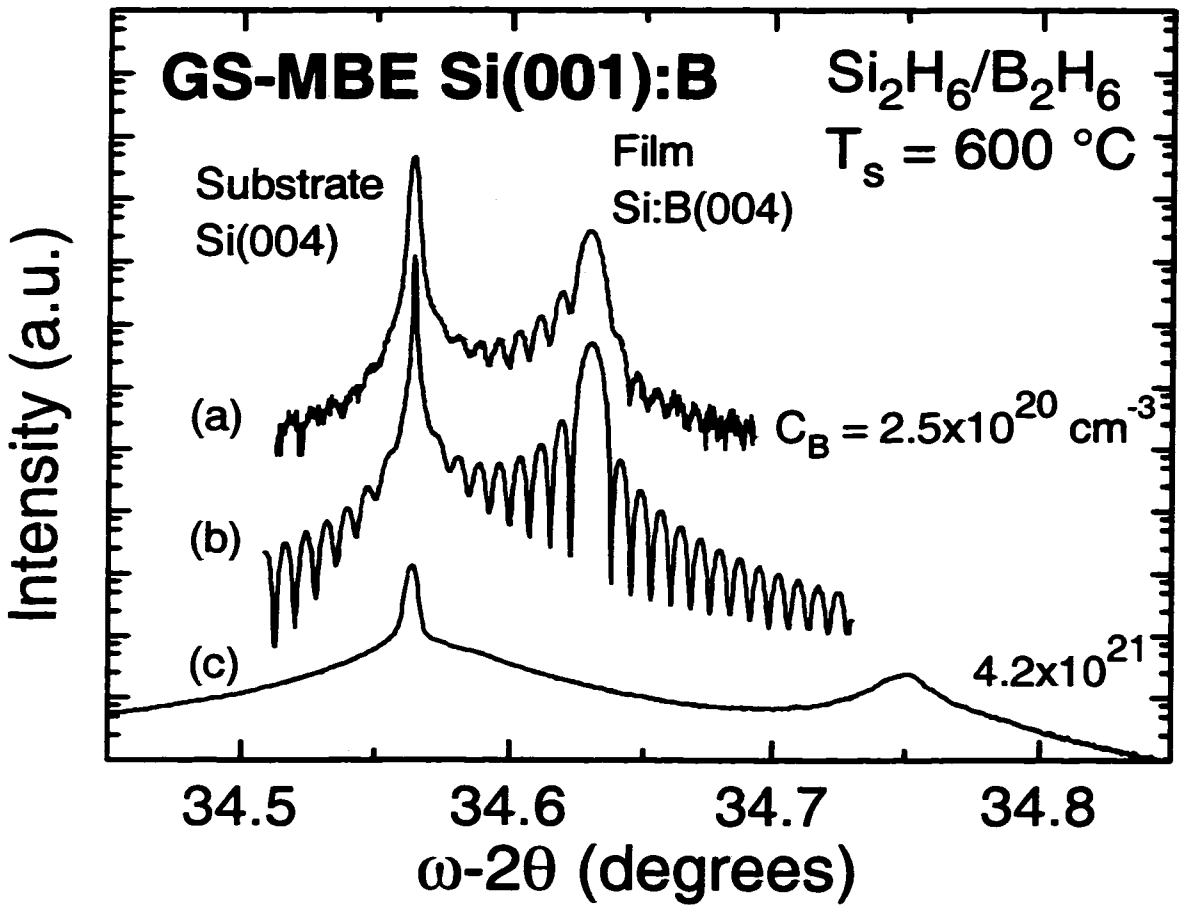

Figure 5.11. High-resolution x-ray diffraction 004 ω–2θ scans from: (a) GS-MBE Si(001):B layer grown at $T_s = 600$ °C with a B concentration $C_B = 2.5x10^{20}$ cm^{-3}; (b) fully dynamical simulation assuming $C_B = 2.5x10^{20}$ cm^{-3}, no strain relaxation, and perfectly uniform flat lattice planes; and (c) GS-MBE Si(001):B layer grown at $T_s = 600$ °C with $C_B = 4.2x10^{21}$ cm^{-3}.

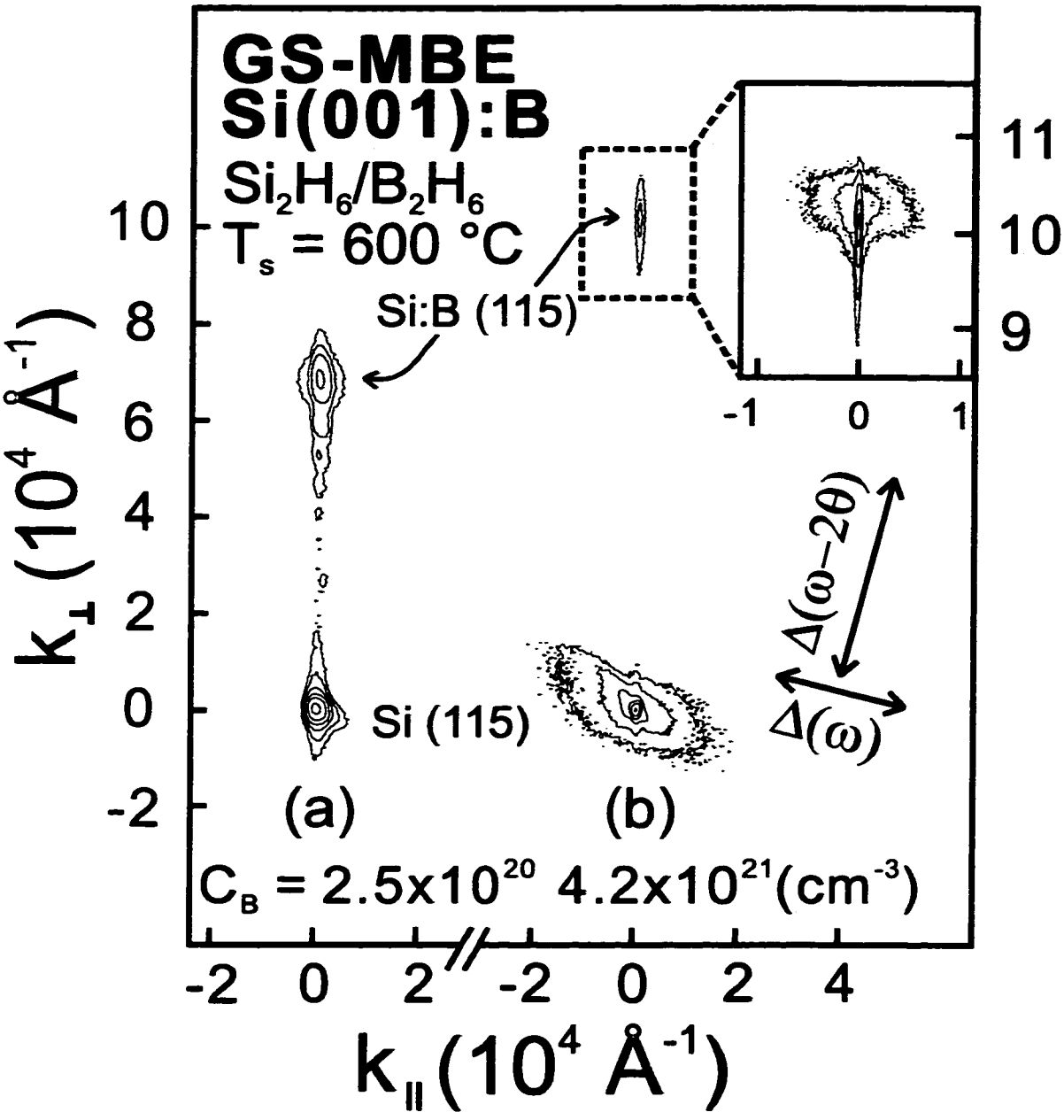

Figure 5.12. High-resolution 115 reciprocal space maps from Si(001):B layers with B concentrations C_B of (a) 2.5×10^{20} cm^{-3} and (b) 4.2×10^{21} cm^{-3}. Successive isointensity contours correspond to 22000, 5000, 500, 80, 30, and 10 counts s^{-1}. The inset shows a detailed view of the layer peak in (b) with isointensity contours corresponding to 80, 45, 23, 7, and 2 counts s^{-1}.

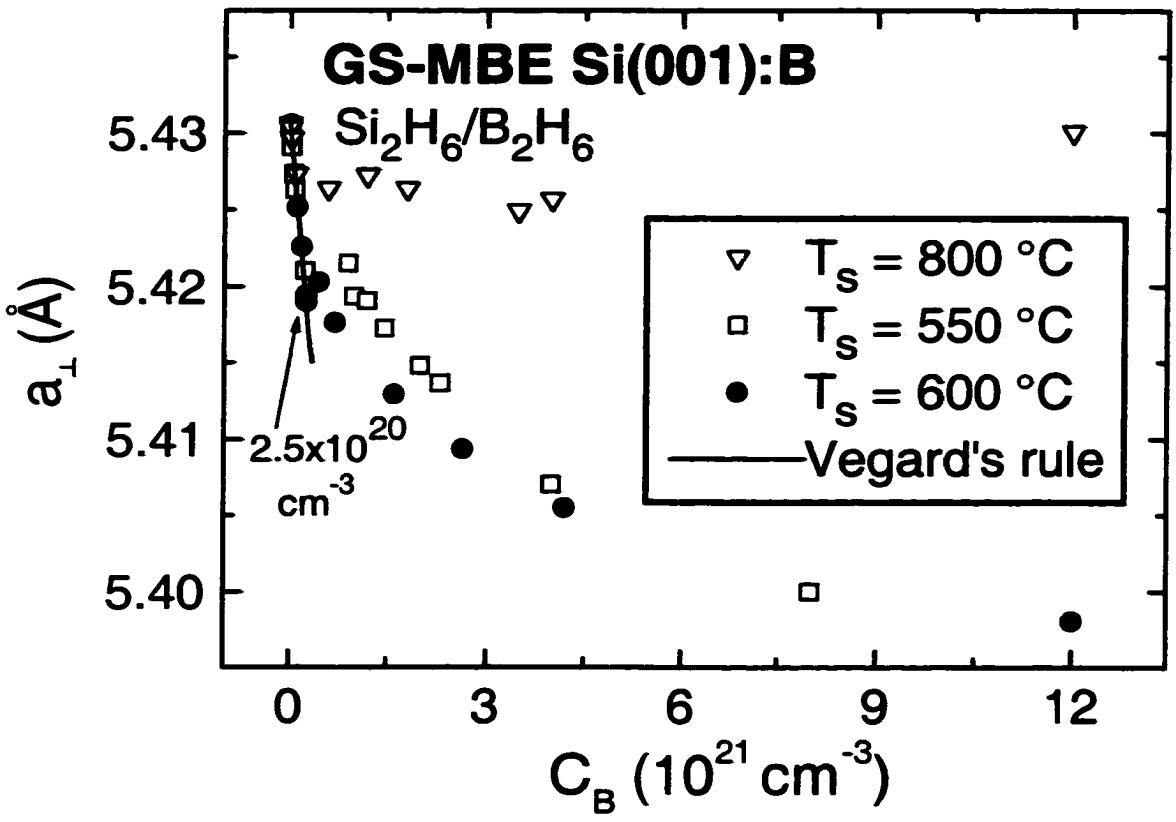

Figure 5.13. The lattice constant $a_\perp$ along the growth direction as a function of B concentration C_B for GS-MBE Si(001):B layers grown from B_2H_6/Si_2H_6 mixtures at T_s = 550, 600, and 800 °C. The solid line shows Vegard's rule based upon a linear interpolation of diamond cubic Si and B lattice constants.

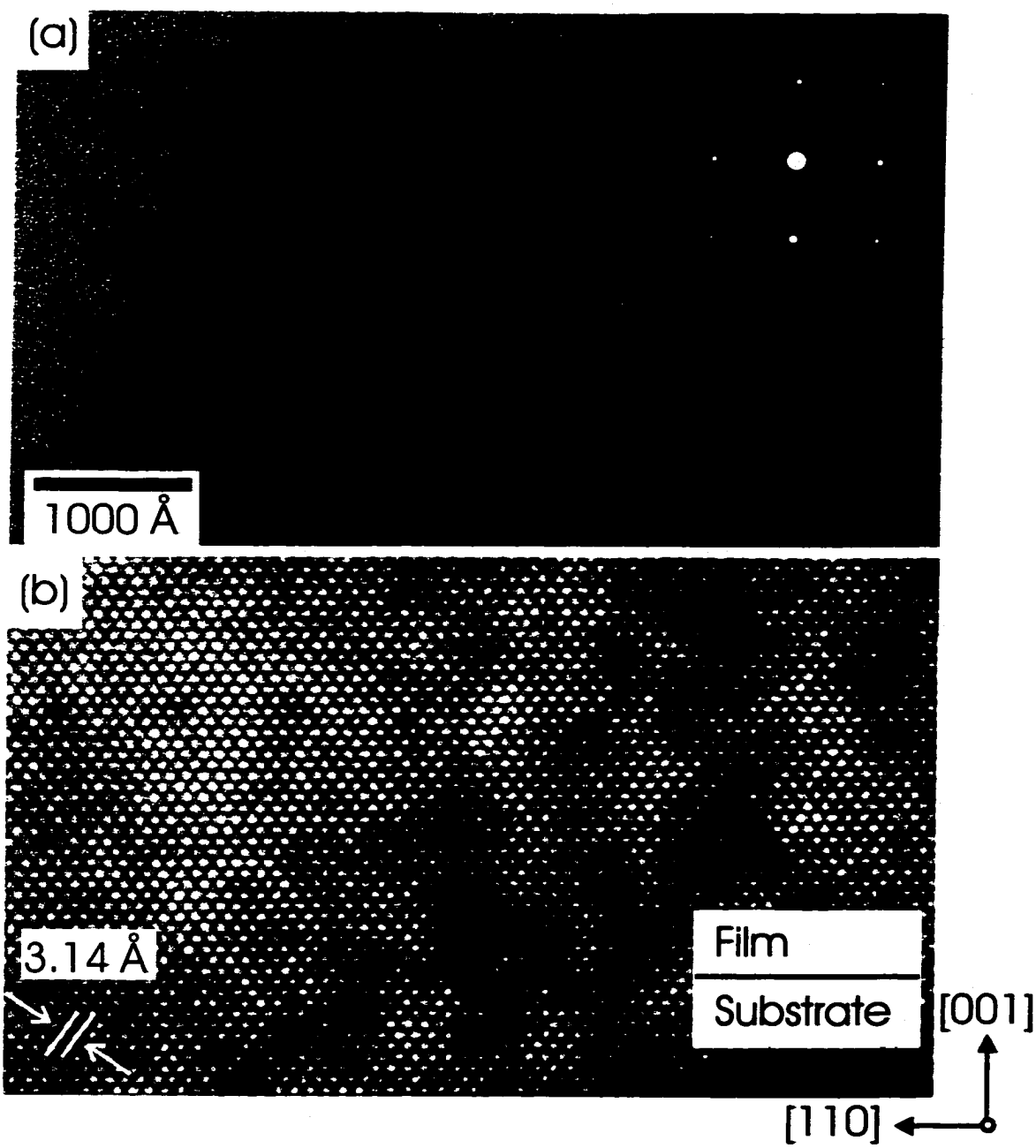

Figure 5.14. (a) Plan-view 001 zone axis TEM micrograph of a GS-MBE Si(001):B layer with B concentration $C_B = 1x10^{20}$ cm^{-3} grown from Si_2H_6/B_2H_6 mixtures at $T_s = 600$ °C. The inset is a 001 selected-area electron diffraction pattern. (b) High-resolution XTEM micrograph from a GS-MBE Si(001):B layer grown at $T_s = 600$ °C with $C_B = 2.5x10^{20}$ cm^{-3}.

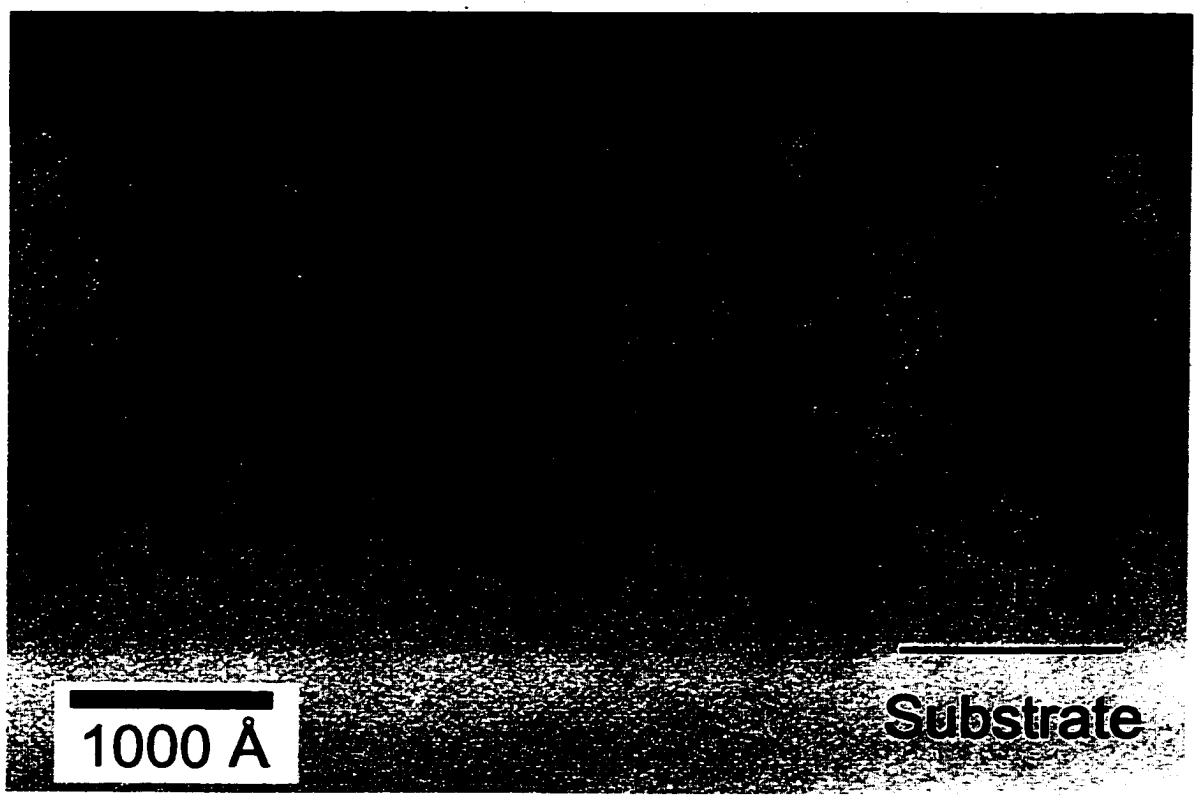

Figure 5.15. Dark-field 011 XTEM micrograph, obtained using the 004 reflection, of a B-doped GS-MBE Si(001) layer grown at $T_s = 600$ °C with $C_B = 3x10^{21}$ cm^{-3}.

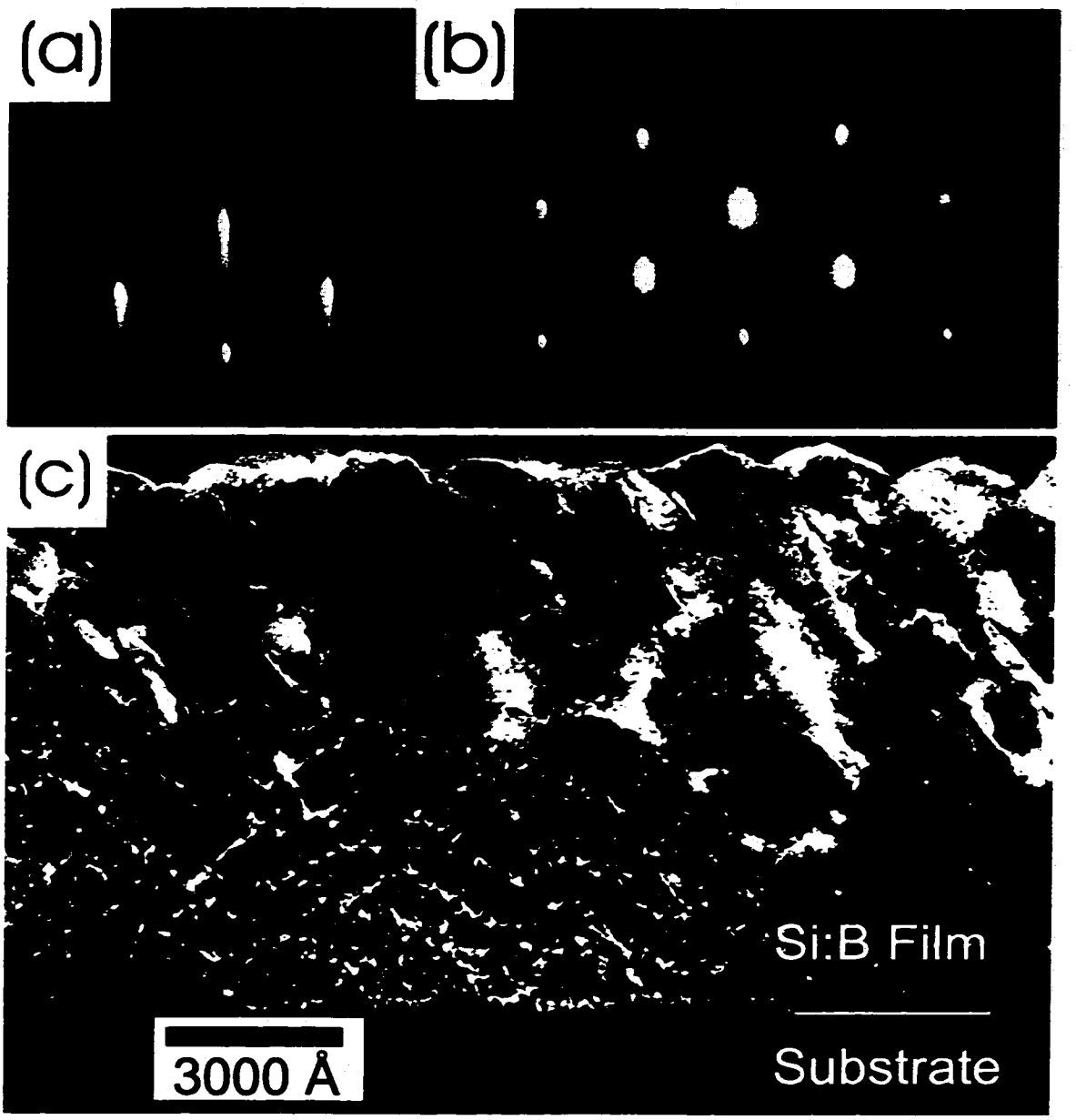

Figure 5.16. RHEED patterns from GS-MBE Si(001):B layers grown at $T_s = 800$ °C with B concentrations C_B of (a) $3x10^{20}$ cm^{-3} and (b) $3x10^{21}$ cm^{-3}. (c) Dark-field 011 XTEM micrograph, acquired using the 004 reflection, of a B-doped GS-MBE Si(001) layer grown at $T_s = 800$ °C with $C_B = 3x10^{21}$ cm^{-3}.

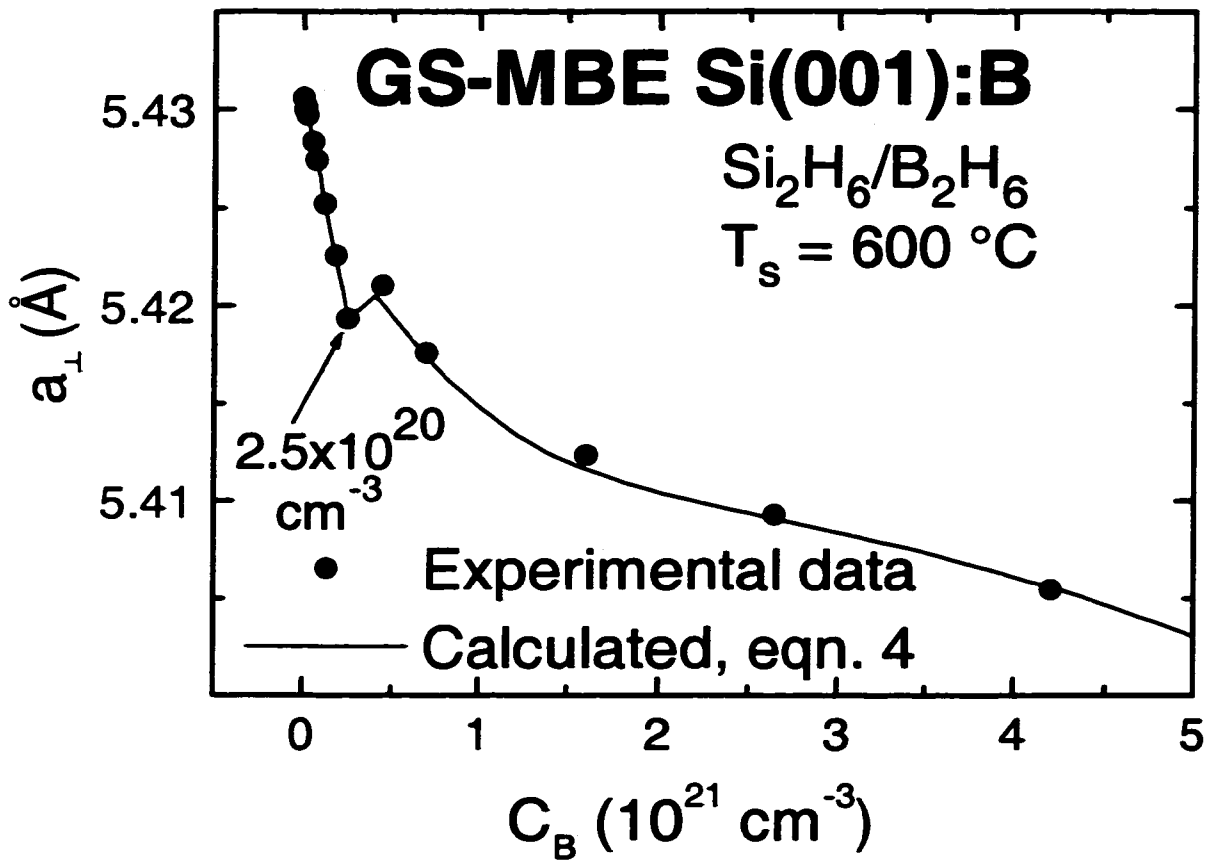

Figure 5.17. The lattice constant $a_\perp$ along the growth direction as a function of B concentration C_B in GS-MBE Si(001):B layers grown from Si_2H_6/B_2H_6 mixtures at $T_s = 600$ °C. The solid line was calculated using equation 5.4.

CHAPTER 6. Electrically active and inactive B lattice sites in ultra-highly B doped Si(001): An x-ray near-edge absorption fine-structure spectroscopy study

6.1. Introduction

In Chapter 5, I presented the first experimental evidence, obtained using high-resolution x-ray diffraction (HR-XRD), Hall-effect, and SIMS measurements for the incorporation of B pairs into substitutional Si sites. This occurs during GS-MBE growth when C_B exceeds $2.5x10^{20}$ cm^{-3}. The B pairs are electrically inactive as shown by temperature-dependent Hall measurements. In this chapter, I use the technique of near-edge x-ray absorption spectroscopy to probe the bonding of the electrically inactive B atoms.

6.2. Results

Si(001):B layers, as presented in Chapter 5 with C_B ranging from $5x10^{16}$ to $1.2x10^{2}$ cm^{-3} were grown in ultra-high vacuum (UHV) by GS-MBE using Si_2H_6 and B_2H_6 at temperatures T_s = 600 °C, well above the monohydride desorption temperature.[1] Typical B *K*-edge TEY and FY NEXAFS spectra, obtained with the x-ray beam incident at 20° to the sample normal, are shown in Fig. 6.1 for films with C_B values between $5x10^{18}$ and $1x10^{22}$ cm^{-3}. The 196 eV peak, corresponding to the B 1s $\rightarrow$ $2p_z$ (π^*) transition, is present for all films, but is much more pronounced in the surface sensitive TEY spectra. The broad feature at 205 eV, due to the B 1s $\rightarrow$ σ^* transition, is clearly visible in the TEY spectra. Both

peaks are assigned to B_2O_3 formed at the surface due to a combination of B segregation during film growth[1] and subsequent sample air exposure.

The NEXAFS peak located at 192 eV emerges in the layer with $C_B = 5x10^{20}$ cm^{-3} and the intensity of the peak increases sharply with further increase in C_B. This peak is much more prominent in the FY than in the TEY NEXAFS spectra. Since the effective electron escape depth for semiconductors with incident x-ray radiation in the 100–200 eV range is < 100 Å compared to a fluorescence photon escape depth of > 1000 Å,[2] the peak at 192 eV must be related to bulk rather than surface B.

6.3. Discussion

6.3.1. Electrically active and inactive B bonding environments

The 192 eV feature in Fig. 6.1 cannot be attributed to previously reported B-related species with similar peak positions: *o*-carborane ($B_{10}H_{10}C_2H_2$), diborane (B_2H_6), and decaborane ($B_{10}H_{14}$).[3] SIMS measurements show that C in our films is below the detection limit, $5x10^{16}$ cm^{-3}, while boron hydrides either dissociatively chemisorb or desorb from short-lived physisorbed states at the film growth temperatures employed. The 192 eV peak is attributed to a B 1s $\rightarrow$ $2p_z$ transition corresponding to sp^2 bonded B incorporated as B pairs located at single Si-sites (inset of Fig. 6.1). In this configuration, each B is surrounded by three atoms: two Si and one B, and has a planar trigonal coordination. The fact that this peak is at a lower energy than the sharp peak arising from surface B_2O_3 is consistent with the lower Pauling electronegativity values of Si (1.8) and B (2.0) compared to O (3.5).

The broad feature in FY spectra near 201 eV (also visible, although weaker, in the surface-sensitive TEY spectra) is attributed to a convolution of contributions arising from B 1s $\rightarrow$ σ^* transitions associated with sp^2 B-B and B-Si (B in the electrically-inactive configuration) bonds together with sp^3 B-Si (B in the electrically-active configuration) bonds. The individual peaks cannot be resolved.

Angle-dependent NEXAFS measurements were carried out on the Si(001):B layer with $C_B = 1.0x10^{22}$ cm^{-3}, for which the electrically inactive B concentration $(C_B-N_B) = 8.8x10^{21}$ cm^{-3} (Table 6.1), in order to determine the polarization dependence of the B 1s $\rightarrow$ $2p_z$ (π^*) signal. The angle θ between the film surface normal and the direction of the incident beam was varied between 10 and 60°. If all B pairs were oriented along the [001] growth direction, i.e. π^* orbitals oriented along [hk0] with $h,k = \pm 1$, the intensity I of the 192 eV feature should be proportional to $\cos^2\theta$. However, if the B pairs are in-plane with π^* orbitals aligned along [0kl] and [h0l] with k,l and $h,l = \pm 1$, I should be independent of θ. No strong dependence of I on θ was observed indicating that most of the B pairs are oriented in-plane. Within the resolution of the measurements, I can not, however, rule out the possibility that the B pairs are randomly oriented, with 1/3 of them along [001], which would give only a weak $I(\theta)$ dependence.

Based upon the above results, I propose the following reaction paths for B incorporation in ultra-high doped GS-MBE Si(001):B layers. During Si(001):B film growth at $C_B \leq 2.5x10^{20}$ cm^{-3}, C_B increases linearly with the B_2H_6/Si_2H_6 flux ratio and incorporated B segregates to the second layer[4] with a coverage $\theta_B \leq \theta_{B,sat} = 0.5$ ML, the saturation value.[1,4] All B incorporated in these layers is located at tetrahedrally-coordinated substitutional Si sites

and is electrically active. As a result, $a_{\perp}$ for these films decreases linearly with increasing C_B and the 192 eV NEXAFS peak is absent.

6.3. Inactive B incorporation mechanism

When C_B exceeds $2.5x10^{20}$ cm^{-3}, the B incorporation rate increases (i.e. C_B increases with B_2H_6/Si_2H_6 flux ratio at a faster rate), $\theta_B > \theta_{B,sat}$ during film growth, and, as has been recently shown by isotopically-tagged temperature-programmed desorption, B begins to accumulate at the outer surface.[1] B surface adatoms activate a parallel B_2H_6 chemisorption mode. Simultaneous with the overall increase in the B incorporation rate (see Fig. 5.2), the fraction of electrically-active B decreases from unity (Table 6.1). The increase in B incorporation probability indicates an additional source, and is due to B adsorption in the form of pairs in parallel with substitutional B incorporation. B pairs are incorporated with trigonal-symmetry on substitutional Si sites such that all B σ-bonds are saturated. Furthermore, incorporation of electrically-inactive B at the expense of active B decreases the overall tensile strain in the layer by contributing a compressive component (see Fig. 5.17).

Previous *ab-initio* calculations show that the lowest-energy configuration for B pairs in Si is for the bond direction to be along $\langle 100 \rangle$ with a B-B bond length $r_{B-B} = 1.6 \pm 0.2$ Å.[5.6] Using this result with our angle-resolved NEXAFS data which rule out the possibility that the B-B bonds are all aligned along the [001] growth direction, I calculated, based upon the experimental value of α obtained from equation 5.4 in Chapter 5 and, the bond length between a nearest-neighbor Si and a B pair atom for two cases: (1) all B pairs are aligned in-plane equally along [100] and [010] directions and (2) the pairs are distributed randomly in all three

orthogonal directions. The results yield $r_{Si-B_{pair}} = 2.18$ and 2.01 ± 0.04 Å, respectively. $r_{Si-B_{pair}}$ for case (2) agrees with total energy calculations predicting a value of 2.01 Å for randomly aligned ⟨100⟩ B pairs.[5]

6.4. Conclusions

In summary, I have shown that B in GS-MBE Si(001):B layers grown from B_2H_6/Si_2H_6 mixtures is incorporated into electrically active sp^3 bonded tetrahedral sites at concentrations N_B up to 2.5×10^{20} cm^{-3}. For layers with higher B concentrations ($C_B = 5 \times 10^{20}$-1.2×10^{22} cm^{-3}), N_B continues to increase with increasing C_B, but the electrically-active B fraction N_B/C_B decreases rapidly. Electrically-inactive B is incorporated as sp^2-bonded trigonally-coordinated B pairs in substitutional Si sites giving rise to a strong $1s \rightarrow 2p_z$ (π^*) NEXAFS feature. I propose a surface reaction path leading to B dimer incorporation which is consistent with our HR-XRD measurements. That is, when the second-layer B coverage during film growth exceeds the saturation value of 0.5 ML (corresponding to $C_B = 2.5 \times 10^{20}$ cm^{-3}), excess B accumulates at the outer surface where it activates a parallel B incorporation mode in the form of pairs on substitutional sites, thus reducing the overall in-plane tensile strain.

6.5 References

1. H. Kim, G. Glass, T. Spila, N. Taylor, S.Y. Park, J.R. Abelson, and J.E. Greene, J. Appl. Phys. **82**, 2288 (1997); G. Glass, H. Kim, M.R. Sardela, Q. Lu, J.R.A. Carlsson, J.R. Abelson, and J.E. Greene, Surf. Sci. **392**, L63 (1997).
2. M. Kasrai, Z. Yin, G.M. Bancroft, and K.H. Tan, J. Vac. Sci. Technol. A **11** 2694 (1993).
3. M.W. Ruckman, M.F. Murray, J.K. Mowlem, and D.R. Strongin, J. Vac. Sci. Technol. A **11**, 2477 (1993).

4. Y. Wang, R.J. Hamers, and E. Kaxiras, Phys. Rev. Lett. **74**, 403 (1995).
5. E. Tarnow, J. Phys. Condens. Matter **4**, 5405 (1992).
6. J. Zhu, T. Diaz dela Rubia, L. H. Yang, C. Mailhiot, and G.H. Gilmer, Phys. Rev. B **54**, 4741 (1996).

Table 6.1. Total (C_B), electrically-active (N_B), and inactive B concentrations in B-doped Si(001) layers.

Total B concentration C_B (cm^{-3})	**Active B concentration N_B (cm^{-3})**	**Inactive B concentration (C_B–N_B) (cm^{-3})**
$5.0x10^{18}$	$5.0x10^{18}$	–
$1.7x10^{20}$	$1.7x10^{20}$	–
$2.5x10^{20}$	$2.5x10^{20}$	–
$4.5x10^{20}$	$2.3x10^{20}$	$2.2x10^{20}$
$5.0x10^{20}$	$2.5x10^{20}$	$2.5x10^{20}$
$7.0x10^{20}$	$3.0x10^{20}$	$4.0x10^{20}$
$1.6x10^{21}$	$4.8x10^{20}$	$1.1x10^{21}$
$2.7x10^{21}$	$6.5x10^{20}$	$2.1x10^{21}$
$4.2x10^{21}$	$7.8x10^{20}$	$3.4x10^{21}$
$6.0x10^{21}$	$9.0x10^{20}$	$5.1x10^{21}$
$1.0x10^{22}$	$1.2x10^{21}$	$8.8x10^{21}$
$1.2x10^{22}$	$1.3x10^{21}$	$1.1x10^{22}$

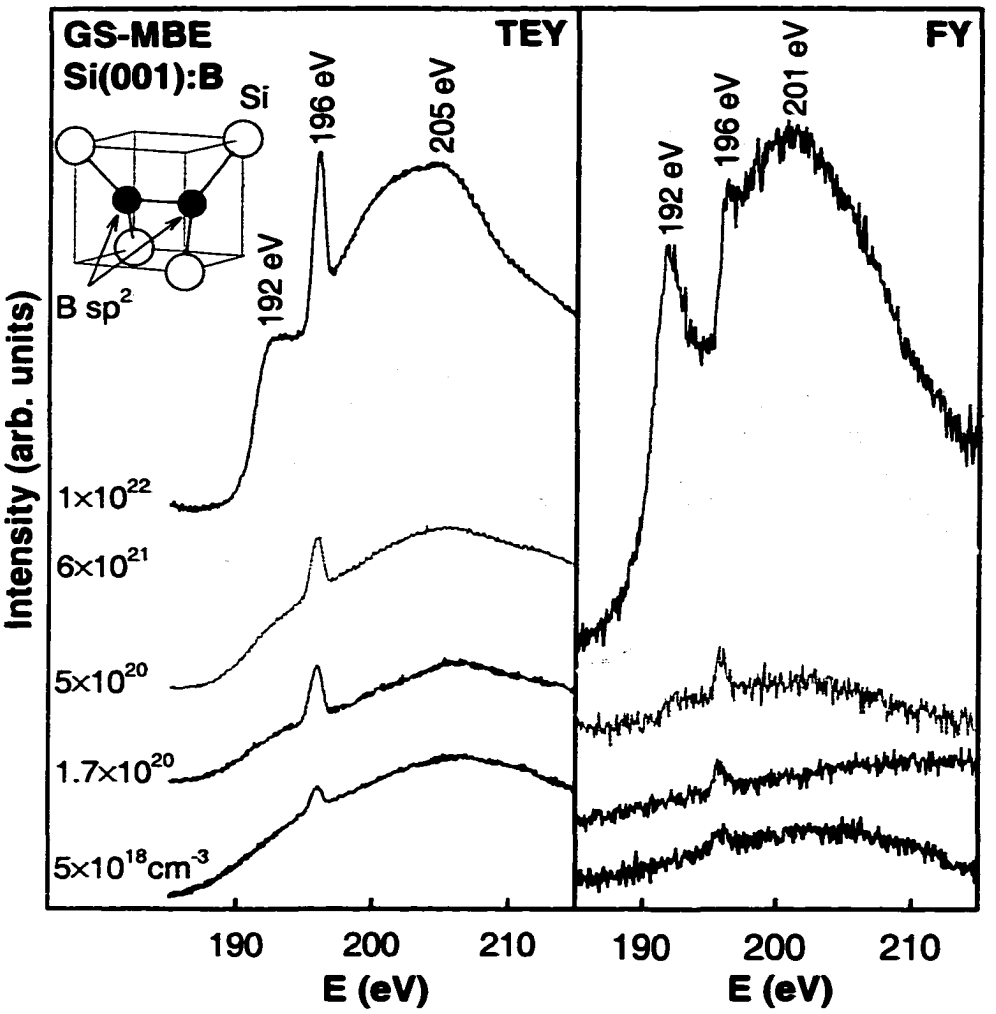

Figure 6.1. (a) Total electron yield (TEY) and (b) fluorescence yield (FY) NEXAFS spectra obtained near the B *K*-edge of GS-MBE Si(001):B layers with C_B ranging from $5.0x10^{18}$ to $1.0x10^{22}$ cm^{-3}. The inset shows a B pair incorporated into electrically-inactive sp^2 bonded trigonally-coordinated substitutional sites in a Si tetrahedron.

CHAPTER 7. Ultra-highly doped $Si_{1-x}Ge_x(001)$:B gas-source molecular beam epitaxy: Boron surface segregation and its effect on film growth kinetics

7.1. Introduction

Results of an investigation using D_2 TPD to determine B and H steady-state surface coverages (θ_B and θ_H) as functions of B concentration C_B, and the substrate temperature T_s during GS-MBE growth of Si(001):B from Si_2H_6/B_2H_6 gas mixtures were presented in Chapter 4. Our group has also used D_2 temperature-programmed desorption (TPD) to determine B, Ge, and H steady-state surface coverages (θ_B, θ_{Ge}, and θ_H) as functions of B concentration C_B, x, and temperature T_s during GS-MBE growth of Si(001):B,[1-3] Ge(001):B[4] and $Si_{1-x}Ge_x(001)$[5-7] from Si_2H_6/B_2H_6, Ge_2H_6/B_2H_6, and Si_2H_6/Ge_2H_6 mixtures, respectively. These data were provided the basis for quantitative modeling of layer growth kinetics.[2,4,5]

Combined ion channeling, cross-sectional transmission electron microscopy, and electrical measurements,[8] together with scanning electron microscopy (STM) analyses[9,10] and TPD combined with AES results,[2] have shown that trivalent B atoms deposited on Si(001) move, primarily due to their smaller size,[3] to the second atomic layer with a saturation coverage of 0.5 ML. Based upon STM results,[9,10] the primary B-induced Si(001) surface reconstruction is a c4x4 subunit containing four second-layer B atoms, two first-layer Si dimers having B backbonds, an unmodified first-layer Si dimer with Si backbonds, and a dimer vacancy.

Typical D_2 TPD spectra obtained from Si(001):B layers (see Fig. 7.1a) exhibit, in addition to β_1 and β_2 peaks due to Si 2×1 monodeuteride $^{D}\!\diagdown\!Si-Si\!\diagup^{D}$ and Si 1×1 dideuteride

$^{D}\backslash_{Si}/^{D}$ surface species, related lower-temperature B-induced β_1^* and β_2^* replica peaks associated with D_2 desorption from B-backbonded Si surface atoms, Si^*. The lower activation energies measured for D_2 desorption from Si^* atoms results from the combination of charge transfer to the B backbonds and additional local strain introduced by the second-layer B. Fig. 7.1a shows that with increasing B concentration, the intensity of the β_1^* peak increases while β_1 peak decreases. Fitting the four TPD peaks and comparing the results to previous measurements on Si(001) wafers dosed with known B coverages (< 0.50 ML)[3] yields θ_B values as a function of the bulk B concentration C_B. From this, the B segregation enthalpy in Si was determined to be -0.53 eV. In addition, it was shown, in agreement with the surface structure model proposed by Wang and Hamers,[9,10] that the coverage of B-backbonded surface sites is equal to $0.5\theta_B$ for second-layer B coverages up to 0.50 ML. For GS-MBE Si layers grown at T_s = 550 °C, θ_B reaches saturation coverage, $\theta_{B,sat}$ = 0.50 ML, at $C_B = 5\times10^{20}$ cm^{-3}. With higher B concentrations, an additional TPD peak is observed at low temperature due to the presence of surface B-H bonds, indicating that B segregates to the outer surface when θ_B exceeds $\theta_{B,sat}$. A similar analysis was used to explain the evolution of Ge monodeuteride TPD spectra obtained from Ge(001):B layers as a function of C_B (see Fig. 7.1b).[4] The segregation enthalpy for B in Ge(001) layers was determined to be -0.64 eV.[4]

The spectra presented in Figs. 7.1a and 7.1b show that saturation deuterium coverages $\theta_{D,sat}$, corresponding to the total area under the TPD envelope function, decrease with increasing B concentration. This is caused by two primary factors. The first is simply the fact that the Si (Ge) dimer vacancy population increases in direct proportion to θ_B. This effect is exacerbated, however, by the partial deactivation of B-backbonded Si^* (Ge^*) dangling-bonds due to charge transfer from Si^* (Ge^*) adatoms to second-layer B. The Si-B (Ge-B) bond length, 2.0-2.1 Å[11] (2.1-2.2 Å)[12] is considerably shorter than Si-Si, 2.35 Å (Ge-Ge, 2.45 Å), and B has both a higher electronegativity than Si (Ge) and an empty sp^3 orbital. Using

measured β_1 and β_1^* (α_1 and α_1^*) integrated TPD peak intensities from bulk Si(001) (Ge(001)) wafers with known B coverages,[3,4] we have shown previously that approximately one dangling bond per Si* (Ge*) dimer is deactivated. These results were incorporated into a predictive model for the growth rates R of GS-MBE Si(001):B and Ge(001):B as a function of the precursor fluxes $J_{Si_2H_6}$, $J_{Ge_2H_6}$, and $J_{B_2H_6}$ and the growth temperature T_s. With constant $J_{Si_2H_6}$, R_{Si} increases by up to 50% with increasing $C_B > 10^{19}$ cm^{-3} at $T_s \leq 550$ °C, while it decreases by an equivalent amount at $T_s \geq 600$ °C.[2] Similar effects were observed for Ge(001):B GS-MBE.[4] Calculated $R(C_B,T_s)$ curves, based upon the TPD results, exhibit good agreement with deposition rate data.[2,4]

Isotopically-tagged *in-situ* D_2 TPD was also used to probe Ge segregation and H desorption pathways during $Si_{1-x}Ge_x(001)$ GS-MBE.[5-7] TPD spectra in Fig. 7.1c contain β_1, β_1', β_2, α_1 and α_2 peaks due to Si 2×1 monodeuteride, mixed Si-Ge dimer 2×1 monodeuteride $^{D}\backslash Si-Ge/^{D}$, Si 1×1 dideuteride, Ge 2×1 monodeuteride $^{D}\backslash Ge-Ge/^{D}$, and Ge 1×1 dideuteride $^{D}\backslash Ge/^{D}$ surface species. The monodeuteride binding energies E_{Si} at Si sites and E_{Ge} at Ge sites both decrease linearly with increasing Ge surface coverage θ_{Ge}. At all Ge coverages, however, E_{Si} is much larger than E_{Ge} and, hence, the steady-state H coverage θ_H on Si sites far exceeds that on Ge. That is, Si sites act as effective traps for D atoms, due to their higher binding energy, and limit the overall H_2 desorption rate during steady-state $Si_{1-x}Ge_x(001)$ growth.[7] The overall dangling-bond density, as measured by the saturation deuterium coverage $\theta_{D,sat}$ is independent of x.[7] Calculated values, based upon the above results, for film growth rates R_{SiGe} and composition x as a function of the precursor fluxes $J_{Si_2H_6}$ and $J_{Ge_2H_6}$ and the growth temperature T_s agree with experimental measurements.[5-7]

In this article, we present the results of experiments utilizing *in-situ* D_2 TPD to determine θ_B, θ_{Ge}, and θ_D as a function of C_B (2×10^{16}-2×10^{21} cm^{-3}) and T_s during GS-MBE $Si_{0.82}Ge_{0.18}(001)$:B growth at T_s = 500-700 °C. TPD spectra from GS-MBE $Si_{0.82}Ge_{0.18}(001)$:B layers contain β_1, β_1', β_2, α_1 and α_2 peaks together with B-induced β_1^*, $\beta_1'^*$, α_1^*, β_2^*, and α_2^*

replica peaks associated with D-bonded Si^* and Ge^* surface atoms with B backbonds. B concentrations in as-deposited $Si_{0.82}Ge_{0.18}(001)$:B layers increase linearly with incident flux ratio $\xi = J_{B_2H_6}/(J_{Si_2H_6} + J_{Ge_2H_6}) \leq 0.3$ for C_B values $\leq 4.6\times10^{20}$ cm^{-3}. At higher ξ, corresponding to $\theta_B > \theta_{B,sat}$, the B incorporation probability increases by up to a factor of 2.5.

For $Si_{0.82}Ge_{0.18}$ layers grown at T_s = 500 °C, θ_{Ge} is 0.63 ML, independent of C_B, while θ_B increases from 0.03 ML with $C_B = 3\times10^{18}$ cm^{-3} to $\theta_{B,sat}$ = 0.5 ML with C_B near 5×10^{20} cm^{-3}. The B segregation enthalpy decreases from -0.53 and -0.64 eV in Si(001) and Ge(001) layers, respectively, to -0.42 eV in $Si_{0.82}Ge_{0.18}(001)$. Measured segregation ratios $r_B = \theta_B/x_B$, where x_B is the bulk B concentration fraction in $Si_{0.82}Ge_{0.18}$, range up to 500. We show that the temperature dependence of B segregation is consistent with equilibrium segregation. A decrease in $R_{SiGe}(C_B)$ by up to a factor of two for $C_B > 10^{19}$ cm^{-3} is predicted, based upon the TPD results, and calculations exhibit good agreement with deposition rate data.

7.2. Experimental results

7.2.1. B incorporation during $Si_{0.82}Ge_{0.18}(001)$:B GS-MBE

Doped $Si_{0.82}Ge_{0.18}(001)$ layers, 0.1-0.3 μm thick, were grown at T_s = 500-700 °C with B concentrations C_B ranging from 2×10^{16} to 2×10^{21} cm^{-3}. The Si_2H_6 and Ge_2H_6 fluxes were maintained constant at $J_{Si_2H_6} = 2.2\times10^{16}$ and $J_{Ge_2H_6} = 6.6\times10^{14}$ $cm^{-2}s^{-1}$, respectively, while the incident B_2H_6 flux was varied from $J_{B_2H_6} = 5.3\times10^{11}$ to 2.2×10^{16} $cm^{-2}s^{-1}$ corresponding to incident precursor flux ratios $\xi = J_{B_2H_6}/(J_{Si_2H_6} + J_{Ge_2H_6})$ between 2×10^{-5} and 1. The primary growth temperature used in these experiments, T_s = 500 °C, was chosen to minimize film roughening, especially at high B doping concentrations, while maintaining an acceptable growth rate, ≈ 0.2 μm h^{-1} for undoped $Si_{0.82}Ge_{0.18}(001)$.[6] Higher temperature growths were also carried out in order to verify that $Si_{1-x}Ge_x$ growth T_s = 500 °C corresponds to the equilibrium segregation regime for both B and Ge.

Typical zero-order Laue-zone RHEED patterns are shown in Fig. 7.2. For $C_B < 1\times10^{20}$

cm^{-3}, the RHEED patterns are similar to those from undoped $Si_{0.82}Ge_{0.18}$ layers and exhibit ordered 2×8 surface superstructures due to dimer-row vacancies.[6] The RHEED patterns consist of well-defined diffraction spots, rather than streaks, with sharp Kikuchi lines, and essentially equi-intense fundamental and half-order reflections as shown in Fig. 7.2a from a film with $C_B = 5\times10^{19}$ cm^{-3}. Layer surfaces were thus atomically smooth with relatively large terraces. At $C_B > 10^{20}$ cm^{-3}, the reflections become streaky as illustrated by the example in Fig. 7.2b from a film with $C_B = 1.5\times10^{21}$ cm^{-3}. With increasing B concentration in this range, the fundamental rods broaden, the ratio of the half-order to fundamental rod intensity decreases, and the amount of diffuse scattering increases; all are indicative of increased atomic-scale surface roughening. Nonetheless, all surfaces exhibited 2-dimensional patterns, with no evidence of facetting or substantial three-dimensional roughening.

The total incorporated B concentration, as measured by SIMS, increased linearly with ξ for flux ratios up to ≈ 0.3, for which $C_B = 5\times10^{20}$ cm^{-3} as shown in Fig. 7.3. The solid line in Fig. 7.3 was calculated using the procedure outlined in section 7.3.4. and agrees well with experimental data throughout the linear B incorporation range. At higher flux ratios, C_B exceeds calculated values by a factor of two. This behavior is similar to recent observations in ultra-highly doped Si(001):B[11] and Ge(001):B[13] GS-MBE for which the linear region corresponds to B incorporation in electrically-active sites, while the break in linearity occurred when $\theta_B > \theta_{B,sat}$ giving rise to the incorporation of electrically inactive trigonally bonded B pairs on substitutional lattice sites.[24] A comparison of C_B values obtained from SIMS, together with resistivity and Hall effect measurements, showed that B was incorporated into substitutional electrically active sites at concentrations $\lesssim 5\times10^{20}$ cm^{-3}.

Fig. 7.4 is a plot of the $Si_{0.82}Ge_{0.18}$(001):B growth rate R_{SiGe} as a function C_B. R_{SiGe} remains constant with increasing B concentrations up to $\approx 10^{19}$ cm^{-3}. At higher B doping levels, however, R_{SiGe} gradually decreases by more than a factor of two. The fact that B, present at concentrations in the part per thousand range, can have such a pronounced effect on

growth kinetics is a clear signature of B surface segregation during layer growth. Analyses of TPD data in sections 7.3.1 and 7.3.2 show that this behavior is due primarily to a second-layer B-backbond induced reduction in the Si and Ge adatom dangling-bond densities and, hence, in the number of sites available for precursor adsorption.

A series of modulation-doped structures were grown in order to determine whether B incorporation during $Si_{1-x}Ge_x(001)$ GS-MBE affects the Ge concentration. In all cases, an undoped $Si_{0.82}Ge_{0.18}(001)$ layer with a thickness of $\simeq$ 600 Å was deposited initially, then without shutting off the Si_2H_6 and Ge_2H_6 fluxes, B_2H_6 was added to the precursor gas stream and a B-doped overlayer was grown. The undoped layer serves as an internal Ge concentration reference during the SIMS measurement.

A typical SIMS profile through a doped/undoped bilayer is presented in Fig. 7.5. Upon initiation of $Si_{1-x}Ge_x$ growth, Ge segregates to the film surface leaving a Ge-depleted region near the film/substrate interface.[5-7] However, once a steady-state bulk alloy concentration is reached ($\simeq$ 100 Å), the Ge concentration in the undoped and doped regions are identical. This was true for all B concentrations investigated, $C_B \leq 2\times10^{21}$. Thus, the Si_2H_6 and Ge_2H_6 reactive sticking probabilities are not strongly dependent on C_B. This is consistent with results for ultra-highly doped Si(001):B and Ge(001):B growth.[2,4,13] Additional corroboration is provided by *in-situ* AES analyses showing that the Ge KLL (1147 eV) to Si LMM (92 eV) and Ge KLL to Si KLL (1600 eV) peak-to-peak intensity ratios obtained from as-deposited $Si_{1-x}Ge_x(001)$:B layers are independent of C_B (see Fig. 7.6). RBS measurements also show that the Ge composition of $Si_{1-x}Ge_x(001)$:B GS-MBE layers is not a function of C_B.

7.2.2. $Si_{0.82}Ge_{0.18}(001)$:B layer microstructure

Fig. 7.7 is a typical high-resolution reciprocal lattice map around the asymmetric 115 Bragg reflection from a 1500-Å-thick $Si_{0.82}Ge_{0.18}(001)$:B layer with $C_B = 1.8\times10^{20}$ cm^{-3}. Diffracted intensity distributions are plotted as isointensity contours as a function of the reciprocal lattice wavevectors $k_{\parallel}$ and $k_{\perp}$. For all samples, including the ultra-highly doped film

shown here, the substrate and film scattering distributions are nearly perfectly aligned in the $k_{\|}$ direction indicating negligible in-plane strain relaxation. From high-precision measurements, the degree of strain relaxation is $< 1x10^{-4}$ for all samples. This is close to the detection limit of the instrument, $2x10^{-5}$. Thus, the in-plane SiGe(001):B lattice constants $a_{\|} = 5.4310 \pm 0.0002$ Å are equal to that of bulk Si. The vertical separation between the film and substrate diffracted intensity distributions increases with C_B giving rise to a tetragonal distortion

The microstructures of fully-strained GS-MBE $Si_{0.82}Ge_{0.18}$(001):B films were found, as judged by TEM and XTEM analyses, to be highly perfect. Typical XTEM and high-resolution XTEM (HR-XTEM) results, in this case from a 2000-Å-thick $Si_{0.82}Ge_{0.18}$ layer with $C_B = 2x10^{20}$ cm^{-3} grown at $T_s = 500$ °C, are shown in Fig. 7.8. The bright-field XTEM micrograph in Fig. 7.8a, obtained under two-beam diffraction conditions using an 004 diffraction vector near the [110] zone axis, is essentially featureless with the exception of the lattice-mismatch strain contrast which is clearly visible at the interface. There is no evidence of extended defects and the film surface is flat to within the resolution of the micrograph. The 110 selected-area diffraction pattern shown as an insert in Fig. 7.8a consists of single-crystal reflections with uniform symmetric intensities. Fig. 7.8b is a 110 HR-XTEM image showing 111 lattice fringes which are continuous across the film/substrate interface.

7.2.3. TPD spectra from $Si_{0.82}Ge_{0.18}$(001):B

Typical D_2 TPD spectra from B-doped $Si_{0.82}Ge_{0.18}$(001) films are reproduced in Fig. 7.9. Spectra acquired from $Si_{0.82}Ge_{0.18}$(001) layers with $C_B = 0$, $3.1x10^{18}$, $4.2x10^{19}$, $2.4x10^{20}$ and $1.5x10^{21}$ cm^{-3} are shown to illustrate the primary trends as a function of C_B. With $C_B \lesssim 1x10^{19}$ cm^{-3}, the spectra are essentially identical to those obtained from undoped $Si_{0.82}Ge_{0.18}$(001) layers (see Fig. 7.1c) indicating that θ_B is small ($\theta_B \lesssim 0.05$ ML) over this B concentration range. The spectrum is composed of four second-order desorption peaks:[5-7] β_1 (peak temperature $T_p = 455$ °C, D_2 desorption energy $E_d = 2.32$ eV) assigned to the Si 2×1 monodeuteride phase, β_1' ($T_p = 430$ °C, $E_d = 2.23$ eV) from the Si-Ge mixed-dimer 2×1

monodeuteride phase, β_2 ($T_p = 365$ °C, $E_d = 1.95$ eV) from the Si 1×1 dideuteride phase, and α_1 ($T_p = 330$ °C, $E_d = 1.85$ eV) from the Ge 2×1 monodeuteride phase. θ_{Ge}, following the procedure in ref. 5, was determined from the total integrated intensity of the Ge monohydride peaks (i.e. the sum of the α_1 plus half of the β_1' peak intensities) to be 0.63 ML.

The TPD spectra change dramatically as a function of C_B at higher B concentrations. The intensity of the Si β_1 and Ge α_1 monodeuteride desorption features decrease and new features emerge. This trend is analogous to that observed for ultra-highly B-doped Si(001)[2] and Ge(001)[4] layers. The D_2 desorption onset temperature is reduced, the desorption features are broadened indicative of the presence of lower energy B-induced replica peaks, and the total integrated area under the peaks decreases indicating a corresponding decrease in the surface dangling-bond coverage.

While the overall changes observed in the TPD spectra indicate strong B surface segregation during GS-MBE $Si_{0.82}Ge_{0.18}$(001):B film growth, the peak positions corresponding to D_2 desorption from the three non-B-backbonded $Si_{0.82}Ge_{0.18}$ surface monohydride phases remain unchanged signaling the fact that their desorption energies remain constant. This is again consistent with θ_{Ge} not being function of C_B. Thus, we attribute the decrease in R_{SiGe} with increasing $C_B > 10^{19}$ cm^{-3} to a B-segregation-induced decrease in the steady-state dangling-bond density and, hence, in the precursor adsorption rates. In order to quantify these effects and deduce the reaction path, we carry out deconvolution of the TPD spectra in the following section.

7.3 Discussion

Detailed plan-view and cross sectional TEM analyses, including high-resolution, were carried out on representative samples spanning the entire B concentration range investigated. Consistent with HR-XRD results, there was no evidence of precipitates or misfit dislocations in any sample.

7.3.1 TPD deconvolution

Si, Ge, B, and H coverages were determined as a function of C_B during steady-state $Si_{0.82}Ge_{0.18}(001)$:B layer growth by analysis of deconvolved TPD spectra acquired following the procedure used for undoped $Si_{1-x}Ge_x(001)$ layers.[5-7] TPD spectra from GS-MBE Si(001):B,[1,2] Ge(001):B[4] and $Si_{1-x}Ge_x(001)$[5-7] layers exhibited up to four peaks with widths of ≃ 75 °C over a span of ≃ 200 °C. Individual peaks were always well resolved, and unique deconvolutions were obtained. In the present case, however, the large number of partially overlapping peaks greatly increases the difficulty of obtaining a unique solution. Thus, to proceed, we use our previous results for the D_2 desorption energies from Si(001):B,[1,2] Ge(001):B[4] and $Si_{0.82}Ge_{0.18}(001)$[5-7] layers as discussed below.

Increasing C_B during growth of $Si_{0.82}Ge_{0.18}(001)$:B at T_s = 500 °C has no measurable effect on either θ_{Ge} or the positions of the D_2 TPD peaks from Si(001) and Ge(001).[2,4] The only effect on TPD spectra due to the corresponding increase in the second-layer B coverage is the creation of new B-backbonded Si and Ge peaks. Thus, while we expect D_2 desorption energies from non-B-backbonded surface species during $Si_{1-x}Ge_x$ growth at constant x to also be independent of C_B, we expect ultra-high B doping to lead to the addition of B-induced replica peaks at lower energies from B-backbonded Si^* and Ge^* surface sites. For Si(001), the ratio of D_2 desorption energies from non-B-backbonded species to those from B-backbonded species is 1.1 for both the mono- and dideuteride phases.[1,2] The equivalent ratios are 1.04 for Ge monodeuteride, and 1.09 for Ge dideuteride.[4] In the case of the Si-Ge mixed-dimer monodeuteride surface phase, we note that the β_1' peak is closest in desorption energy to the β_1 peak and we thus assume a ratio of 1.1. Finally, D_2 desorption from outer surface B atoms occurs when $\theta_B > \theta_{B,sat}$ with an activation energy = 1.76 eV.[2] This D_2 desorption peak overlaps with the α_2 (Ge dideuteride) peak, such that desorption contributions from the two species remain convoluted. However, we only use the monodeuteride peaks to determine surface coverages.[1-7] The complete set of D_2 binding energies to all phases of all species

present during $Si_{0.82}Ge_{0.18}$(001):B growth are listed in Table 7.1.

Fig. 7.10 shows four typical deconvoluted TPD spectra from epitaxial $Si_{0.82}Ge_{0.18}$(001):B layers with C_B ranging from 1×10^{18} to 1.5×10^{21} cm^{-3}. All TPD spectra were fit using standard Polanyi-Wigner analyses in which the desorption rate $d\theta_D/dT$ is expressed as[14]

$$\frac{d\theta_D}{dT} = \left(\frac{\nu\theta_D^n}{\zeta}\right)\exp(-E_d/kT) \tag{1}$$

where ν is the pre-exponential factor, θ_D is the instantaneous D coverage, n is the order of the desorption reaction, ζ is the sample heating rate, E_d is the desorption activation energy, and k is Boltzmann's constant. Desorption from all surface phases obeys second order kinetics during $Si_{1-x}Ge_x$(001) layer growth with $x > 0.02$.[5] At high pumping speeds,[15]

$$\theta_D(T) = \frac{\theta_o}{1+\left(\frac{\nu}{\zeta}\right)\theta_o I(T)}. \tag{2}$$

θ_o in equation (2) is the initial coverage and I(T) is given by

$$I(T) = \frac{E_d}{R}\left[\frac{e^{-\varepsilon}}{\varepsilon^2}\sum_{n=1}^{\infty}\frac{(-1)^{n+1}n!}{\varepsilon^{n-1}}\right]_{T_o}^{T} \tag{3}$$

in which $\varepsilon = E_d/kT$.

Equations 1-3 were used to fit the $Si_{0.82}Ge_{0.18}$(001):B D_2 TPD spectra in Fig. 7.10 based upon the single set of desorption activation energies listed in Table 7.1. Excellent fits were obtained for these, as well as all TPD spectra obtained from $Si_{0.82}Ge_{0.18}$(001):B layers over the entire range of C_B investigated. Deconvoluted peaks with desorption energies greater than 1.76 eV (i.e. peak temperature $T_p \gtrsim 290$ °C) are clearly resolved. These include the six monodeuteride peaks which allow extraction of quantitative values for Si, Ge, Si-Ge, Si^*, Ge^*, and Si-Ge^* dimer coverages as a function of C_B. The intensities of the two Si dideuteride peaks β_2, and β_2^* are quite small, corresponding to coverages < 0.03 ML, based on $Si_{1-x}Ge_x$(001) TPD data,[5] and can be safely ignored. The TPD feature centered at 270 °C is dominated by the α_2 peak for $C_B < 5\times10^{20}$ cm^{-3}. At higher C_B, the feature rapidly increases in

size, and is dominated by desorption from surface B-D bonds, however, these two phases are too closely spaced to be deconvolved.

In order to obtain quantitative dangling-bond densities for each surface species $\theta_{db,species}$, all monodeuteride peaks from $Si_{0.82}Ge_{0.18}$(001):B TPD spectra were integrated. All peak intensities were normalized to the Si monohydride peak intensity (1 ML) from clean deuterium-saturated Si(001) wafers, to obtain a direct measure of the dangling-bond coverage for each species. Figure 7.11 is a plot of the dangling-bond densities of Si, Ge, Si-Ge, Si^*, Ge^*, and Si-Ge^* dimer species as a function of C_B. The non-B-backbonded monodeuteride dangling-bond densities from Si, Ge, and Si-Ge species (θ_{Si^o}, θ_{Ge^o}, $\theta_{Si\text{-}Ge^o}$) decrease as shown in Fig. 7.11a, while B-backbonded monodeuteride dangling-bond densities from Si^*, Ge^*, and Si-Ge^* species (θ_{Si^*}, θ_{Ge^*}, $\theta_{Si\text{-}Ge^*}$) increase with increasing C_B as detailed in Fig. 7.11b.

The total dangling-bond density θ_{db} in each sample as a function of C_B is simply given by the sum of the individual species dangling-bond values $\theta_{db,species}$ in Figs. 7.11a and 11b corresponding to constant C_B. θ_{db} decreases with increasing C_B from 1 ML at $C_B = 0$ to 0.5 ML at $C_B = 1.5 \times 10^{21}$ cm^{-3}. This can be understood based upon previous studies of Si(001):B layers where B segregation leads to increasing coverages of the c4×4 surface phase with increasing C_B.[11,12] The area fraction of B-induced dimer vacancies increases linearly with the c4×4 area fractions. In addition, however, approximately half of the dangling-bonds associated with B-backbonded surface dimers are deactivated by charge transfer to the underlying B atoms. This phenomenon was previously observed in Si(111)$\sqrt{3}\times\sqrt{3}$ in which charge transfer was deduced from tunneling spectra.[16] The Si-B bond-length is $\simeq$ 18% shorter than Si-Si[13], and B has both a higher electronegativity than Si and an empty sp^3 orbital. In the absence of data regarding the detailed surface structure of $Si_{0.82}Ge_{0.18}$(001):B layers, we only need assume that the backbond charge transfer arguments, which were shown to be valid for Si(001) and Ge(001) surfaces[2,4] are valid in this case as well.

Following the analyses in refs. 7-13 for GS-MBE growth of Si(001):B, Ge(001):B, and $Si_{1-x}Ge_x(001)$, we attribute the decrease in the dangling-bond density on non-B-backbonded dimer species primarily to the formation of dimer vacancies associated with the development of ordered B-induced surface reconstructions. Concurrently, the dangling-bond density on B-backbonded dimer species increases at a slower rate due to the partial deactivation of Si^*, Ge^*, and $Si\text{-}Ge^*$ dangling bonds resulting from charge transfer to B backbonds.

For $C_B \leq 5\times10^{20}$ cm^{-3} (corresponding to $\theta_B < \theta_{B,sat} = 0.5$ ML as we show below) the dangling-bond density on non-B-backbonded surface atoms θ_{dbo} decreases with increasing θ_B as:

$$\theta_{dbo} = \theta_{Sio} + \theta_{Geo} + \theta_{Si\text{-}Geo} = 1 - 1.5\theta_B \text{ ML}. \quad (4)$$

Similarly, the coverage of B-backbonded surface atoms increases from 0 to 0.50. However, assuming, as in the cases of Si(001)[2] and Ge(001),[4] that approximately half of these latter dangling-bonds are deactivated, the actual B-backbonded species dangling-bond density θ_{db*} is:

$$\theta_{db*} = \theta_{Si*} + \theta_{Ge*} + \theta_{Si\text{-}Ge*} = 0.5\theta_B. \quad (5)$$

θ_B values determined from the TPD data based on equations 4 and 5 are plotted as a function of C_B in Fig. 7.12. The curve exhibits the signature shape of an equilibrium segregation process with saturation coverage of 0.5 ML equal to that observed for Si(001):B[2] and Ge(001):B[4]. Results from equations 4 and 5 agree with each other within the experimental uncertainty (10%), supporting our assumption that the B-induced surface structure in $Si_{1-x}Ge_x(001)$:B is analogous to that of Si(001):B. The inset in Fig. 7.12 shows the sum of integrated intensities of the B-backbonded and non-B-backbonded monodeuteride desorption peaks, with excellent agreement to calculated values (lines) obtained from equations 4 and 5.

7.3.2. B segregation

Gibbsian surface segregation is described by the equation[17]

$$r_B = \frac{1-\theta_B}{1-x_B}\exp\left(\frac{-\Delta H_s}{kT_s}\right), \quad (6)$$

where r_B is the steady-state ratio of the surface coverage θ_B to the bulk B fraction x_B and ΔH_s is the segregation enthalpy. Expressing θ_B in terms of C_B, and accounting for the observation that $\theta_{B,sat} = 0.5$ ML, yields

$$\theta_B = \frac{0.5C_B \exp(-\Delta H_s / kT_s)}{N_{SiGe} - C_B[1-\exp(-\Delta H_s / kT_s)]} \quad (7)$$

where N_{SiGe} is the bulk $Si_{0.82}Ge_{0.18}$ atom density, 4.9×10^{22} cm^{-3}. Equation (7) is fit to our θ_B vs C_B data, in Fig. 7.12, obtained from TPD and SIMS results presented in section 7.2. The agreement is very good using a segregation enthalpy of $\Delta H_s = -0.42\pm0.04$ eV. This is 0.11 and 0.22 eV smaller than for B in Si(001)[2] and Ge(001)[4] layers, respectively. We also plot calculated results using the segregation enthalpy for B segregation in Si(001), -0.53 eV, showing that the steady-state B coverage is very sensitive to small changes in ΔH_s.

Strain is a key driving force in the segregation of both Ge and B.[6.2] As we show above, θ_{Ge} during $Si_{0.82}Ge_{0.18}$(001):B GS-MBE at T_s = 500 °C is constant at 0.63 ML irrespective of C_B. Local strain due to surface reconstructions also results in changes in the interplanar spacings of near-surface layers.[18] In the present case with $Si_{0.82}Ge_{0.18}$(001)2×8, as with Si(001)2×1[19] and Ge(001)2×1, the surface is in tension and the spacing between the first and second atomic planes is larger than the bulk value. Angular-resolved photoemission results show that while the outer-layer of as-grown undoped $Si_{1-x}Ge_x$(001) is Ge-rich, the second-layer is Ge deficient.[18] This study shows that the average Si concentration of the second-layer is greater than the bulk composition, implying strain-driven Si segregation to the second-layer in $Si_{1-x}Ge_x$(001). For Si(001):B films, the presence of B atoms in the second-layer serves to relax the interplanar spacing toward the bulk value, hence lowering the total system free energy.[19] However, in $Si_{0.82}Ge_{0.18}$(001) films, a fraction of the second-layer strain is relaxed by the presence of Si atoms. The fact that the B segregation enthalpy is significantly lower in strained $Si_{0.82}Ge_{0.18}$(001) than in Si(001) or Ge(001) layers implies that the presence

of a Si-rich underlayer reduces the energy advantage of B residing in the second-layer vs bulk lattice sites, resulting in a lower segregation driving force for the alloy.

$\theta_B(T_s)$ values were obtained from TPD analyses of $Si_{0.82}Ge_{0.18}(001)$:B layers with $C_B = 5\times10^{19}$ cm^{-3} grown at temperatures T_s ranging from 500 to 700 °C. The experimental results show good agreement with values calculated using equation 7 with $\Delta H_s = -0.42$ eV, indicating that B segregation is in the equilibrium regime throughout this temperature range. That is, the B segregation rate is greater than the film growth rate, and θ_B decreases with increasing T_s. This is consistent with previous reports that B segregation during Si(001) GS-MBE is in the equilibrium regime at $T_s \geq 500$ °C,[2] and that the transition temperature to kinetically limited segregation of $Si_{1-x}Ge_x(001)$ layers tends to decrease with increasing x.[20]

7.3.3. $Si_{1-x}Ge_x(001)$:B growth kinetics

$R_{SiGe}(T_s)$ results for undoped $Si_{1-x}Ge_x(001)$ GS-MBE have been well described using a linear superposition of the reactive sticking probabilities of Si_2H_6 and Ge_2H_6 on each surface species, while using the results of the TPD analyses to determine hydrogen desorption rates and, hence, the steady-state dangling-bond coverage associated with each surface species.[5] This treatment, developed in ref. 7, led to the following equation:

$$R_{SiGe} = \frac{2}{N_{SiGe}}\left[\theta_{Si} f_{Si}^2 (J_{Si_2H_6} S^{Si}_{Si_2H_6} + J_{Ge_2H_6} S^{Si}_{Ge_2H_6}) + \theta_{Ge} f_{Ge}^2 (J_{Si_2H_6} S^{Ge}_{Si_2H_6} + J_{Ge_2H_6} S^{Ge}_{Ge_2H_6})\right] \quad (8)$$

f_{Si} and f_{Ge} are the Si and Ge dangling bond densities, while $S^{Si}_{Si_2H_6} = 0.036$[21] and $S^{Ge}_{Ge_2H_6} = 0.052$[22] are the reactive sticking probabilities of Si_2H_6 and Ge_2H_6 on Si(001) and Ge(001), respectively, and $S^{Ge}_{Si_2H_6} = 0.0068$ and $S^{Si}_{Ge_2H_6} = 0.28$ are the corresponding cross-terms.[7] $S^{Si}_{Si_2H_6}$ has, over the film growth temperature range of interest, a weak temperature dependence, with an activation energy for reactive adsorption of -0.16 eV.[22] The temperature dependence of $S^{Ge}_{Ge_2H_6}$ is also very weak with an activation energy for reactive adsorption of < 0.2 eV.[23] H_2 desorption kinetics during $Si_{1-x}Ge_x(001)$ GS-MBE from Si_2H_6 and Ge_2H_6 with $x > 0.02$ obey second-order kinetics.[5] For undoped $Si_{0.82}Ge_{0.18}(001)$ GS-MBE at T_s = 500 °C,

the steady-state H and Ge coverages are $\theta_H = 0.37$ ML and $\theta_{Ge} = 0.63$ ML, and while θ_{Ge} is constant with increasing C_B, θ_H decreases due to the B-induced reduction in the average H_2 desorption energy.

As discussed above, the presence of second-layer B atoms affects the total dangling-bond coverage. Here we define f_{Si}^* and f_{Ge}^* as the dangling-bond fractions on B-backbonded Si and Ge atoms, and f_{Si}^o and f_{Ge}^o as the non-B-backbonded Si and Ge dangling-bond fractions. Combining equations 4-7, the total Si and Ge dangling-bond densities are:

$$f_{Si} = f_{Si}^o\theta_{Si^o} + f_{Si}^*\theta_{Si^*} = \left(\frac{f_{Si}^o + 0.25\left(f_{Si}^o + f_{Si}^*\right)\frac{C_B}{N_{SiGe}}\exp\left(\frac{-\Delta H_s}{kT_s}\right)}{1+\frac{C_B}{N_{SiGe}}\exp\left(\frac{-\Delta H_s}{kT_s}\right)} \right) \tag{9}$$

and

$$f_{Ge} = f_{Ge}^o\theta_{Ge^o} + f_{Ge}^*\theta_{Ge^*} = \left(\frac{f_{Ge}^o + 0.25\left(f_{Ge}^o + f_{Ge}^*\right)\frac{C_B}{N_{SiGe}}\exp\left(\frac{-\Delta H_s}{kT_s}\right)}{1+\frac{C_B}{N_{SiGe}}\exp\left(\frac{-\Delta H_s}{kT_s}\right)} \right) \tag{10}$$

The steady-state fractional dangling-bond coverages f_{Si}^o and f_{Ge}^o, during $Si_{1-x}Ge_x(001)$ film growth for which Si_2H_6 and Ge_2H_6 adsorption and H desorption kinetics are second order are given by[21,5]

$$f_{Si}^o = \left[1 + \sqrt{\frac{2J_{Si_2H_6}S_{Si_2H_6}}{N_{SiGe}\nu_{Si}\exp\left(-\frac{E_{Si}}{kT_s}\right)}} \right]^{-1} \tag{11}$$

and

$$f_{Ge}^o = \left[1 + \sqrt{\frac{2J_{Ge_2H_6}S_{Ge_2H_6}}{N_{SiGe}\nu_{Ge}\exp\left(-\frac{E_{Ge}}{kT_s}\right)}} \right]^{-1} \tag{12}$$

where E_{Si} and E_{Ge} are the Ge-coverage dependent H_2 desorption activation energies from Si and Ge surface sites respectively,[5] and the pre-exponential factors are $\nu_{Si} = 7.9\times10^{11}$ s^{-1} and

$\nu_{Ge} = 5.0\times10^{14}\ s^{-1}$.[2,4] Similarly, f_{Si}^{*} and f_{Ge}^{*} in equations 9 and 10 can be written by replacing E_{Si}, and E_{Ge} in equations 11 and 12 with E_{Si}^{*} and E_{Ge}^{*}, the activation energies for hydrogen desorption from B-backbonded Si^{*} and Ge^{*} surface species, respectively.

Using a equations 8-12, we calculate $R_{SiGe}(C_B)$ based upon the desorption activation energies in Table 7.1. The results, R_{SiGe} vs C_B, are plotted as a solid line in Figure 7.4, are found to be in very good agreement with the experimental data. R_{SiGe} is very sensitive to ΔH_s, and increases with increasing values. For a given B concentration at T_s = 500 °C, the second-layer B coverage in $Si_{0.82}Ge_{0.18}(001)$ layers is lower than in Si(001), hence the total dangling-bond density is higher.

7.3.4. B incorporation kinetics

B_2H_6 dissociatively adsorbs with second-order kinetics on Si(001)[24] and Ge(001)[25] through reaction with Si or Ge dangling-bonds. The B deposition rate on Si(001) and Ge(001) can be expressed:[24,25]

$$R_B = \frac{2S_{B_2H_6}J_{B_2H_6}\theta_{db}^2}{N} \tag{13}$$

where θ_{db} is the dangling bond density and N is the Si or Ge bulk number density. Thus, combining equation (13) with equation (8), the B concentration, expressed as the ratio of the B deposition rate to the overall film deposition rate during $Si_{1-x}Ge_x$ GS-MBE is given by

$$C_B = \frac{R_B}{R_{SiGe}} = \frac{S_{B_2H_6}J_{B_2H_6}\theta_{db}^2}{\theta_{Si}f_{Si}^2(J_{Si_2H_6}S_{Si_2H_6}^{Si} + J_{Ge_2H_6}S_{Ge_2H_6}^{Si}) + \theta_{Ge}f_{Ge}^2(J_{Si_2H_6}S_{Si_2H_6}^{Ge} + J_{Ge_2H_6}S_{Ge_2H_6}^{Ge})}. \tag{14}$$

From the C_B vs ξ results in Fig. 7.3, the overall B_2H_6 reactive sticking probability $S_{B_2H_6}$ during growth of $Si_{0.82}Ge_{0.18}(001)$ is $2.5\text{x}10^{-4}$. This is essentially equal to the value obtained for B doping during Si(001) GS-MBE and approximately an order of magnitude higher than for Ge(001):B growth, at the same growth temperature.[2,4]

At flux ratios $\xi > 0.3$ (Fig. 7.3), corresponding to $\theta_B > \theta_{B,sat}$, we observe that the incorporated B concentration increases with increasing ξ at a faster rate than the calculated curve. Ratios of experimental to calculated values exceeding two for $\xi \geq 0.5$. A similar effect

was previously observed for B incorporation in Si(001).[13] As θ_B exceeds the saturated second-layer B coverage, excess B segregates to the outer surface and a parallel B incorporation pathway is opened. However, B incorporated into Si(001) through this reaction path resides in non-elecrically-active sites. Initial Hall measurements show that this is also the case for $Si_{0.82}Ge_{0.18}$(001):B. The maximum fully electrically-active B concentrations in $Si_{0.82}Ge_{0.18}$(001) l layers grown at T_s = 500 °C is 4.6×10^{20} cm^{-3}.

7.4. Conclusions

B-doped $Si_{0.82}Ge_{0.18}$(001) films, with concentrations $C_B = 2\times10^{16}$-2×10^{21} cm^{-3}, were grown by gas-source molecular beam epitaxy (GS-MBE) from Si_2H_6, Ge_2H_6, and B_2H_6 at T_s = 500-700 °C. D_2 TPD spectra were used to show that B strongly segregates to the second-layer, and to determine B coverages. B incorporation as a function of the incident flux ratio ξ was linear with C_B up to 5×10^{20} cm^{-3} corresponding to a saturated second-layer coverage of 0.5 ML. Ge incorporation, and the Ge segregation rate were found to be independent of the B_2H_6 flux. Strain, the primary driving force for B segregation was partially relieved by the presence of segregating Ge atoms at the surface. Increasing the Ge concentration from 0 to 18 at% led to a decrease of 0.11 eV in the B segregation enthalpy. The overall B_2H_6 sticking probability during growth of $Si_{0.82}Ge_{0.18}$(001) at T_s = 500 °C, 2.5×10^{-4}, is essentially equal to that on Si(001) and much larger than on Ge(001). Film deposition rates R_{SiGe} decrease by $\approx$ factor of two with increasing $C_B > 5\times10^{19}$ cm^{-3}. Using a combination of previous D_2 TPD results for ultra-highly doped Si(001) and Ge(001) together with the present TPD results for $Si_{0.82}Ge_{0.18}$(001):B, we have developed a predictive model for $R_{SiGe}(x,C_B)$ which exhibits very good agreement with experimental data and provides mechanistic insight into the growth process.

7.5. References

1. G. Glass, H. Kim, M.R. Sardela, Q. Lu, J.A. Abelson, and J.E. Greene, Surface Science, 392, L63 (1997).
2. H. Kim, G. Glass, T. Spila, N. Taylor, J. R. Abelson, and J. E. Greene, J. Appl. Phys. 82, 2288 (1997).
3. H. Kim, G. Glass, S.Y. Park, T. Spila, N. Taylor, J.R. Abelson, and J.E. Greene, Appl. Phys. Lett. 69, 3869 (1996).
4. H. Kim and J. E. Greene, J. Vac. Sci. Technol. A17, 354 (1999).
5. H. Kim, N. Taylor, T. R. Bramblett, and J. E. Greene, J. Appl. Phys. 84, 6372 (1998).
6. H. Kim, N. Taylor, J.R. Abelson, and J.E. Greene, J. Appl. Phys. 82, 6062 (1997).
7. H. Kim, P. Desjardins, J. R. Abelson, and J. E. Greene, Phys. Rev. B58, 4803 (1998).
8. R.L. Headrick, B.E. Weir, A.F. Levi, D.J. Eaglesham, and L.C. Feldman, Appl. Phys. Lett. 57, 2779 (1990).
9. Y. Wang, and R.J. Hamers, Appl. Phys. Lett. 56, 2057 (1995), and J. Vac. Sci. Technol. A13, 1431 (1995).
10. Y. Wang, R.J. Hamers, and E. Kaxiras, Phys. Rev. Lett. 74, 403 (1995).
11. B. E. Weir, R. L. Headrick, Q. Shen, L.C. Feldman, M. S. Hybertson, M. Needels, M. Schluter, and T. R. Hart, Phys. Rev. B 46, 12861 (1992).
12. *Handbook of Chemistry and Physics*, ed.: D.R. Lide, 77th Edition, (CRC Press, Boca Raton, Florida, 1996).
13. G. Glass, H. Kim, P. Desjardins, N. Taylor, T. Spila, Q. Lu, and J. E. Greene, Phys. Rev. B, Submitted, A. Vailionis, G. Glass, P. Desjardins, David G. Cahill, and J.E. Greene, Phys. Rev. Lett. **82**, 4464 (1999).
14. P.A. Redhead, Vacuum 12, 203 (1962).
15. F.M. Lord, and J.S. Kittelberger, Surf. Sci. 43, 173 (1974).
16. Ph. Avouris, I.W. Lyo, F. Bozso, and E. Kaxiras, J. Vac. Sci. Technol. A 8, 3405 (1990).
17. S.A. Barnett and J.E. Greene, Surf. Sci. 151, 67 (1985).
18. J.E. Rowe, D.M. Riffe, G.K. Wertheim, and J.C. Bean, Appl. Phys. Lett. **76**, 4915 (1995).
19. M. Ramamoorthy, E.L. Briggs, and J. Bernholc, Phys. Rev. B 59, 4813 (1999).
20. C.P. Parry, R.A. Kubiak, S.M. Newstead, T.E. Whall, and E.H.C. Parker, Mat. Res. Soc. Symp. Proc. 220, 79 (1991); C.P. Parry, R.A. Kubiak, S.M. Newstead, E.H.C. Parker, and T.E. Whall, Mat. Res. Soc. Symp. Proc. 220, 103 (1991).
21. T.R. Bramblett, Q. Lu, T. Karasawa, M.-A. Hasan, S.K. Jo, and J.E. Greene, J. Appl. Phys. 76, 1884 (1994).

22. J. R. Engstrom, L.-Q. Xia, M. J. Furjanic, and D. A. Hansen, Appl. Phys. Lett. 63, 1821 (1993).

23. G. Eres and J. W. Sharp, J. Vac. Sci. Technol.A 11, 2463 (1993).

24. Q. Lu, T.R. Bramblett, N.-E. Lee, M.-A. Hasan, T. Karasawa, and J.E. Greene, J. Appl. Phys. 77, 3067 (1995).

25. T. R. Bramblett, Q. Lu, N.-E. Lee, N. Taylor, M.-A. Hasan, and J. E. Greene, J. Appl. Phys. 77, 1504 (1995).

Table 7.1. Summary of parameters used for deconvoluting $Si_{0.82}Ge_{0.18}(001)$:B TPD spectra

TPD feature	Surface phase	Adatom species	Peak temp. T_p (°C)	Activation energy for D_2 desorption E_d (eV)	E_d determination
β_1	Si monodeuteride	Si^o	450	2.32	ref. 5
β_1^*	B-backbonded Si monodeuteride	Si^*	400	2.11	$E_{\beta_1}/E_{\beta_1^*}=1.1$ refs. 5, 2
β_1'	mixed Si-Ge dimer monodeuteride	$Si\text{-}Ge^o$	430	2.23	ref. 5
$\beta_1'^*$	B-backbonded mixed Si-Ge dimer monodeuteride	$Si\text{-}Ge^*$	380	2.03	$E_{\beta_1}/E_{\beta_1^*}=1.1$ refs. 5, 2
α_1	Ge monodeuteride	Ge^o	325	1.85	ref. 5
α_1^*	B-backbonded Ge monodeuteride	Ge^*	302	1.78	$E_{\alpha_1}/E_{\alpha_1^*}=1.04$ refs. 5, 4
α_2	Ge dideuteride	Ge^o	a	1.76	refs. 5, 4
α_2^*	B-backbonded Ge dideuteride	Ge^*	a	<1.76	refs. 5, 4
β_2	Si dideuteride	Si^o	365[b]	1.95[b]	ref. 5
β_2^*	B-backbonded Si dideuteride	Si^*	300[b]	1.76[b]	$E_{\beta_2}/E_{\beta_2^*}=1.1$ refs. 5, 2
B	desorption from atomic B at the outer surface	B	a	1.76	ref. 2

[a] Contributes to desorption feature centered at 270 °C

[b] Species accounts for less than 0.05 ML coverage for all samples investigated

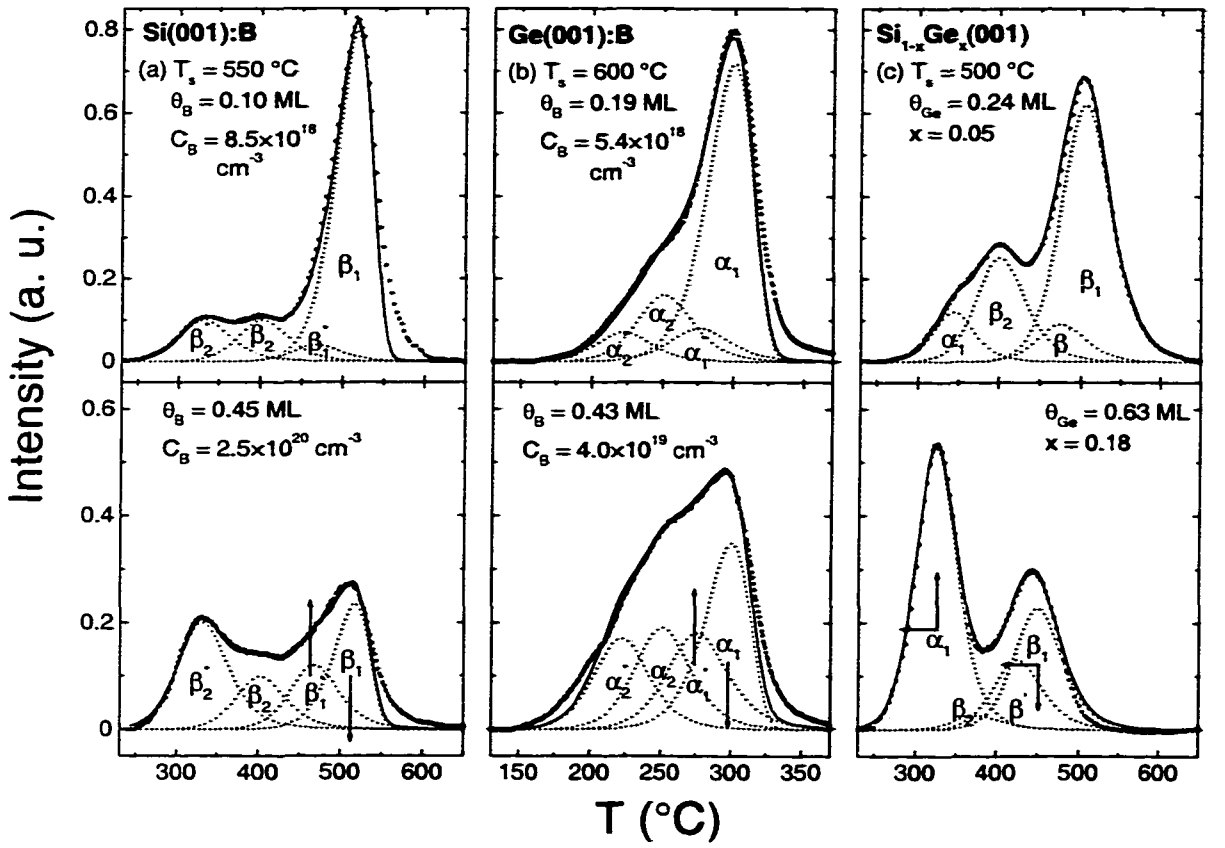

Figure 7.1. TPD spectra from (a) GS-MBE Si(001):B layers doped to concentrations C_B 8.5×10^{18} and 2.5×10^{20} cm^{-3}, (b) GS-MBE Ge(001):B layers with $C_B = 5.4\times10^{18}$ and 4×10^{19} cm^{-3}, and (c) undoped GS-MBE $Si_{1-x}Ge_x(001)$ layers with x = 0.05 and 0.18. The arrows indicate the effects of increased B or Ge concentration on the intensity and position of primary desorption peaks.

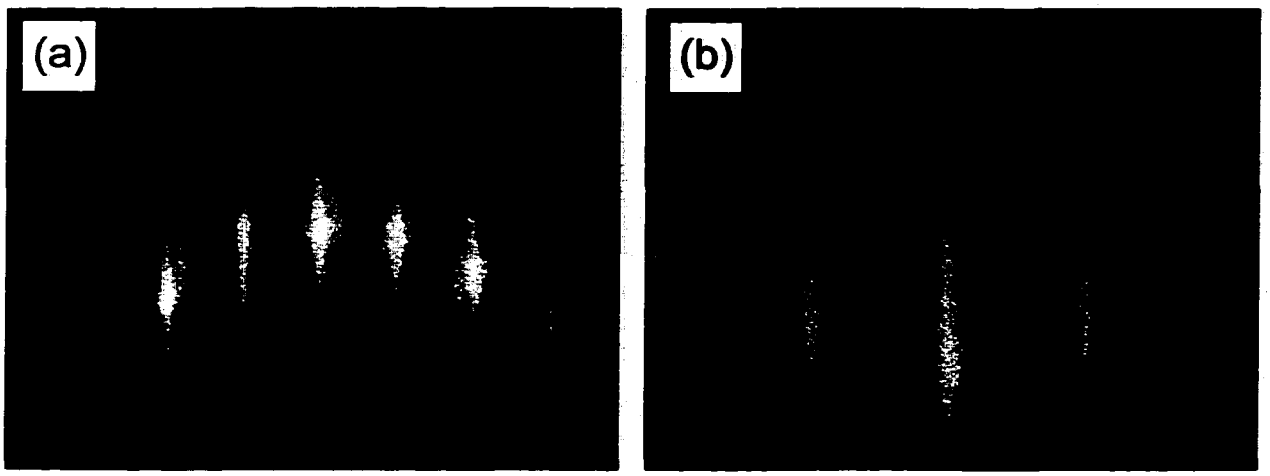

Figure 7.2. RHEED patterns for B-doped $Si_{0.82}Ge_{0.18}(001)$ layers with C_B values of (a) 5×10^{19} cm^{-3} and (b) 1.5×10^{21} cm^{-3}.

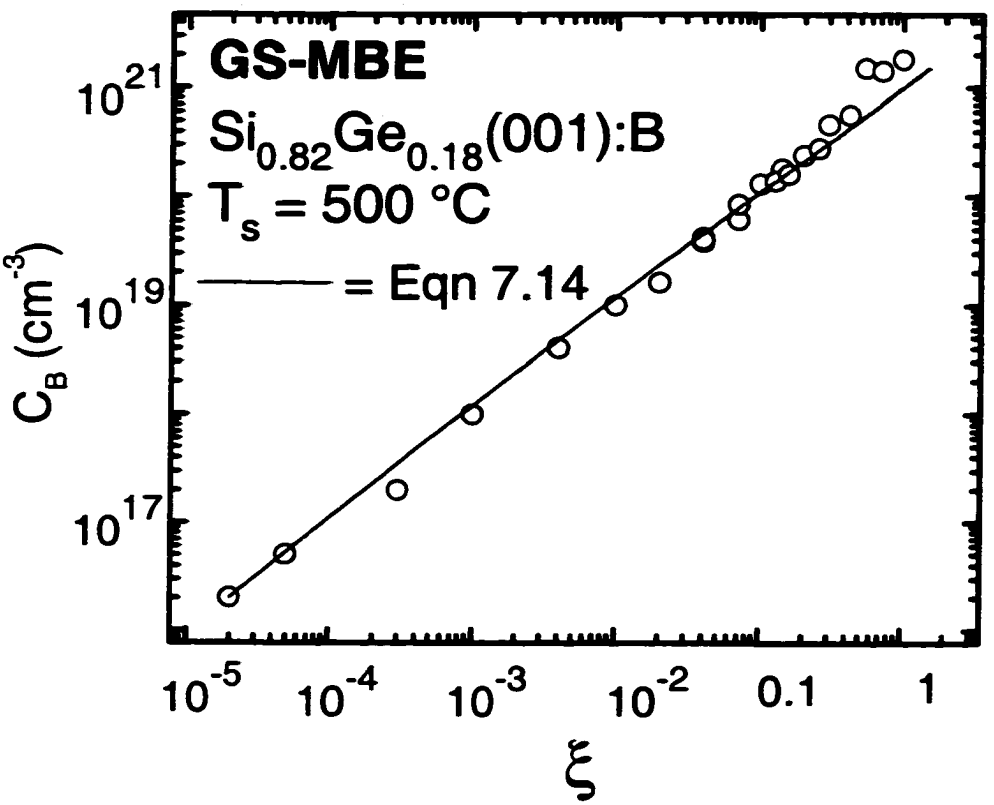

Figure 7.3. B concentrations C_B in $Si_{0.82}Ge_{0.18}$(001) GS-MBE layers as a function of impingement flux ratio $\xi = 10^{-5}$ to 1.

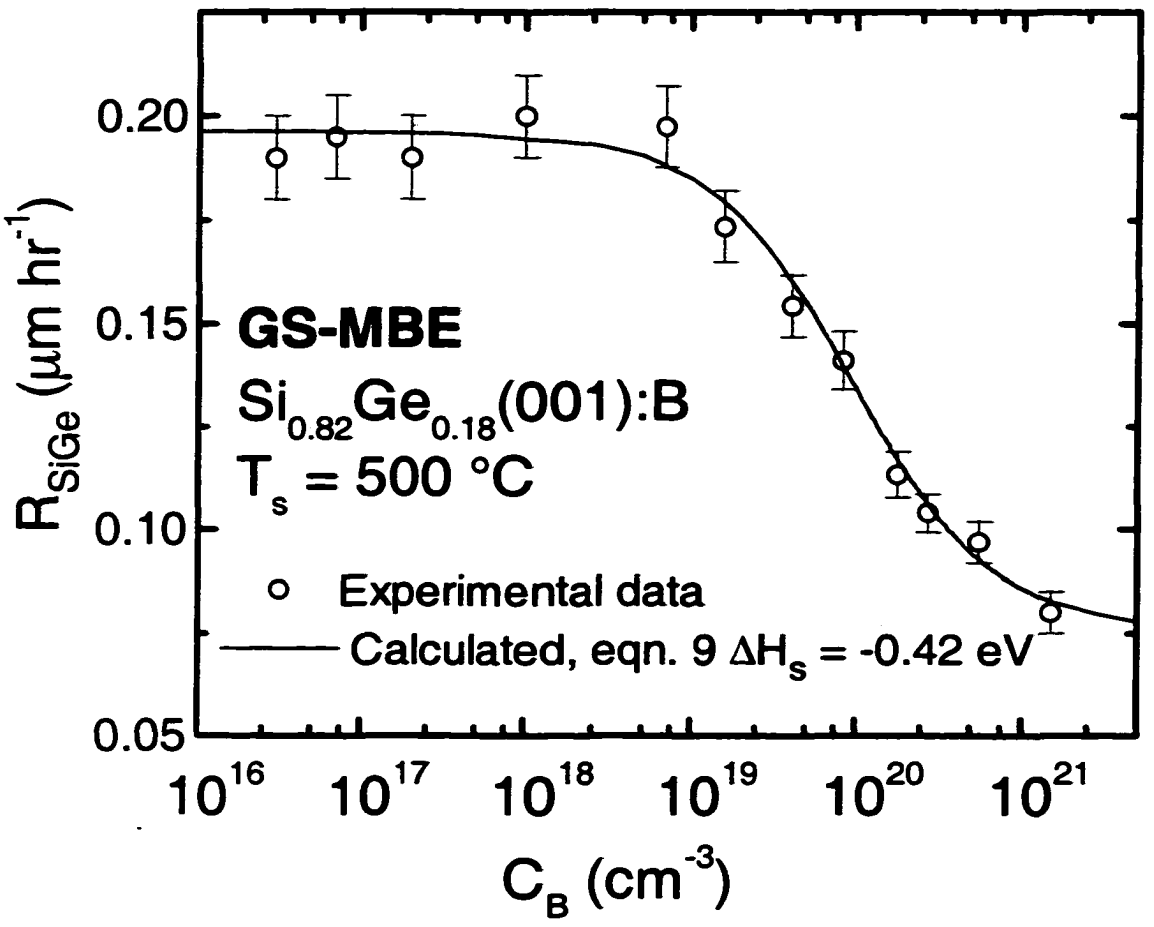

Figure 7.4. Experimental (data points) and calculated (solid lines, see section 7.3) GS-MBE $Si_{0.82}Ge_{0.18}$(001):B GS-MBE deposition rates R_{SiGe} as a function of the bulk B concentration C_B in layers grown from $Si_2H_6/Ge_2H_6/B_2H_6$ mixtures with $J_{Si_2H_6}$ and $J_{Ge_2H_6}$ maintained constant at 2.2×10^{16} and 6.6×10^{14} cm^{-2} s^{-1}.

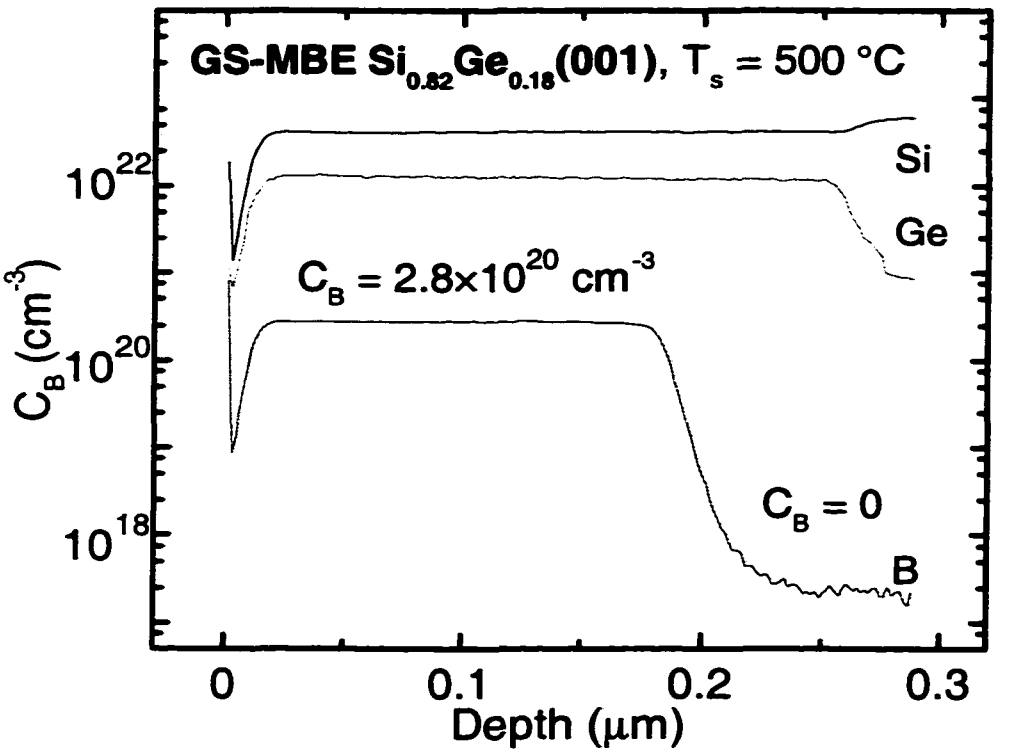

Figure 7.5. SIMS depth profile through a 1800-Å-thick B-doped $Si_{0.82}Ge_{0.18}(001)$ layer with $C_B = 2.8\times10^{20}$ cm^{-3} grown on a 600-Å-thick undoped $Si_{0.82}Ge_{0.18}(001)$ layer on Si(001).

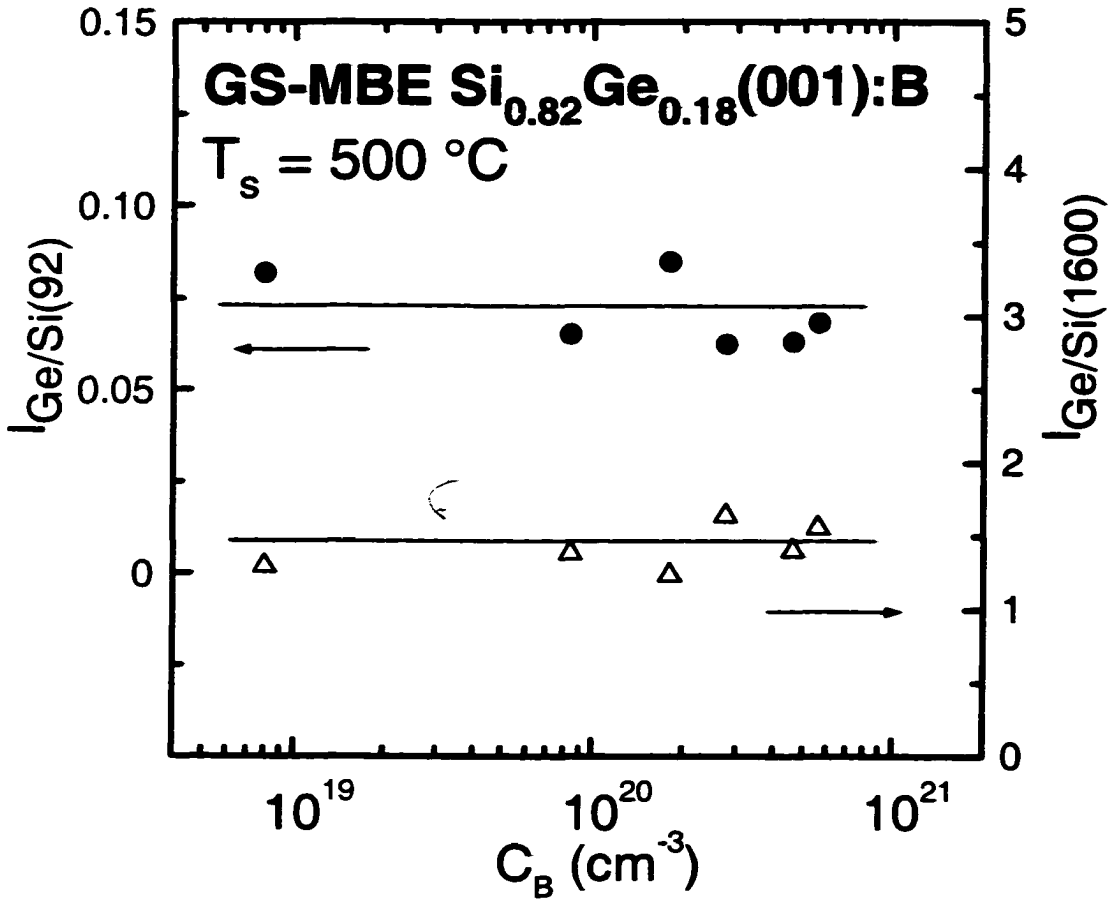

Figure 7.6. AES peak intensity ratios of the Ge KLL (1147 eV) I_{Ge} to Si LMM (92 eV) $I_{Si(92)}$ and Si KLL (1600 eV) $I_{Si(1600)}$ peaks as a function of B concentration C_B for B-doped $Si_{0.82}Ge_{0.18}(001)$ films.

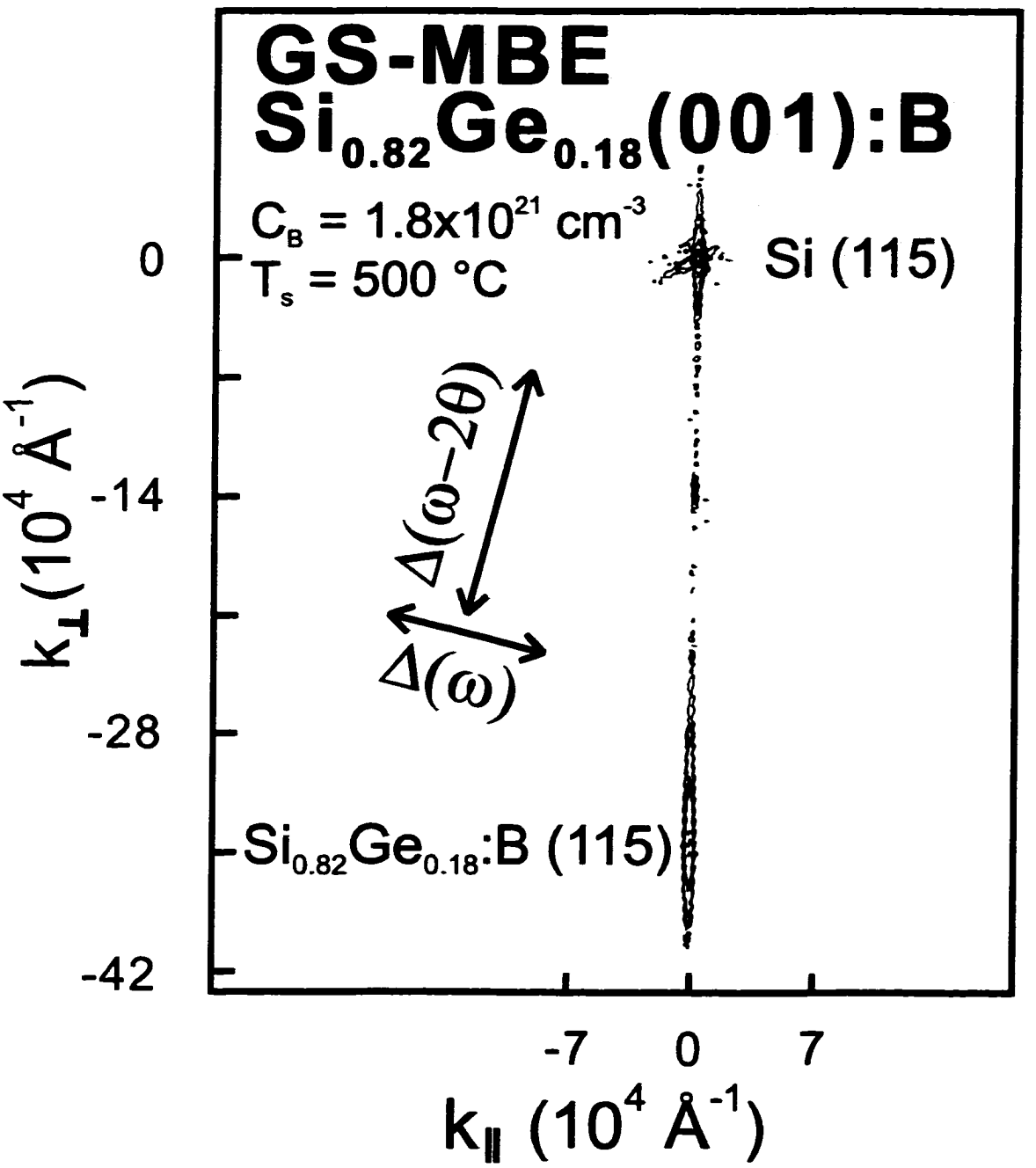

Figure 7.7. High-resolution 115 reciprocal space map from a 1500-Å-thick $Si_{0.82}Ge_{0.18}$(001):B layer with a B concentration C_B of $1.8x10^{21}$ cm^{-3}. Successive isointensity contours correspond to 40000, 10000, 750, 100, 15, and 5 counts s^{-1}.

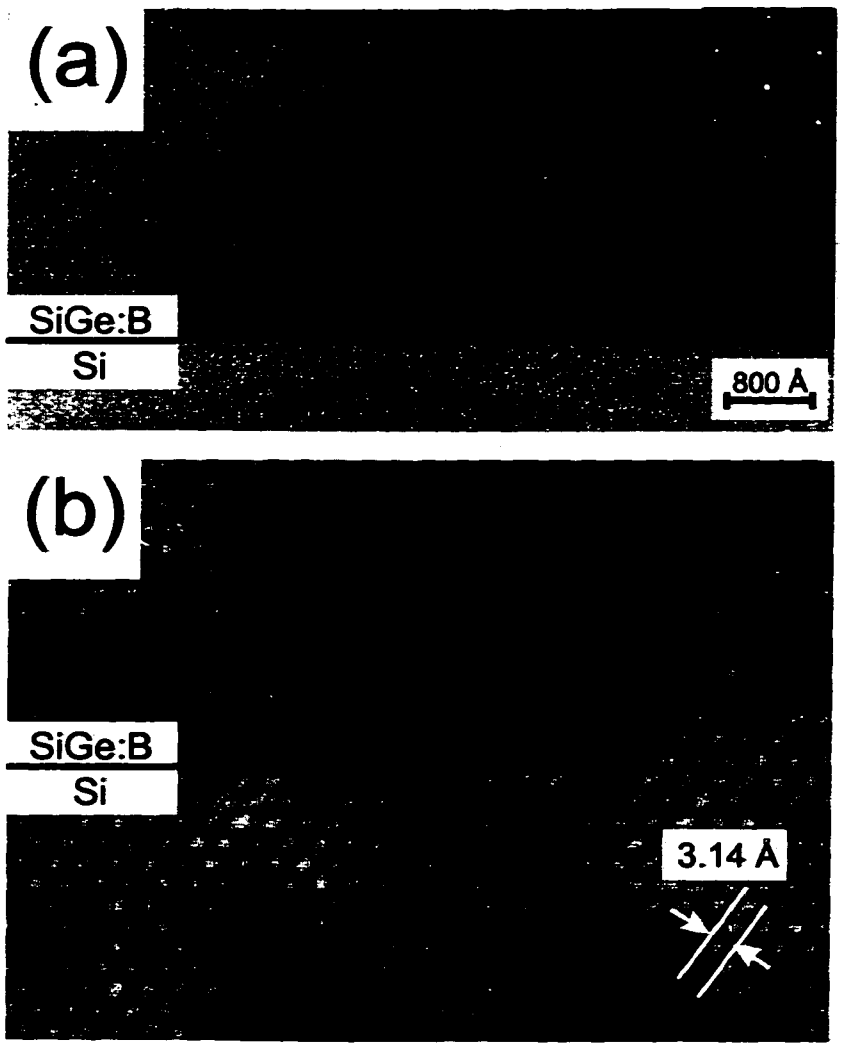

Figure 7.8. (a) A [110] XTEM micrograph from a GS-MBE $Si_{0.82}Ge_{0.18}(001)$ layer with C_B = $2x10^{20}$ cm^{-3} grown at T_s = 500 °C from Si_2H_6,Ge_2H_6 and B_2H_6. (b) A high-resolution image of the same sample.

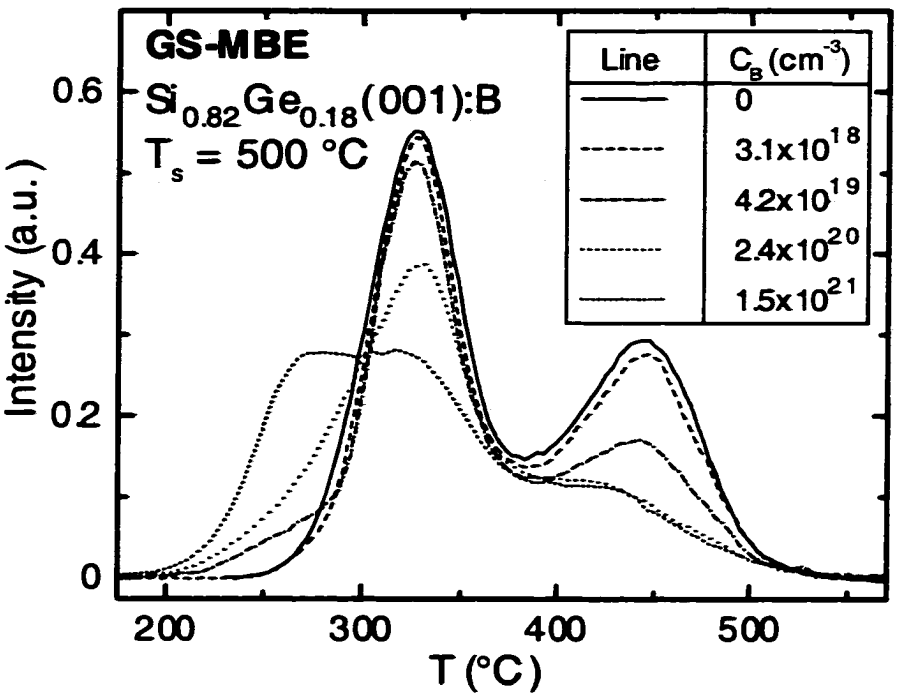

Figure 7.9. D_2 TPD spectra from GS-MBE $Si_{1-x}Ge_x(001)$:B films grown at $T_s = 500$ °C and doped to concentrations $C_B = 0, 3.1\times10^{18}, 4.2\times10^{19}, 2.4\times10^{20}$, and 1.5×10^{21} cm^{-3}.

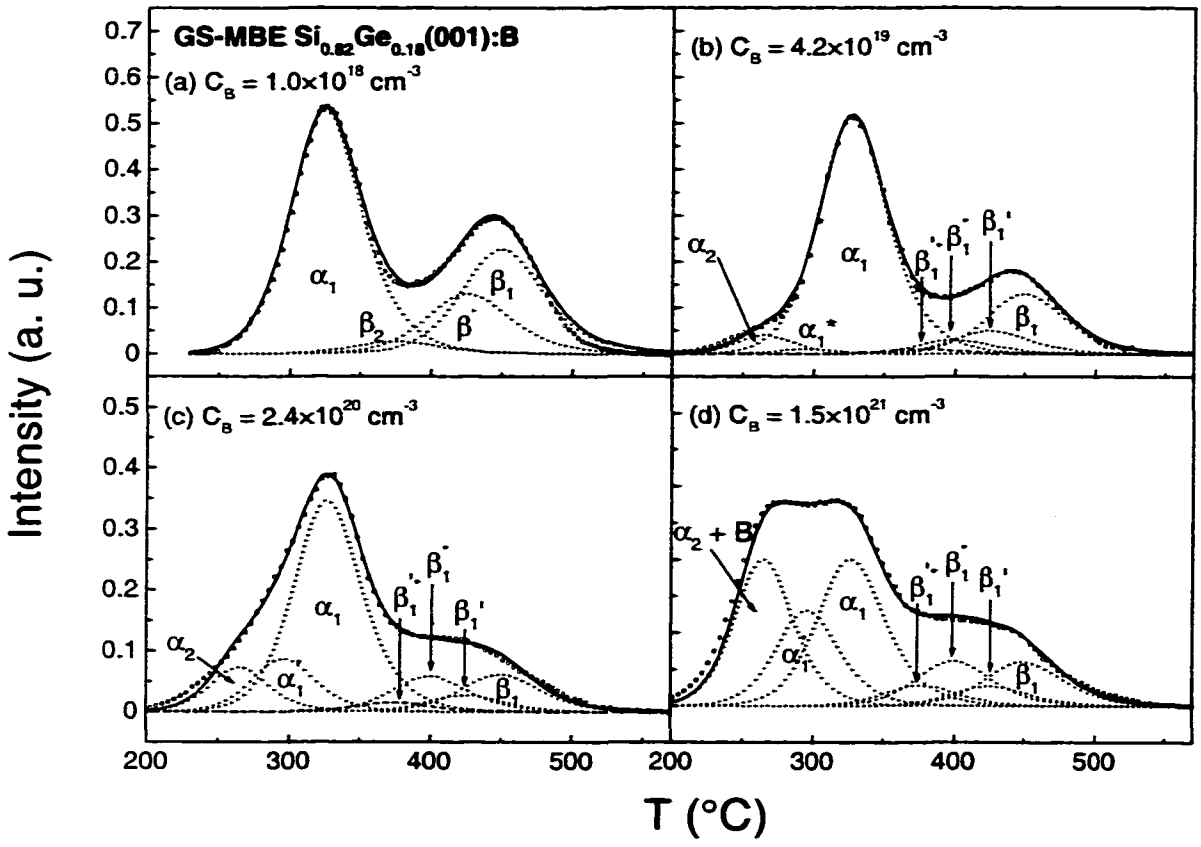

Figure 7.10. Deconvoluted D_2 TPD spectra from GS-MBE $Si_{1-x}Ge_x(001)$:B films grown at T_s =500 °C and doped to concentrations $C_B = 1\times10^{18}$, 4.2×10^{19}, 2.4×10^{20}, and 1.5×10^{21} cm^{-3}.

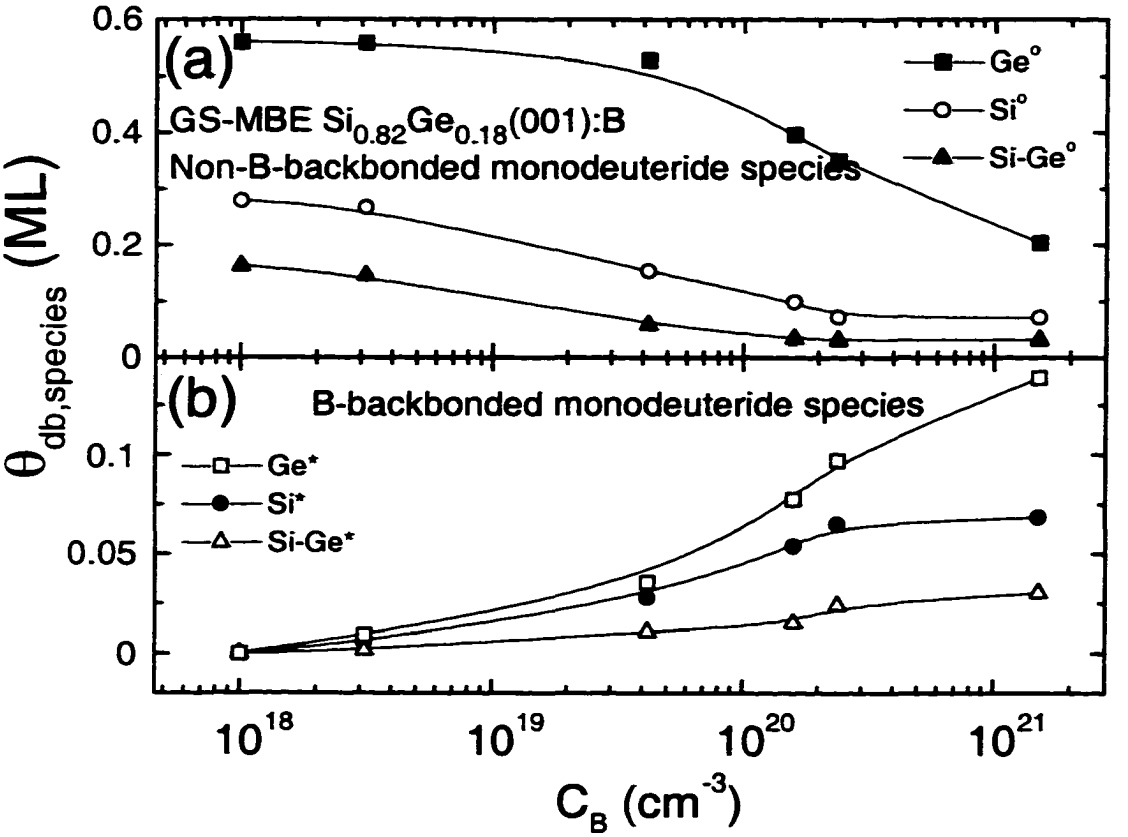

Figure 7.11. (a) non-B-backbonded Ge°, Si°, and Si-Ge° dimer species dangling-bond coverages, and (b) B-backbonded Ge^{*}, Si^{*}, and Si-Ge^{*} dimer species dangling-bond coverages.

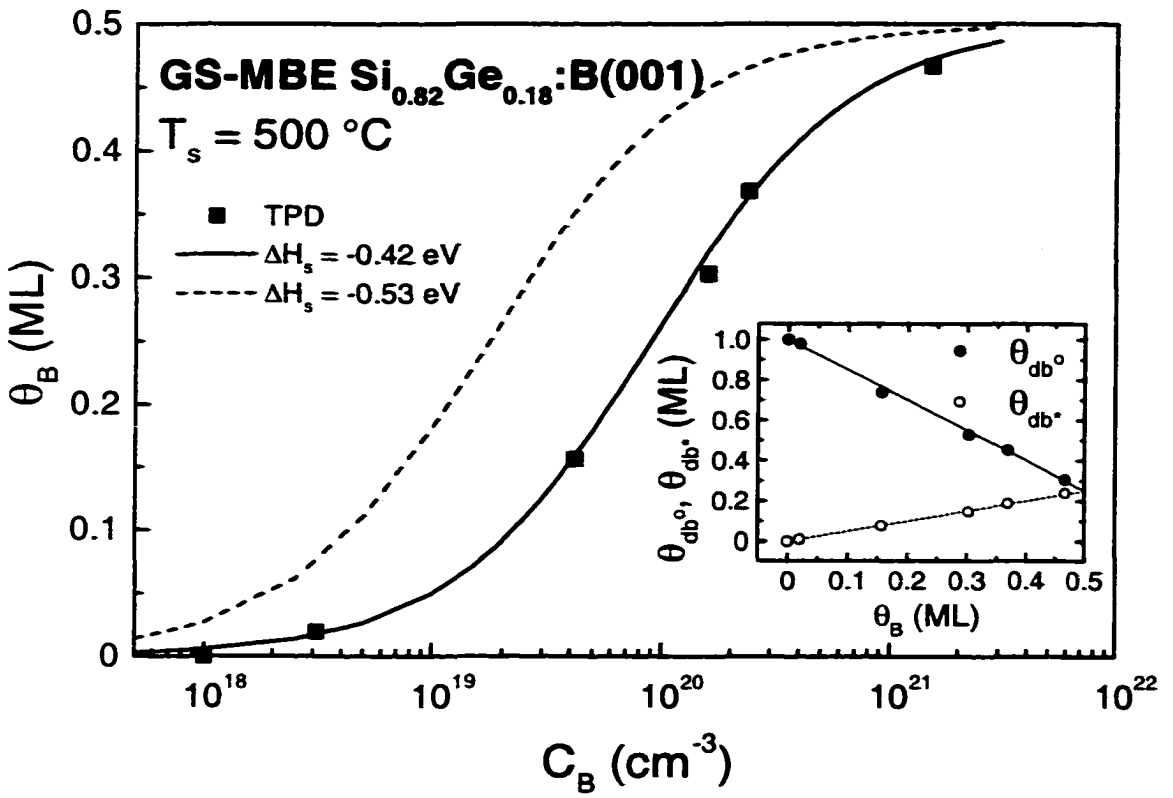

Figure 7.12. B surface coverages θ_B (data points) as a function of bulk B concentrations C_B in GS-MBE $Si_{0.82}Ge_{0.18}(001)$:B films grown from $Si_2H_6/Ge_2H_6/B_2H_6$ mixtures at $T_s = 500$ °C. Calculated values from eqn. 7 using segregation enthalpies $\Delta H_s = -0.53$, and -0.42 eV are plotted as lines. Inset: Dangling-bond densities (data points) of B-backbonded θ_{db^*}, and non-B-backbonded species θ_{db^o}, and calculated values from eqns. 7.5 and 7.6 (lines).

CHAPTER 8. Conclusions

In this thesis, I show that *in-situ* ultra-high B doping of $Si_{1-x}Ge_x$ has significant and complex effects on H_2 desorption kinetics, and hence on layer growth rates. The fact that B, present in concentrations in the part-per-thousand range can have such a profound effect on surface kinetic processes is a clear signature of strong B segregation during growth. The use of TPD in the analysis of surface species coverages and H_2 desorption energies was essential for the development of a predictive model for the growth kinetics of intrinsic and doped $Si_{1-x}Ge_x(001)$ layers. Quantitative measurement of the second-layer B coverage was also critical for model development. I show that while B concentrations increase linearly with impingement flux ratio under conditions corresponding to sub-saturation B coverages, the B_2H_6 reactive sticking probability increases dramatically for B coverages above saturation. Complementary measurements including SIMS, Hall-effect, HR-XRD, and NEXAFS revealed that the increased B concentrations correspond to concentrations of electrically-active and inactive B atoms, the latter present in the form of pairs. Finally, I showed that the inactive B atoms were directly incorporated at the growth surface.

8.1. Effect of B on H_2 desorption and Si(001) growth kinetics

At high B doping concentrations in Si(001) films, ordered B subunits in the second layer weaken surface Si-H bonds while deactivating Si dimer dangling bonds during film growth. These effects are exacerbated by the strong tendency for B segregation giving rise to steady state segregation ratios r_B up to 1200 at 550 °C. The segregation enthalpy ΔH_s was determined to be -0.53 eV. Results from Si(001) layers doped with B concentrations C_B between $1x10^{17}$ and $1.2x10^{22}$ cm^{-3} and grown on Si(001)2x1 at temperatures T_s = 500-850 °C by GS-MBE from Si_2H_6 and B_2H_6, were used to model the effects of ultra-high B doping on Si(001):B GS-MBE growth kinetics. R_{Si} increases with increasing $C_B \geq 2x10^{19}$ cm^{-3} at $T_s \leq 550$ °C, where steady state H coverages are high, due to B-enhanced H desorption rates.

At $T_s \geq 600$ °C, corresponding to much lower steady state θ_H values, R decreases due to B-induced deactivation of Si dangling bonds.

8.2. B incorporation and bonding in Si(001)

B incorporation in Si(001) layers was investigated. C_B increases linearly with the incident precursor flux ratio $J_{B_2H_6}/J_{Si_2H_6}$ and, for $T_s < 700$ °C, B is incorporated into substitutional electrically-active sites at concentrations up to C_B^*. For $T_s = 600$ °C, C_B^* is 2.5×10^{20} cm^{-3}. At higher B concentrations, C_B increases faster than $J_{B_2H_6}/J_{Si_2H_6}$ and there is a large and discontinuous decrease in the electrically-active fraction of incorporated B. However, the total activated B concentration continues to increase and reaches a value of $N_B = 1.3 \times 10^{21}$ cm^{-3} with $C_B = 1.2 \times 10^{22}$ cm^{-3}. Resistivities are in good agreement with theoretical values to for C_B values up to C_B^*, where $\rho_{300K} = 300$ μΩ-cm. Conductivity mobilities are equal to theoretical maximum values for C_B up to 1.6×10^{21} cm^{-3}.

HR-XRD and reciprocal space mapping measurements show that all films are fully strained. No B precipitates, or misfit dislocations, were detected by HR-XRD and TEM analyses, even in films with $C_B = 1.2 \times 10^{22}$ cm^{-3} (24 at% B). The lattice constant in the film growth direction $a_\perp$ decreases linearly with increasing C_B up to the limit of full electrical activation and continues to decrease, but non-linearly, with $C_B > C_B^*$.

HR-XRD, SIMS, Hall-effect, NEXAFS, and TEM data were used in concert to determine the nature and lattice site of electrically-inactive B. TEM/XTEM analyses imply that B clusters must be smaller than ≃ 50 Å, HR-XRD analyses show that the macroscopic strain contribution per inactive B atom is constant, Hall measurements show that the active B concentration continues to increase even when $C_B > C_B^*$, and NEXAFS measurements show that the concentration of trigonally-bonded B atoms increases proportionately to the electrically-inactive B concentration. These results indicate that B is present in small highly-dispersed nanoclusters of constant size. Based upon a detailed analysis of the out-of-plane Si(001):B lattice constants as a function of active and inactive B concentrations, we show that

inactive B is incorporated as trigonally-coordinated B pairs on single Si lattice sites and oriented with the B-B bond axis randomly aligned along ⟨001⟩ directions.

The fraction of inactive B decreases with increasing temperature indicating that the B pairing reaction is not diffusion controlled. Furthermore, the B concentration as a function of $J_{B_2H_6}/J_{Si_2H_6}$ becomes superlinear when $\theta_B > \theta_{B,sat}$, and the net increase in C_B is essentially equal to the concentration of inactive B. These factors support direct B pair incorporation at the growth surface. During high temperature growth ($T_s \geq 700$ °C), the situation is more complex. In addition to direct B incorporation at the surface, B clustering in the bulk is mediated by large concentrations of interstitial point defects resulting in B deactivation during growth when C_B exceeds $5x10^{19}$ cm^{-3}.

B strongly surface segregates to the second-layer with a saturation coverage $\theta_{sat,B}$ of 0.5 ML (corresponding to $C_B = C_B^*$ for $T_s < 700$ °C). At higher C_B, $\theta_B > \theta_{sat,B}$ and B accumulates in the upper layer, as shown by thermally programmed desorption measurements. The presence of upper layer B modifies the interaction of B_2H_6 with the Si surface, and opens a parallel reaction channel whereby B incorporates as pairs which are electrically inactive but have a low carrier scattering cross-section. At $C_B > 2x10^{21}$ cm^{-3}, carrier mobilities begin to degrade substantially. This is correlated with lattice plane buckling in response to local B-induced strain measured by x-ray diffraction as well as by TEM electron diffraction contrast measurements.

8.3. Effect of B on H_2 desorption and $Si_{0.82}Ge_{0.18}$(001) growth kinetics

B-doped $Si_{0.82}Ge_{0.18}$(001) films, with concentrations to 2×10^{21} cm^{-3}, were grown by gas-source molecular beam epitaxy (GS-MBE) from Si_2H_6, Ge_2H_6 and B_2H_6 at T_s = 500-700 °C. D_2 temperature-programmed desorption (TPD) was used to probe the surface structure, and to determine B coverages θ_B. TPD results indicate that the surface is composed of B-backbonded dimers, non-B-backbonded dimers, and dimer vacancies in essentially the same proportions as observed on Si(001):B surfaces at constant B coverage. B incorporation as a

function of incident flux ratio ξ was linear with C_B up to 5×10^{20} cm^{-3} corresponding to B coverages $\theta_B \leq 0.5$ ML. Ge incorporation and segregation rates were found to be independent of the diborane flux. Strain, the primary driving force for B segregation was partially relieved by Ge co-segregation. Increasing the Ge concentration from 0 to 18% led to a decrease of 0.11 eV in the B segregation enthalpy. C_B vs flux ratio measurements indicate that the B_2H_6 sticking probability on the $Si_{0.82}Ge_{0.18}(001)$ surface is much higher than that predicted by a linear superposition of sticking probabilities on pure Si(001) and Ge(001) surfaces. Film deposition rates R_{SiGe} decrease by $\simeq$ factor of 2 with increasing $C_B > 5\times10^{19}$ cm^{-3}.

Drawing upon our previous modeling results for $Si_{1-x}Ge_x(001)$ alloys, Si(001):B, Ge(001):B together with the $Si_{0.82}Ge_{0.18}(001)$:B results presented here, we have developed a comprehensive growth kinetics model. Predicted layer growth rates as a function of B and Ge concentrations exhibit excellent agreement with experimental data and it provides mechanistic insight into the growth process. These results build upon previous results obtained by our group and others, towards the ultimate goal of developing a predictive universal model for gas-source hydride layer growth.

CHAPTER 9. Future perspectives

9.1. Thermal stability of Si(001):B layers

Our results showing that B can be incorporated into GS-MBE/UHV-CVD Si(001) at concentrations well above 10^{21} cm^{-3} with no precipitation and yielding 100% electrical activation for C_B up to 2.5×10^{20} cm^{-3} have generated considerable excitement in the microelectronics community and raised practical issues concerning thermal stability of these layers doped well above reported equilibrium solid solubility limits. This section summarizes initial results of the use of *in-situ* high-resolution synchrotron x-ray diffraction (HR-XRD) measurements to follow the evolution of B depth profiles in real time during the annealing of Si(001):B layers with $C_B = 2\times10^{20}$ cm^{-3} at T_a = 600-1100 °C for t_a up to 12 h. These results are combined with post-deposition SIMS, TEM/XTEM, and temperature-dependent Hall measurements. An analysis of the overall data set show that all dopant species remained fully active with no evidence for precipitation or clustering. Moreover, the doping profiles remained abrupt, due to extensive concentration-enhanced diffusivity, as B diffuses into the Si substrate at the higher annealing temperatures.

9.2. Preliminary annealing results for ultra-highly doped Si(001):B

A series of 0.5-μm-thick ultra-highly B doped Si(001):B layers with $C_B = 2\times10^{20}$ cm^{-3} were grown on Si(001)2x1 at T_s = 600 °C by GS-MBE from Si_2H_6 and B_2H_6. Electrically-active B concentrations N_B were determined from temperature-dependent Hall-effect measurements while total B concentrations C_B were measured using quantitative SIMS analyses referenced to ion implanted samples with known B concentrations. The results showed that $N_B = C_B$ in all layers indicating that 100% of the B resides on electrically-active substitutional sites. HR-XRD reciprocal lattice maps obtained from asymmetric 115 reflections showed, with a resolution of better than 1 part in 10^5, that all layers were fully

strained and free from misfit dislocations. There was no measurable mosaicity. High-resolution TEM and XTEM analyses also revealed the films to be free of dislocations with no observable B precipitates.

The samples were annealed in a load-locked UHV chamber on beamline X16A at Brookhaven National Laboratory's Synchrotron Light Source. The annealing chamber was equipped with Be windows and mounted inside a five-circle HR-XRD goniometer equipped with a high-resolution monochromator and a single-bounce Ge (111) analyzer crystal. The ultra-highly doped samples were subjected to anneals in UHV at temperatures T_a = 600, 900, 950, 1000, 1050 and 1100 °C, for times up to 12 hours. During the anneals, the out-of-plane film lattice constants $a_\perp$ were measured *in-situ* every 30 s using ω–2θ HR-XRD radial scans near the Si(004) reciprocal lattice point. The large covalent radius mismatch between B and Si combined with the fact that the layers remained fully strained throughout these experiments allowed us to quantitatively measure small changes in B concentration depth distributions. The technique takes advantage of the fact that $a_\perp$ is related to C_B through the simple expression $a_\perp = a_{Si}(T_a) + \beta C_B$ where a_{Si} is the bulk Si lattice constant and $\beta = -4.5 \times 10^{-23}$ Å cm^3 is the volume contraction per B atom.

Fig. 9.1, showing four ω–2θ scans as a function of annealing time at T_a = 1000 °C, is typical of the type of real-time data obtained. All diffracted intensity distributions are fit using a fully dynamical simulation which yields C_B as a function of sample depth x. From the scan corresponding to the as-deposited layer (t_a = 0), the simulation shows that the film is uniformly doped with $C_B = 2 \times 10^{20}$ cm^{-3} in agreement with the SIMS and Hall measurements. After annealing for t_a = 0.4 h, the maximum in the 004 reflection has shifted to 34.45° indicating a peak B concentration $C_{B,max} = 1.5 \times 10^{20}$ cm^{-3} located at the layer free surface (x = 0) while the intensity distribution toward lower angles shows that B has diffused into the Si substrate. However, from fitting the distribution we find that the profile remains abrupt. With further annealing, $C_{B,max}$ continues to decrease (see Fig. 9.2 where each square corresponds to

a data point) and the B front continues to diffuse deeper into the substrate. This corresponds to a larger layer effective width and hence gives rise to an increase in the layer maximum scattering intensity.

Fig. 9.3 shows a SIMS $C_B(x)$ depth profile (which is in very good agreement with the *in-situ* XRD-determined profile) from an ultra-highly B doped sample annealed for 12 h at 1000 °C. The profile remains relatively abrupt, due to concentration enhanced diffusion, with $C_{B,max} = 5x10^{19}$ cm^{-3}. Hall measurements show that all B remains 100% electrically active. Similar depth profiles, together with complete electrical activity, were obtained under all annealing conditions except for $T_a = 600$ °C where no B redistribution was observed.

These results are of potential significance for ultra-high doping applications since the electrical activity is found to be thermally stable even under very aggressive thermal cycling. Moreover, the results are also important for materials processing where ultra-highly doped layers can be used as controlled B in-diffusion sources. Future work in this area should focus on modeling of B-concentration-dependent diffusion, the role of electrically-inactive B pairs during diffusion, and the effects of Ge alloying on diffusional behavior.

9.3. Dependence of the B_2H_6 reactive sticking probability on x

Our group has previously shown that B_2H_6 dissociatively adsorbs with second-order kinetics on Si(001)[1] and Ge(001)[2] through reaction with Si or Ge dangling-bonds. The B deposition rate on Si or Ge surfaces can thus be expressed as:[1,2]

$$R_B = \frac{2S_{B_2H_6} J_{B_2H_6} \theta_{db}^2}{N} \tag{9.1}$$

where θ_{db} is the dangling bond density and N is the Si or Ge bulk number density. Thus, combining equation (9.1) with equation (7.8), the B concentration, expressed as the ratio of B deposition rate to the overall deposition rate, in GS-MBE $Si_{1-x}Ge_x$ is given by:

$$C_B = \frac{R_B}{R_{SiGe}} = \frac{\frac{2}{N_{SiGe}}\left[S_{B_2H_6} J_{B_2H_6} \theta_{db}^2\right]}{\frac{2}{N_{SiGe}}\left[\theta_{Si} f_{Si}^2 (J_{Si_2H_6} S_{Si_2H_6}^{Si} + J_{Ge_2H_6} S_{Ge_2H_6}^{Si}) + \theta_{Ge} f_{Ge}^2 (J_{Si_2H_6} S_{Si_2H_6}^{Ge} + J_{Ge_2H_6} S_{Ge_2H_6}^{Ge})\right]}. \quad (9.2)$$

From the C_B vs ξ results in Fig. 7.3, the overall B_2H_6 reactive sticking probability $S_{B_2H_6}$ during growth of $Si_{0.82}Ge_{0.18}(001)$ is 2.5×10^{-4}. This is essentially equal to the value obtained for B doping during Si(001) GS-MBE, and approximately an order of magnitude higher than for Ge(001):B, at the same growth temperature.[2]

Currently there is little understanding of the Ge concentration dependence of the B_2H_6 chemisorption process on $Si_{1-x}Ge_x(001)$ surfaces. This area should be explored using a series of B-doped $Si_{1-x}Ge_x(001)$ layer growth experiments, each at a different Ge concentration. The B concentration expressed in equation 9.2 can then be rewritten to account explicitly for the reactive sticking probabilities of B_2H_6 on Si and Ge sites as shown in equation 9.3.

$$C_B = \frac{R_B}{R_{SiGe}} = \frac{\frac{2J_{B_2H_6}}{N_{SiGe}}\left(S_{B_2H_6}^{Si} \theta_{Si} f_{Si}^2 + S_{B_2H_6}^{Ge} \theta_{Ge} f_{Ge}^2\right)}{\frac{2}{N_{SiGe}}\left[\theta_{Si} f_{Si}^2 (J_{Si_2H_6} S_{Si_2H_6}^{Si} + J_{Ge_2H_6} S_{Ge_2H_6}^{Si}) + \theta_{Ge} f_{Ge}^2 (J_{Si_2H_6} S_{Si_2H_6}^{Ge} + J_{Ge_2H_6} S_{Ge_2H_6}^{Ge})\right]} \quad (9.3)$$

Thus we will be able to independently determine the B_2H_6 reactive sticking probabilities on Si and Ge sites independently. Through this work we hope to gain insight into the B_2H_6 reaction mechanism on $Si_{1-x}Ge_x(001)$ surfaces, and to better understand the key factors affecting reactive sticking probabilities in general.

9.4. References

1. Q. Lu, T.R. Bramblett, N.-E. Lee, M.-A. Hasan, T. Karasawa, and J.E. Greene, J. Appl. Phys. 77, 3067 (1995), G. Glass, H. Kim, P. Desjardins, N. Taylor, T. Spila, Q. Lu, and J. E. Greene, Phys. Rev. B, Submitted.
2. T. R. Bramblett, Q. Lu, N.-E. Lee, N. Taylor, M.-A. Hasan, and J. E. Greene, J. Appl. Phys. 77, 1504 (1995), H. Kim and J. E. Greene, J. Vac. Sci. Technol. A17, 354 (1999).

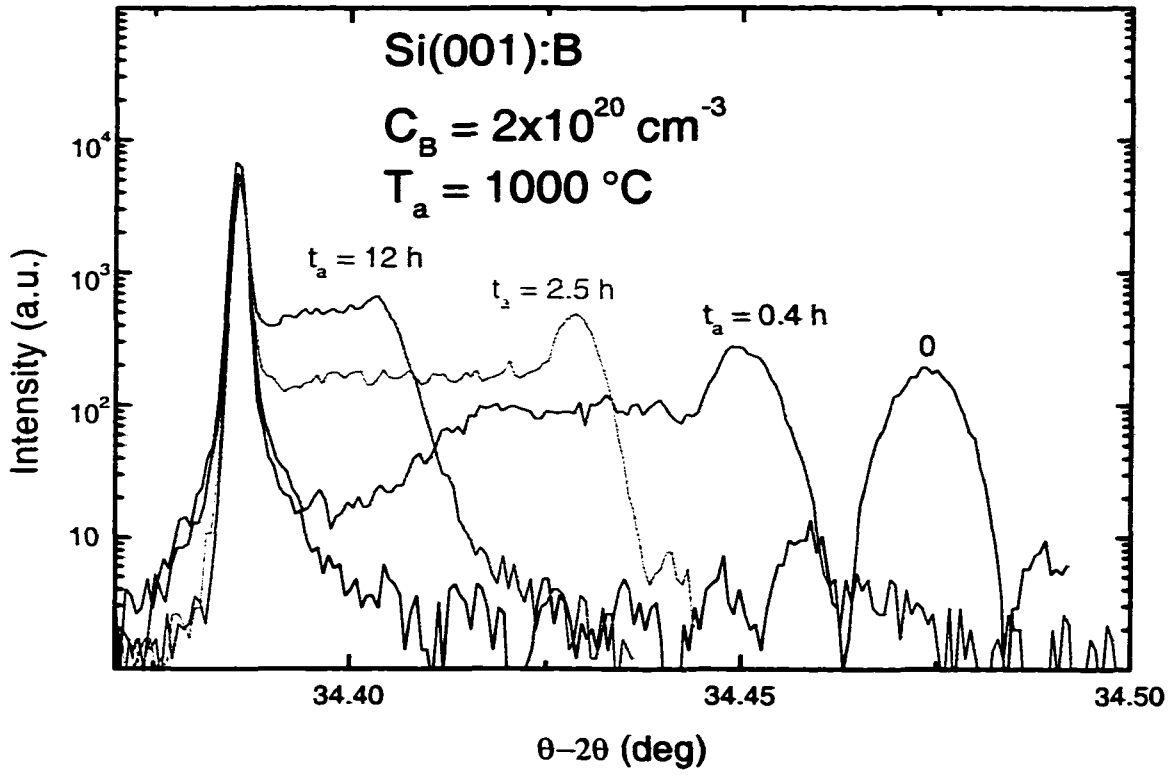

Figure 9.1. HR-XRD ω–2θ scans as a function of annealing time at T_a = 1000 °C

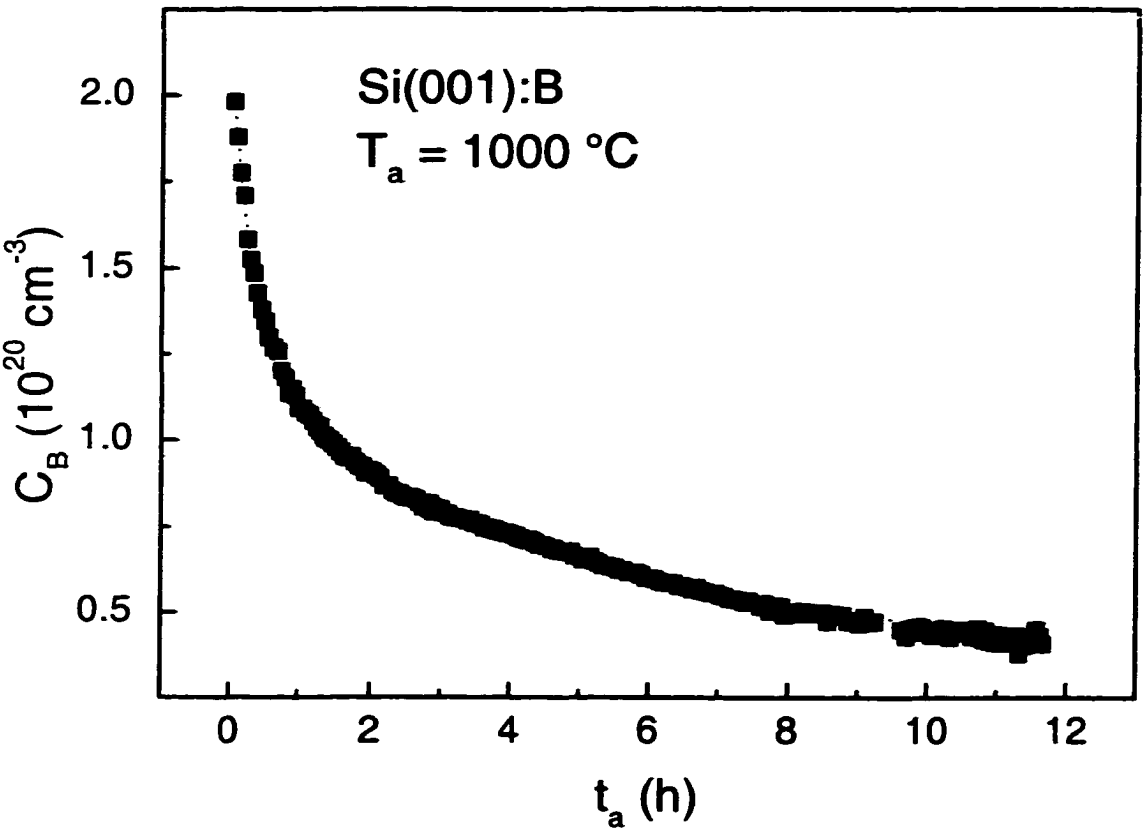

Figure 9.2. B concentration values inferred from HR-XRD data as a function of annealing time at T_a = 1000 °C.

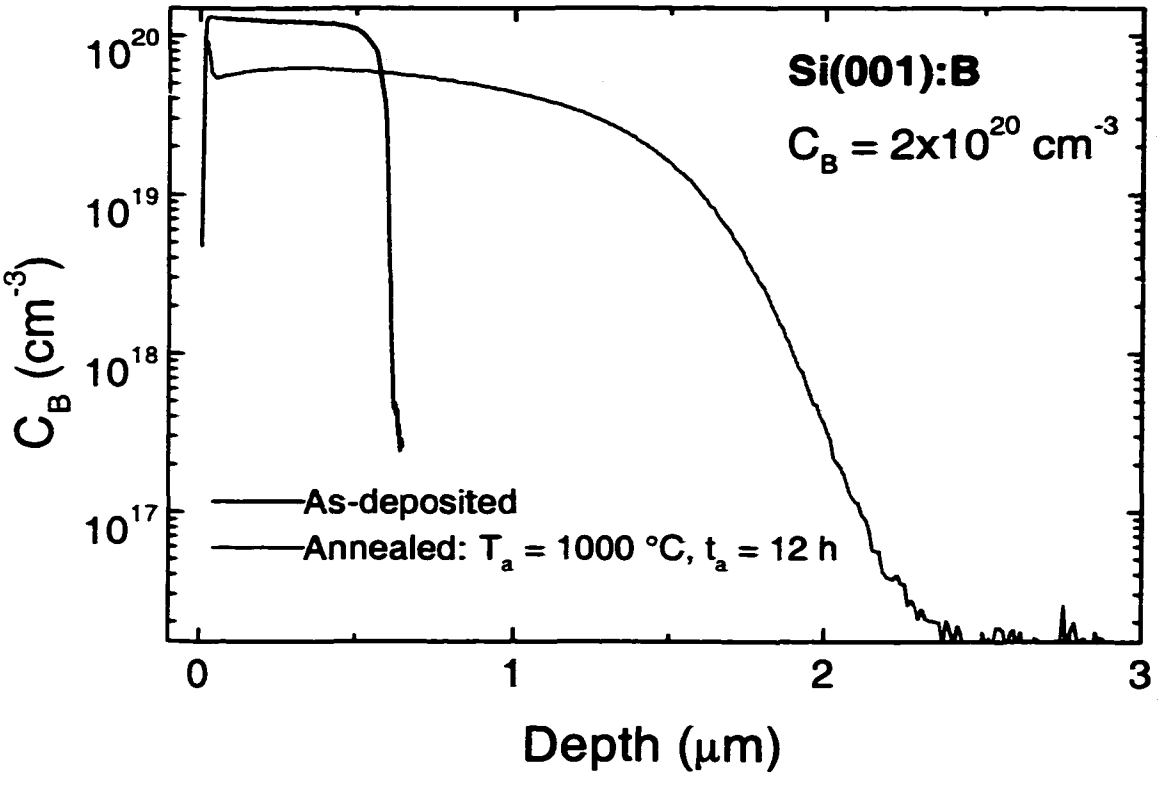

Figure 9.3. SIMS depth profiles for a Si(001):B sample before and after annealing.

APPENDICES

Appendix A

The Si-B bond length in Si:B was calculated based upon the β value obtained from the $a_{\perp}(C_B)$ data in Fig. 5.17 and equation 5.4 using the following procedure. The lattice parameter for a hypothetical zincblende-structure $Si_{0.5}B_{0.5}$ alloy, in which every bond is between neighboring Si and B atoms, was obtained by linear extrapolation of the $a_{\perp}$ vs C_B curve in Fig. 5.17 to $C_B = N_B = N_{Si}/2 = 2.5x10^{22}$ cm^{-3}. The tetragonally-strained unit cell was converted to a cubic cell using the Poisson ratio for Si, $\nu_{Si} = 0.278$, and assuming linear elasticity. The cubic lattice parameter was then used to calculate the Si-B bond length given the 109.5° tetrahedral bond angle. The result yields $r_{Si\text{-}B} = 2.04$ Å.

The bond length $r_{Si-B_{pair}}$ between nearest-neighbor Si and B-pair B atoms was calculated using an analogous procedure. I determined $a_{\perp}$ for an hypothetical ordered $Si_{0.33}B_{0.66}$ alloy composed of Si and B-pairs as basis sets on substitutional zincblende sites. This was done by extrapolating $a_{\perp}(C_B)$ to the value corresponding to $C_B = 2N_{Si}/3$ with $N_B = 0$. The tetragonal cell was converted to cubic as described above. $r_{Si-B_{pair}}$ values were then calculated for different B-pair bond-axis orientation distributions based upon the cubic cell volume with a B-B bond length of 1.60 Å[37,50] and trigonal Si-B-Si bond angles of 120°. Three cases were considered: (1) all B-pairs aligned with their bond axes along the [001] growth direction, (2) B-pairs aligned randomly along in-plane [100] and [010] directions, and (3) B-pairs distributed equally in all three orthogonal ⟨100⟩ directions. In the latter case, a

supercell of three unit cells was used. The results for $r_{Si-B_{pair}}$ are: (1) 1.70, (2) 2.18, and (3) 2.01 Å.

Appendix B

Our group has previously shown that B segregates strongly to the second layer during Si(001):B film growth.[1,2] The process is well described by Gibbsian equilibrium segregation theory with a saturation B second-layer coverage $\theta_{B,sat}$ of 0.5 ML and a segregation enthalpy of -0.53eV. [3] The bulk B concentration C_B corresponding to $\theta_{B,sat}$ ranges from $2x10^{20}$ cm^{-3} at T_s = 550 °C to $7x10^{20}$ cm^{-3} at T_s = 800 °C. When C_B exceeds these concentrations (i.e., when $\theta_B > \theta_{B,sat}$), B begins to accumulate at the outer surface.

In the absence of B at the outer Si(001) surface, B_2H_6 dissociatively chemisorbs in a second-order thermally-activated process to yield B atoms which, mediated by second-layer segregation, move to substitutional electrically-active sites. However, the presence of B at the outer layer strongly affects the B_2H_6 adsorption process and introduces an additional B incorporation path which is precursor mediated and results in the incorporation of electrically-inactive B pairs in substitutional sites. The overall B reactive sticking probability $S_{B_2H_6}$ can be expressed as

$$S_{B_2H_6} = (S^{B}_{B_2H_6})^{f_a} (S^{B-B}_{B_2H_6})^{(1-f_a)} \quad \text{(B.1)}$$

where $S^{B}_{B_2H_6}$ is the reactive sticking probability leading to single B atom incorporation, $S^{B-B}_{B_2H_6}$ is the reactive sticking probability leading to B-pair incorporation, f_a is the electrically-active fraction of incorporated B, and $(1- f_a)$ is the fraction of B present in the form of B-pairs. When $\theta_B \leq \theta_{B,sat}$, f_a =1 and $S_{B_2H_6} = S^{B}_{B_2H_6}$. As θ_B exceeds 0.5 ML, f_a decreases exponentially with increasing C_B (see inset in Fig. 6). f_a also depends on the film growth temperature through the B segregation rate. Thus, since these growth conditions correspond to the equilibrium

segregation regime,[30] θ_B decreases with increasing T_s for a given value of C_B resulting in an increase in $f_a(T_s)$.

The total fraction x_B of B incorporated into the Si lattice is given by the ratio of the B to Si reactive sticking probabilities,

$$x_B = \frac{S_{B_2H_6}}{S_{Si_2H_6}} = \frac{(S^{B}_{B_2H_6})^{f_a}(S^{B-B}_{B_2H_6})^{(1-f_a)}}{(S_{Si_2H_6})}. \tag{B.2}$$

Extracting the rate constants from the activated reactive sticking probabilities yields

$$e^{(-E_B^{inc}/kT)} \propto \frac{(e^{(-E_B/kT)})^{f_a}(e^{(-E_{B-B}/kT)})^{(1-f_a)}}{e^{(-E_{Si}/kT)}} \tag{B.3}$$

where E_B, $E_{B\text{-}B}$, and E_{Si} are the activation energies for incorporation of B, B-pairs, and Si while $E_B^{inc} = (E_B - E_{Si})$. Taking the natural logarithm of both sides and rearranging terms, obtaining

$$\begin{aligned} E_B^{inc} &= f_a(E_B - E_{Si}) + (1-f_a)(E_{B-B} - E_{Si}) + K \\ &= \{f_a E_B + (1-f_a)E_{B-B}\} - E_{Si} + K \end{aligned} \tag{B.4}$$

in which K is constant with respect to temperature.

VITA

Glenn Aaron Glass was born in Portland Oregon on June 20, 1970. He attended the California Polytechnic State University at San Luis Obispo in the department of Materials Engineering from 1990 to 1994. While at Cal Poly, Glenn's honors include "ASM Scholar" from the American Society for Metals two years consecutively, the award for "Outstanding Undergraduate Achievement" from the Society for Advancement of Manufacturing and Process Engineering, and a scholarship from the Institute for the Advancement of Engineering. Two summers were spent as an engineering intern at Siemens Solar Industries in Camarillo, CA where Glenn assisted in development efforts of copper indium diselenide thin-film solar cells. After obtaining his B.S. in 1994, Glenn began his Ph.D. studies in the Electronic Materials division of the Materials Science and Engineering Department at the University of Illinois. In 1996 Glenn was named a Semiconductor Research Corporation and Motorola fellow, and in 1998 Glenn was honored with the Mavis memorial scholarship and the American Vacuum Society Graduate Student Award. The summer of 1998 was spent as a research intern in Motorola's Phoenix Corporate Research Laboratory in Tempe AZ, working on development of self-assembled nanostructure devices. Glenn has authored or co-authored ten scholarly peer-reviewed publications and has given seven presentations at national or international conferences. After obtaining his Ph.D. in 1999, Glenn will begin a career at Intel's Portland Technology Development facility in Oregon.